Alma Mater Studiorum – Università di Bologna

DOTTORATO DI RICERCA
in
Geofisica

Ciclo XX

Facoltà di Scienze Fisiche, Matematiche e Naturali

Settore/i scientifico disciplinari di afferenza:GEO/12

TITOLO

Reanalysis Techniques for the numerical modelling of the Mediterranean Sea Circulation

Presentata da: **Mario Adani**

Coordinatore Dottorato **Relatore**

Chiar.mo Prof. Michele Dragoni **Prof.ssa Nadia Pinardi**

Esame finale anno 2008

1. Chapter : Introduction

1.1 The Mediterranean Sea

The Mediterranean basin is located between 5° East and 35° West and between 35° - 40 ° North. It is surrounded by Europe, Africa and Asia; its longitudinal extension is about 3850 Km and its latitudinal one is about 600 Km. The mean depth is about 1500 m while its maximum one is almost 5000m in the Matapan trench. It is a semi-enclosed sea which communicates with the Atlantic Ocean through the Gibraltar Strait, which has a mean depth of 350 m and a minimum width of 22 Km. This strait is one of the major feature of the Mediterranean Sea because it regulates the exchange of water, salt heat and other hydrological proprieties with the Atlantic ocean.

There are two more straits: Dardanelles and Bosphorus. The former is the connection between the Aegean Sea and the Marmara Sea, the latter between the Marmara Sea and the Black Sea. These two straits are very shallow and narrow so that the transport is much lower than at Gibraltar: the net transport at Gibraltar is about 0.1 Sv while the Dardanelles and the Bosphorus one is about 0.01 Sv.

The Mediterranean Sea may be divided in two sub-basins: the Western extending from Gibraltar to the Sicily Strait and the Eastern going from Sicily to the Middle East coasts. The continental shelf of the Sicily Strait has a maximum depth of 500 m and it creates a barrier for the exchange of deep waters between the western and eastern parts of the Mediterranean Sea. The maximum depths of the two basins are respectively 3400 m and 4200 m for the western and eastern basins (excluding the Matapan trench).

1.1.1 Mediterranean Circulation

The Mediterranean Sea circulation is strongly forced by the wind and air-sea heat and water fluxes. The wind stress shows a very high variability at both short and long time scale. It is the main direct and indirect engine of the gyres and the mesoscales. The wind stress influences the seasonal general circulation time scale too, as shown by Pinardi et al. (2006).

The heat and water fluxes control the thermohaline circulation which govern the heat and water transports throughout the basin. This forcing plays an important role at long time scales, seasonal and interannual one. It interacts with the wind stress determining the deep waters formation whose temporal scale is of the order of decades. The air-sea fluxes show a very high variability at interannual scales (Pinardi et al.,1993).

The last important forcing is the Gibraltar Strait which controls the inflow and outflow of the Mediterranean Sea waters. The in-outflow is quite stable along the seasons and years.

The Mediterranean Sea has a negative water budget , that is the evaporation exceeds the precipitation and the river run off, so that the equilibrium is maintained gaining water from the Atlantic. The basin shows also a net loss of heat (O[10 W/m^2]) which is balanced by the net positive gain of heat from Gibraltar Strait. These two feature produce an anti-estuarine circulation: the interface is about 150 m deep.

The vertical and horizontal circulation may be described based on the water mass movement. The water masses are volumes of water which are characterized by ratios of temperature and salinity included in a particular range. In the Mediterranean sea there are:

- Modified Atlantic Water (MAW). It is characterized by low salinity values in the surface layer. Typical salinity values are ranging from 36.5 to 38.5 psu from west to east. It enters from Gibraltar Strait and it forms a layer which is not more then 100 m deep. During is path it evaporates enhancing the salt concentration so that, becoming denser, it tends to sink.
- Levantine Intermediate Water (LIW). It is characterized by temperature values raging from 15° to 17.5° C, and salinity from 38.95 to 39.1 psu in the subsurface. It is generated in eastern part of the Levantine basin in late winter by intermediate convection. The mixing

can reach 200-300 meters depth. LIW propagates eastward toward the Sicily shelf reaching a depth of 400-500 meter in that region.

- Mediterranean Deep Water (MDW). It is characterized by temperature values raging from 12.6 to 13.3° C and salinity one form 38.4 to 38.65 psu. This water mass is generated by deep convection in both the sub-basins. The Gulf of Lion area generates the WMDW which can mix with the LIW and can pass the Strait of Gibraltar going out from the Mediterranean Sea. In the eastern basin there are two locations which are interested by this phenomenon : Adriatic and Aegean Sea. The water mass generated in the eastern basin (EMDW) sinks more than the depth of the Sicilian continental shelf so that it can not mix with WMDW.

Recent studies have demonstrated that the Mediterranean circulation is due to an equilibrium among mesoscale, seasonal and interannual variability (Robinson et al., 2001, Demirov and Pinardi, 2007); the strong interaction among different scale's dynamics makes it difficult to study the Mediterranean circulation. Moreover the two sub-basins show a different behaviour: in the western basin, the seasonal variability dominates while in the eastern one both seasonal and interannual signals are present. Seasonal and interannual changes are also connected to changes in the characteristics of intermediate and deep water masses (Korres et al., 2000).

Nevertheless, in order to simplify the description, it is possible to define three type of circulation based on temporal-spatial scale:

- Basin scale circulation (including the thermoaline circulation)
- Sub-basin scale circulation
- Mesoscale circulation

The most important aspect of the basin scale circulation is the thermoaline one, that is the vertical and horizontal water mass movements due to differences in density.(Figure 1-1 from Pinardi and Masetti, 2000)

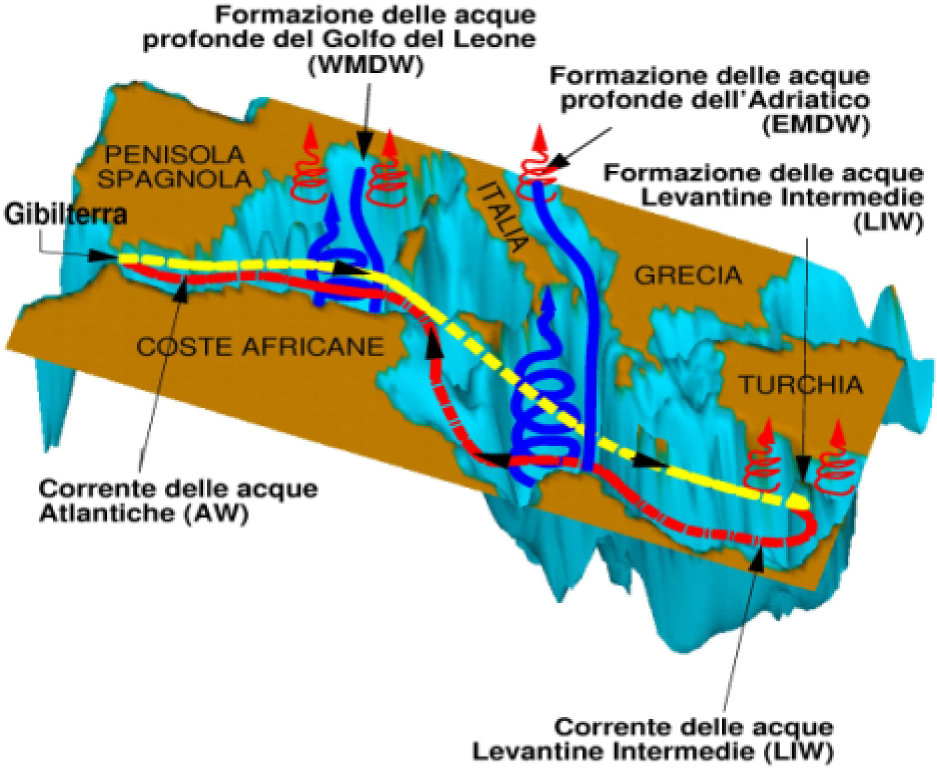

Figure 1-1: Schematic of thermoaline circulation in the Mediterranean Sea (Pinardi and Masetti, 2000)

This circulation looks like a “conveyor belt” and it is divided in zonal and meridional. The former is driven by the intermediate water formation processes and corresponds to Atlantic Water which enters from Gibraltar. This water interacts with the atmosphere during its movement toward the Middle East becoming denser. In an area between Rhodes and Cyprus this water mass sinks and becomes intermediate Levantine water. It goes eastward and leaves the Mediterranean sea trough the Gibraltar Strait. The variability associated to this circulation is seasonal.

The meridional circulation is driven by the deep water formation processes that have a large interannual variability.

The deep water formation processes are localized in small areas and there are a couple of regions in which it is possible to find the correct conditions in order to trigger such a process: one of them is located in the western basin in an area called Gulf of Lion around 42°N and 5°E (WMDW). In the eastern basin the deep water (EMDW) is formed in the Northern and Southern Adriatic. The

EMDW exits from Otranto Strait and spreads into the Ionian Sea but it can not mix with WMDW because its depth is deeper then the bathymetry of the Sicilian continental shelf (about 400 m). After the Eastern Mediterranean Transient in 1988-89 the Aegean Sea has been the site for active deep waters formation processes. This water mass (AGDW) is warmer then the Adriatic one but saltier and dense. The AGDW has filled up the deep layers of the Ionian basin and for almost a decade it has replaced the conventional EMDW

Figure 1-2: The surface circulation structures (from Pinardi et al. 2006)

The sub-basin circulation is characterized by shorter temporal and spatial scales and the structures of this circulation are more evident at the surface. In the Alboran Sea the water coming from the Atlantic meanders and creates two anti-cyclonic gyres (3a in Figure 1-2). The Atlantic water becomes Algerian current and it becomes progressively unstable and generates cyclonic and anti-cyclonic mesoscale eddies (3b in Figure 1-2). Observations (Millot, 1985) show that only the anticyclonic eddies survive, increase in size, propagate eastward, and can leave the coast drifting into the Balearic Basin. The Algerian current goes along the African coast toward the Sicily Straits where it bifurcates: one branch enters in the Eastern Basin (3d in Figure 1-2), the other one goes northward in the Tyrrhenian Sea throught the Sardinian Channel (3c in Figure 1-2). This current flows ciclonically along the Italian coast. In winter the cyclonic gyre is more intense and it extend for the entire Tyrrenian Basin, while in summer it is confiened to the northern part and the south Tyrrhenyan can invert its circulation in anticyclonic one. Part of the Northward Tyrrhenian current pass trough the Corsica Channel and originates the Liguro-Provencal current (1a in Figure 1-2), which flows along the Italian and French coast. This currents meanders and is more intense during winter.

The branch on Algerian current which reaches the Ionian Sea is called Atlantic-Ionian Stream (3d in Figure 1-2). It divides the the Ionian basin in two parts, the northern one has a cyclonic circulation but in the southern one prevails the anticyclonic one. South from Create this current bifourcates, one branch follows the lebanese-egyptian coast called Southern Levantine current (3g in Figure 1-2), the other one is the Mid-Mediterranean Jet (3f in Figure 1-2) which cuts the Levantine Basin passing by the south coast of Cyprus. South from the jet two anticyclonic gyre are present: Mersa-Matruh and Shikmona (8a and 8b in Figure 1-2); while in the northern cyclonic system are usually found: Rhode and Iera-Petra gyre (4 and 10 in Figure 1-2). Generally speaking we can conclude that the surface horizontal circulation of the Mediterranean basin shows more cyclonic gyre in the north and anticyclone in the south (Pinardi and Masetti, 2000). The main features of the sub-basin scale circulation are the semi-permanent gyre and only quite recent it has been formulated the hypotesis that the main forcing of such circulation was the wind stress curl (Pinardi and Navarra 1993, Molcard et al. 2002)

The mesoscale circulation can not be described as the sub-basin or basin scales because its temporal scale is evanescent: eddies with opposite sign appear and disappear every few weeks. The horizontal diameter of the mesoscale process is generally four to five times the local Rossby radius of deformation. This is an oceanographic measure to define the spatial scale processes for which the adiabatic vertical movements are of the same order of magnitude of the horizzontal one. In the Mediterranean sea the Rossby radius of deformation is about 10-14 km. The dynamical instability of the jet currents such as the Algerian current, the Atlantic-Ionian Stream and the Mid-Mediterranean jet can give rise to eddies that modify the local themohalien structure of the water column. Moreover these eddies can interact with the main current producing deviations of the current itself from its original path. Usually these eddies are quite evanescent far from the energy source which has created them so they cannot travel much from the upgrowth point. The mesoscale eddies were sampled for the first time in the Mediterranean basin by Robinson et. al. (1987) with a high resolution observational campaign. He demonstrates the presence of mesoscale eddies typical of the open ocean. These eddies are important because they partecipate to the transport of the Levantine waters which are trapped inside the eddies. Paschini et al. (1993) in the Adriatic sea and Ayoub et al. (1997), analizing altimetry data, have found evidences of eddies everywhere in the Mediterranean Sea.

1.2 What is Data Assimilation?

Estimating the state of the ocean circulation is one of the central issues in oceanography. Traditionally, such studies have been pursued by two separate approaches: inductive analyses of direct observations on one hand and deductive studies through numerical ocean modeling on the other. A systematic approach to the former include inverse modeling and the latter is represented by numerical solutions using ocean general circulation models (OGCM). The issue of combining the two approaches, namely data assimilation, has received attention from the eighties, following the example of meteorology.

Data assimilation is a procedure in which observations are combined in an "optimal way" with the numerical modeling. The "optimal way" is to be intended as minimizing the combined errors of the observations and the model simulations. From the mathematical point of view data assimilation could be considered as an inverse problem. That means, given two independent estimates of a the same unknown and its respective errors, using the theory of the least-square, data assimilation looks for the most probable solution. Thus the optimality is defined as the state having the least expected error variance given the input data.

The behaviour of geophysical fluids is non-linear: ocean states that are initially similar often differentiate rapidly over time. Data assimilation (Malanotte-Rizzoli, 1996 Robinson et al., 1998) is essential to control phase and loss of predictability errors and to optimize forecast accuracies. The predictability limit is the theoretical time necessary for two slightly different true ocean states to become undistinguishable from two arbitrarily chosen states. It is inherent to the growth rate of errors for a perfect prediction model. It depends on the true ocean processes under consideration and is a function of the initial uncertainty.

The ability of a system to predict certain ocean phenomena is the predictive capability of the system for those phenomena. It considers all sources of data, model errors (initial and boundary conditions, model processes) and their evolution. It needs to be quantified as a function of the observation network, models and assimilation criterion used. The system predictive capability is ultimately limited by predictability. Before the predictability limit is reached, which depends only on the non-linear transfer of errors from smaller to larger scales, other sources of errors (quality and quantity of observations, forcing, model structures and parameters, initialization and assimilation scheme etc.) limit the predictive capability.

A field estimate made by melding data and dynamics by a short dynamical adjastment model run, after assimilating data, is called nowcast which is of primary importance to initialize the model in order to produce succesful forecast. Moreover data assimilation techniques are used to produce analysis and reanalysis which are described in section 1.2.2. The main difference between the two is that usually analysis are carried out in a operational way: day by day or week by week an analysis is produced and the last field is the nowcast from which a forecast is initialized. A reanalysis is the best estimate of the past state of the ocean so that the most complete time series of observations is considered in the past (filter) or even in the future (smoother).

Ocean science and marine techology are inherently interdisciplinary subjects and physical forcing plays an important role in many aspect of, e.g., acustical, biological and sedimentological dynamics in the sea. Thus there are a variety of scientific and practical applications for which a realistic estimation of the physical fields is relevant: climate studies, biogeochemical cycles, ecosistem dynamics, sustainable fisherie managment, tactical decisions in enviromental risk, search and rescue operations, not to mention all the related field linked to economic and defence aspects such as tourism, energy, submarine and mine warfare, etc.

1.2.1 The Assimilation schemes

The data assimilation techniques can be divided into two main groups: the sequential and the variational data assimilation. In the former case the minimization is carried on in two steps: (i) the forecast of the state vector and of its error covariance are computed, and (ii), the data-forecast melding and error update, which include the linear combination of the dynamical forecast with the difference between the data and model predicted values for those data (i.e. data residuals), are estimated. The variational data assimilation minimizes the cost function each time observations are available, penalizing the time-space misfits between the data and the numerical solutions, with the constraint of the model equations and their parameters.

The most common algorithms which belong to the first class of assimilation schemes are Optimal Interpolation (OI), Kalman filter, Rauch-Tung-Striebel smoothing while 3Dvar and 4Dvar (three and four-dimentional variational scheme) are the one for the second class.

The OI is the most unexpensive technique from the computational point of view because it finds a local solution and discontinuities might appear in the analysis due to the presence of nearby observations (Gautier et al. 1999) , and time-dependent dynamical constraints are not explicitly enforced.

The main advantage of Kalman filtering and Rauch-Tung-Striebel smoothing is that they provide a formal estimate of errors for the data assimilation solution. However, the price one pays is the computation of the error covariance and the filter/smoother gain at each time step. Moreover the filtering and the smoothing techniques can provide a way to perform a global spatial adjustement. In general smoother differs from filter because it uses also formally future observations and then it should be capable to obtain more accurate estimates. Smoother can also provide physically consistent fields because the corrections are associated to the control variables of the system and not to the state variable as in the filter phase. This concept will be better developed in section 3.1.

Variational approaches seek the solution of a minimization problem performing several evaluations of the cost function, which gives the distance between the model variables and the observations, and its gradiant.Compared with variational approaches such as the 3Dvar, sequential algorithms require less initial investiment in terms of coding: the variational schemes does not require, as in sequential schemes, complex linearized observational opearator (projector of the model space onto the observational space) and are naturally designed to incorporate gradual developments. Although data assimilation theory is well-known, direct implementation of such assimilation schemes is impractical for most state-of-the-art OGCM because of the computational requirements. Typical state-of-the art general circulation models have millions of prognostic variables. Consequently, the corresponding model's state error covariance matrix, which describes the errors relationships, has over a million squared elements.

In order to solve this problem various approximations of variational and sequantial methods have been put forth to simplify their computational implementation either in deterministical direction or stocastic one, i.e., Singular Evolutive Extended Kalman filter (SEEK) introduced by Pham et al. 1998, Reduced Order Optimal Interpolation (De Mey and Benkiran,2000), Ensemble Kalman Filter (EnKF) developed by Evensen 1994.

1.2.2 The Re-analysis

The ocean climate has traditionally been studied by statistical analysis of observations of particular oceanic properties such as temperature. Climatological information is often presented in terms of long-term averages, and sequences of observations are examined in order to find for example evidence of warming. A powerful new approach to climate analysis has emerged in recent years. It applies the tools and techniques of modern data assimilation in a process called re-analysis. The products, so-called re-analyses, have applicability far beyond that of traditional climate information. Forecasts of increasing accuracy have resulted from refining numerical models and from refining data assimilation techniques together with the availability of new data sets, such as satellite data. Both refinements have been made possible by investment in powerful computer systems, complementing the even larger investment made in the observing systems.

In daily forecasting the in situ and satellite based observations are combined with a short forecast based on earlier observations to create the initial state for a new forecast. In a re-analysis, the observations collected in past decades are fed into a modern forecasting system that is much more refined than the systems available when most of the observations were made. Oceanic and boundary conditions are reconstructed for each day of the period over which suitable observations exist. Re-analysis differs from the traditional climatological approach in that it processes a wide variety of observations simultaneously, using the physical laws embodied in the forecast model and knowledge of the typical errors of forecasts and observations to interpret conflicting or indirect observations and fill gaps in observational coverage.

Each re-analysis creates a new view of the climate of the ocean and its variations. Time consistency is a very important consideration for climate studies and in the context of re-analysis, the data assimilation is applied with minimum changes throughout the period producing consistent estimates without major changes in the modelling assumptions. The usage of the operational products for climate research is problematic. Deficiencies in the analysis method or in the numerical model could introduce significant biases in the resulting analyses, and could invalidate the conclusions drawn from them. Many of these deficiencies are removed over time, but this could have introduced trends or discontinuities in the operational analysis time series that are of difficult interpretation (e.g. Trenberth and Olson 1988; Trenberth and Guillemot 1995).

1.3 Objectives and structure of the thesis

This thesis has been inspired by the need to have the best knowledge of the climate of the Mediterranean Sea in order to evaluate the climate change in the Mediterranean region. Since each reanalysis produces a different picture of the state of the ocean, an interesting topic is to qualify and quantify the differences between reanalysis produced changing only the assimilation scheme. This is one of the main objective of this work.

Moreover many of most important scientific properties of the ocean circulation, e.g. heat flux and potential vorticity, are never actually measured, but they can be calculated from estimates of the circulation from numerical model. Then it becomes important to have an assimilation scheme such as the Partitioned Kalman Filter/Smoother (PKFS), which can produce physically consistent solutions (BUDGET CONSERVATION). So the other objective of this thesis is to implement and assess the weaknesses and strengths of that assimilation scheme. The choice to implement the PKFS on a well-known problem, whose analytical solution is already proven, is dictated by the necessity to discern the real solution which can not be known in a realistic case for geophysical sciences.

The organization of the thesis is the following:

In chapter 2 the implementation of a realistic water flux in the numerical model is presented and the numerical simulation will be assessed for a period from 1992 to 2000. The impact of a realistic water flux versus the one proposed by Tonani et al. (2007) will be discussed. This preliminary work has been necessary to understand the predictive skills of the general circulation model.

The implementation and the results of the Partitioned Kalman Filter and Smoother will be described in chapter 3 where it will be examined also the possibility of a future implementation for a realistic case in order to have a physically consistent reanalysis of the Mediterranean circulation.

In chapter 4 the optimal interpolation and 3DVAR reanalysis experiments will be commented, the historical dataset collected for the assimilation will be presented and a discussion of the estimated circulation for the two numerical experiments will be carried out.

The last chapter will illustrate the main conclusions.

2. Chapter: Simulation of the Mediterranean Sea circulation

In this chapter the ocean general circulation model used in the thesis is presented together with the upgrades carried out to improve some of its processes representation. The code is OPA8.1 (Madec et al., 1998) and it has been implemented in the Mediterranean Sea for the first time by Tonani et al. (2007).

Improving the model will help to make assimilation working more efficiently and thus create conditions for which maximum advantage from assimilation of observations can be achieved. The water flux formulation of the model was then changed because it was thought to be a major drawback of the present numerical model (Tonani et al., 2007).

2.1 The ocean general circulation Model

Ocean general circulation models normally are based upon the so-called primitive equations. They are the Navier-Stokes equations on a rotating earth with gravity and with the following approximations:

- Spherical Earth: gravitational force is always perpendicular to horizontal velocities.
- The depth of the ocean is negligible compared to the Earth radius.
- The density variations are negligible except for the buoyancy force (Boussinesq approximation).
- The vertical momentum equation reduces to hydrostatic balance that is Coriolis, frictional, and vertical acceleration terms are considered negligible.
- The continuity equation reduces to the imposition of a divergencelss velocity field (incompressible flow).

The model equations are:

$$\frac{\partial u}{\partial t} = (\zeta + f)v - w\frac{\partial u}{\partial z} - \frac{1}{2a\cos\varphi}\frac{\partial}{\partial\lambda}\left(u^2 + v^2\right) - \frac{1}{\rho_o a\cos\varphi}\frac{\partial p}{\partial\lambda} - A^{lm}\nabla^4 u + \frac{\partial}{\partial z}\left(A^{vm}\frac{\partial u}{\partial z}\right) \quad \text{eq: 2.1}$$

$$\frac{\partial v}{\partial t} = -(\zeta + f)u - w\frac{\partial v}{\partial z} - \frac{1}{2a}\frac{\partial}{\partial\varphi}\left(u^2 + v^2\right) - \frac{1}{\rho_o a}\frac{\partial p}{\partial\varphi} - A^{lm}\nabla^4 v + \frac{\partial}{\partial z}\left(A^{vm}\frac{\partial v}{\partial z}\right) \quad \text{eq: 2.2}$$

$$\frac{\partial p}{\partial z} = -\rho g \quad \text{eq.2.3}$$

$$\frac{1}{a\cos\varphi}\left[\frac{\partial u}{\partial\lambda} + \frac{\partial}{\partial\varphi}(\cos\varphi v)\right] + \frac{\partial w}{\partial z} = 0 \quad \text{eq: 2.4}$$

$$\frac{\partial\theta}{\partial t} = -\frac{1}{a\cos\varphi}\left[\frac{\partial}{\partial\lambda}(\theta u) + \frac{\partial}{\partial\varphi}(\cos\varphi\theta v)\right] - \frac{\partial}{\partial z}(\theta w) - A^{lT}\nabla^4 T + A^{vT}\frac{\partial^2\theta}{\partial z^2} + \delta\mu\left(\theta^* - \theta\right) \quad \text{eq: 2.5}$$

$$\frac{\partial S}{\partial t} = -\frac{1}{a\cos\varphi}\left[\frac{\partial}{\partial\lambda}(Su) + \frac{\partial}{\partial\varphi}(\cos\varphi Sv)\right] - \frac{\partial}{\partial z}(Sw) - A^{lS}\nabla^4 S + A^{vS}\frac{\partial^2 S}{\partial z^2} + \delta\mu\left(S^* - S\right) \quad \text{eq:2.6}$$

$$\rho = \rho(T, S, p) \quad \text{eq.2.7}$$

The momentum equation are re-formulated as function of the vorticity $\zeta = \frac{1}{a\cos\varphi}\left[\frac{\partial v}{\partial\lambda} + \frac{\partial}{\partial\varphi}(u\cos\varphi)\right]$, u,v,w are the components of the velocity vector, a is the Earth radius, $f = 2\Omega\sin\varphi$ is the Coriolis term with Ω the constant Earth rotation rate, p is the hydrostatic pressure, θ is the potential temperature, S is the salinity, ρ is the in situ density and ρ_o=1020 kg m^{-3} is the reference density, A^{lm},A^{vl} are the horizontal and vertical eddy viscosities respectively, A^{vT},A^{vS} are the vertical diffusivity coefficients and A^{lT},A^{lS} horizontal diffusivities coefficients for temperature and salinity respectively, μ and δ are the relaxation coefficient.

The model integrates also a free surface equation with an implicit scheme. The numerical implementation of the implicit free surface scheme is described in Roullet et al. (2000).

In order to solve the model equations described above it is necessary to impose boundary conditions at the vertical and lateral boundaries.

For the vertical velocity, the boundary condition at the bottom (z=-H) is

$$w = -\vec{u}_h^{\,b} \cdot \nabla H$$

where $\vec{u}_h^{\,b}$ is the meridional and zonal component of the bottom velocity. At the surface (z=η) the vertical boundary condition for *w* is

$$w = \frac{D\eta}{Dt} - WF \,.$$

where *WF* is the imposed Water Flux. In this thesis we will compare between two different formulations of the *WF*.

The vertical boundary condition for the horizontal velocity components are: at the bottom

$$A^{vm} \left. \frac{\partial \vec{u}_h}{\partial z} \right|_{z=-H} = C_D \sqrt{u_b^2 + v_b^2 + e_b \vec{u}_h^{\,b}}$$

where C_D is the drag coefficient and e_b is the bottom kinetic energy due to the tides, internal waves breaking and to other processes characterized by short temporal and spatial scales. The corresponding boundary condition at the surface is

$$A^{vm} \left. \frac{\partial \vec{u}_h}{\partial z} \right|_{z=\eta} = \frac{\vec{\tau}}{\rho_O}$$

where $\vec{\tau}$ is the wind stress.

The boundary condition for the temperature and salt flux at the bottom is

$$A^{vT,S} \frac{\partial}{\partial z} \left. (T, S) \right|_{z=-H} = 0$$

while at the surface is $A^{vT} \left. \frac{\partial T}{\partial z} \right|_{z=0} = \frac{Q}{\rho_o C_p}$

where C_p is the specific heat capacity, Q is the net heat flux. For the salinity, the salt flux, corresponding to the water flux is:

$$A^{vS} \left. \frac{\partial S}{\partial z} \right|_{z=0} = WF \; S_{z=0} \rho_o \,.$$

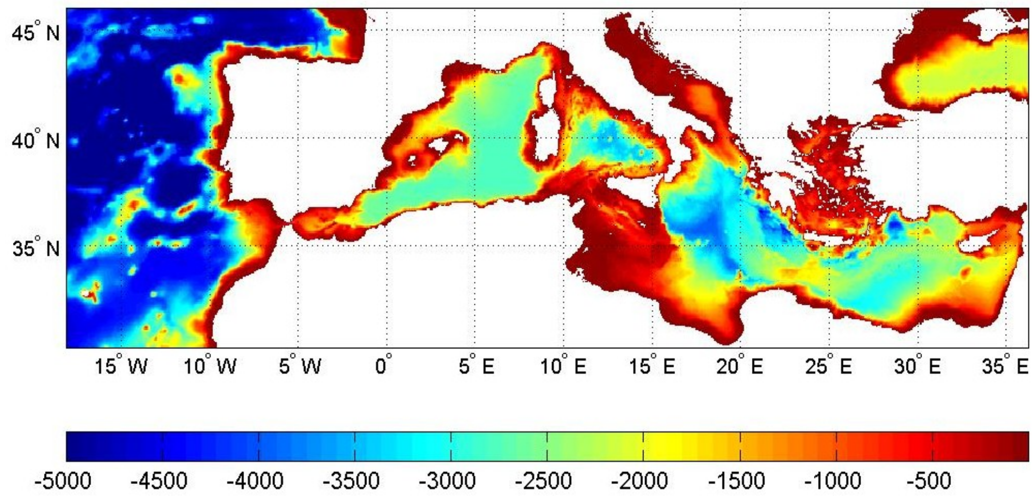

Figure 2-1 Topography for the entire model domain.

The model domain is shown in Figure 2-1 and it extends in the Atlantic. The so-called Atlantic box helps to simulate properly the transport at the Gibraltar Strait. However, in the present formulation the model considers the Atlantic box as closed and in order to maintain temperature and salinity values consistent with the climatology in the box, the model salinity and temperature fields are relaxed to the climatological values along a strip at the latitudinal and longitudinal boundaries of the Atlantic domain. The strip is an area with the extension of 2° at the westward and southward boundaries and 3° at the northern boundary in order to cover the entire Gulf of Biscay region. The last right hand term of equations 5 and 7 is the term that produces such relaxation in the Atlantic box.. The μ coefficient is spatially varying: it is larger closer to the Atlantic box strip boundary points, and then it decreases linearly to zero toward the internal sides of the strip. In this area a sponge layer is also present in order to minimize the instabilities and the horizontal diffusivities are incremented by a factor of 5.

At the Gibraltar Strait (6.25°W-5.125°W) the horizontal viscosity is laplacian instead of bilaplacian as in the rest of the domain and diffusivity is ten times bigger. The bottom friction drag coefficient is linear and ten times bigger then in the other parts of the model. These modifications are necessary to have a realistic transport trough the strait (Tonani et al., 2007)

2.2 The water flux boundary conditions

In this thesis we have chosen to intercompare two simulations done with two different formulations of the water flux term since the water loss at the air-sea interface of the model could be the source of a major model error.

The operational model of the Mediterranean Sea (Tonani et. al. 2007) uses the following approximate formulation for WF:

$$WF = \gamma^{-1} \frac{\left(S_{z=0} - S^{*}_{z=0}\right)}{S_{z=0}\rho_o} \qquad \text{eq: 2.8}$$

where $S^{*}_{z=0}$ is the climatological monthly mean salinity at the surface, and γ is the salinity relaxation coefficient whose constant value is set to –0.007 [m^2s/Kg] The corresponding "relaxation time", obtained considering $\frac{\Delta z}{\Delta t} = WF$ is:

$$\Delta t = \rho_o \Delta z \gamma \left(\frac{S_{z=0}}{S_{z=0} - S^{*}_{z=0}} \right)$$

Considering $\Delta z = 3$, which is the width of the first layer of the model, $\Delta t \cong 5$ days.

The formulation developed in this thesis is a general one and it is written:

$$WF = E - P - R \qquad \text{eq: 2.9}$$

where E is the evaporation, P the precipitation and R the runoff divided by the area of the river mouth.

Knowing that the Mediterranean Sea is a concentration basin, i.e., it evaporates water more than the water gained by the precipitation and river run off, and being the model domain closed, the total water flux, average on the domain should be zero. In order to conserve the volume in the entire model domain an artificial correction has been implemented by Tonani et al. (2007). This correction consists in adding the same amount of water lost in the Mediterranean uniformly at each grid point in the Atlantic box.

In equation 2.8 S^* is the MEDATLAS monthly mean climatological salinity. The original data is given on a regular grid of a resolution of 1/5x1/5 degree later interpolated on the model grid.

In the second experiment the water flux is a realistic flux. The evaporation (E) is calculated by the model at each time step, the precipitation is the monthly mean climatology from NCEP-NCAR reanalysis (Kistler et al, 2001) The original data have a resolution of 2.5x2.5 degrees and also in this case they have been interpolated on the model grid.

The river discharge data (R) are monthly mean climatology and they have been taken from the "Global Runoff Data Centre", while for the Adriatic river data from Raicich (1996). The river implemented are Po, Vjiose, Drin, Rhone, Ebro, Nile and zero salinity is assumed along the river mouth points.

The Dardanelles inflow from the Marmara Sea has been parametrized as a river using data inferred from Mariotti et al. (2002). The salinity associated to the Dardanelles inflow is taken from the MedATLAS monthly mean climatology. Thus formally the Dardanelles Strait has been treated as a river. The area upon which the river input is spread depends on the mass of water flowing into the Mediterranean Sea: greater is the river runoff wider is the surface.

In order to simulate a river delta the water mass input has been spread using an exponential function $f(r)=\left[1-\left(\frac{r}{A}\right)^2\right]\exp\left[-\frac{1}{2}\left(\frac{r}{B}\right)^2\right]$ which decreases in the offshore direction. The zero-crossing parameter (A) has been chosen equal to 8 km for the Dardanelles and 6 km for the other rivers while the e-folding parameter (B) for the Dardanelles is 4 km and 10 km for the others.

Near the river mouths, an upstream advection scheme has been implemented in order to enhance the mixing of fresh and salty waters. Both the precipitation and the river runoff data are not interpolated in time so that when the month changes there is an abrupt variation.

Both experiments are initialized with temperature and salinity fields from MEDATLAS climatology and from a state of rest. The simulations cover a period from 1992 to 2000 and they are forced with the same atmospheric forcing, except for the water flux. For years 1992 and 1993 the forcing is computed from ECMWF Reanalysis (ERA15) atmospheric surface variables. The spatial resolution is the T106 Gaussian Grid, (approximately 1.1250 x 1.1213 lat-lon grid) and a temporal resolution of 6 hours. For the rest of the period the atmospheric forcing comes from ECMWF operational analyses but the spatial resolution of the data change throughout the years. For the 1994 and from 1998 to 2000 the spatial resolution is 0.5 degrees while for the period from 1995 to 1997 the resolution is 0.5625 degrees.

2.3 Results

Different aspects of the simulation experiments have been studied, for example the consistency of the solutions with climatological values in order to quantify the model drift, the analysis of well-known observed features of the general circulation and particular attention has been paid to the evaluation of the differences between the two simulation experiments. For simplicity, the experiment with the water flux parametrized as in (2.8) is called experiment 1 (EXP1) and the numerical experiment with the realistic water flux parameterization as in (2.9) will be called experiment 2 (EXP2).

The first aspect which captures the attention is the improvement of the new parameterization of the water flux. In Figure 2-2 it is shown from top to bottom the surface integral of Heat flux, Water Flux and Sea Surface Height (SSH) respectively for EXP1. In Figure 2-3 there are the same quantities calculated for the EXP2. In both figures the blue curves shows the model results, the red curves are the monthly mean climatology computed from NCEP re-analysis and the green line is the multi-annual mean.

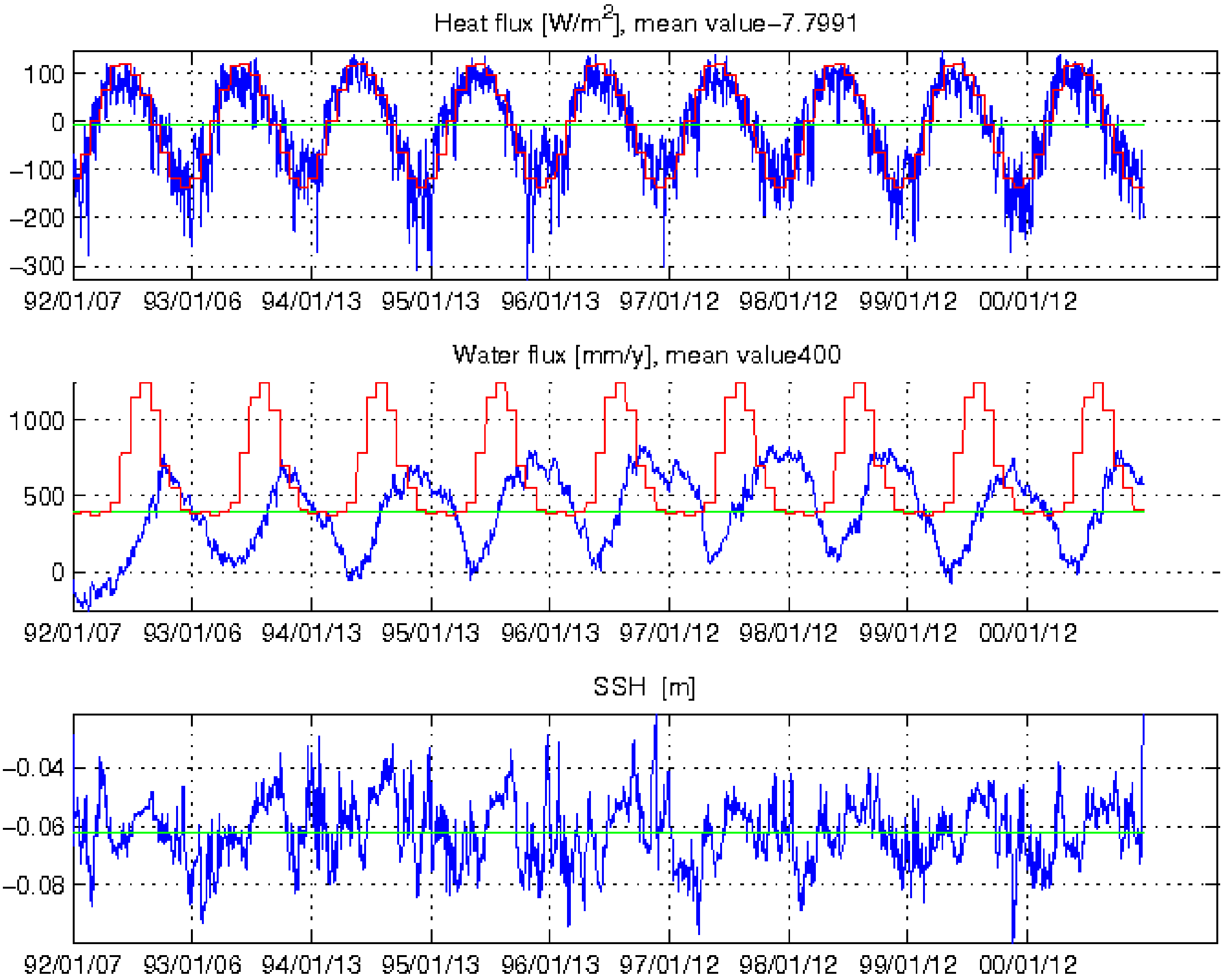

Figure 2-2 Time series for EXP1 of the basin mean heat flux (top panel), water flux (middle panel), Sea Surface Height (bottom panel). In every panel blue line is the daily mean model output, red line is the monthly mean NCEP climatology, green line is the multi-annul mean.

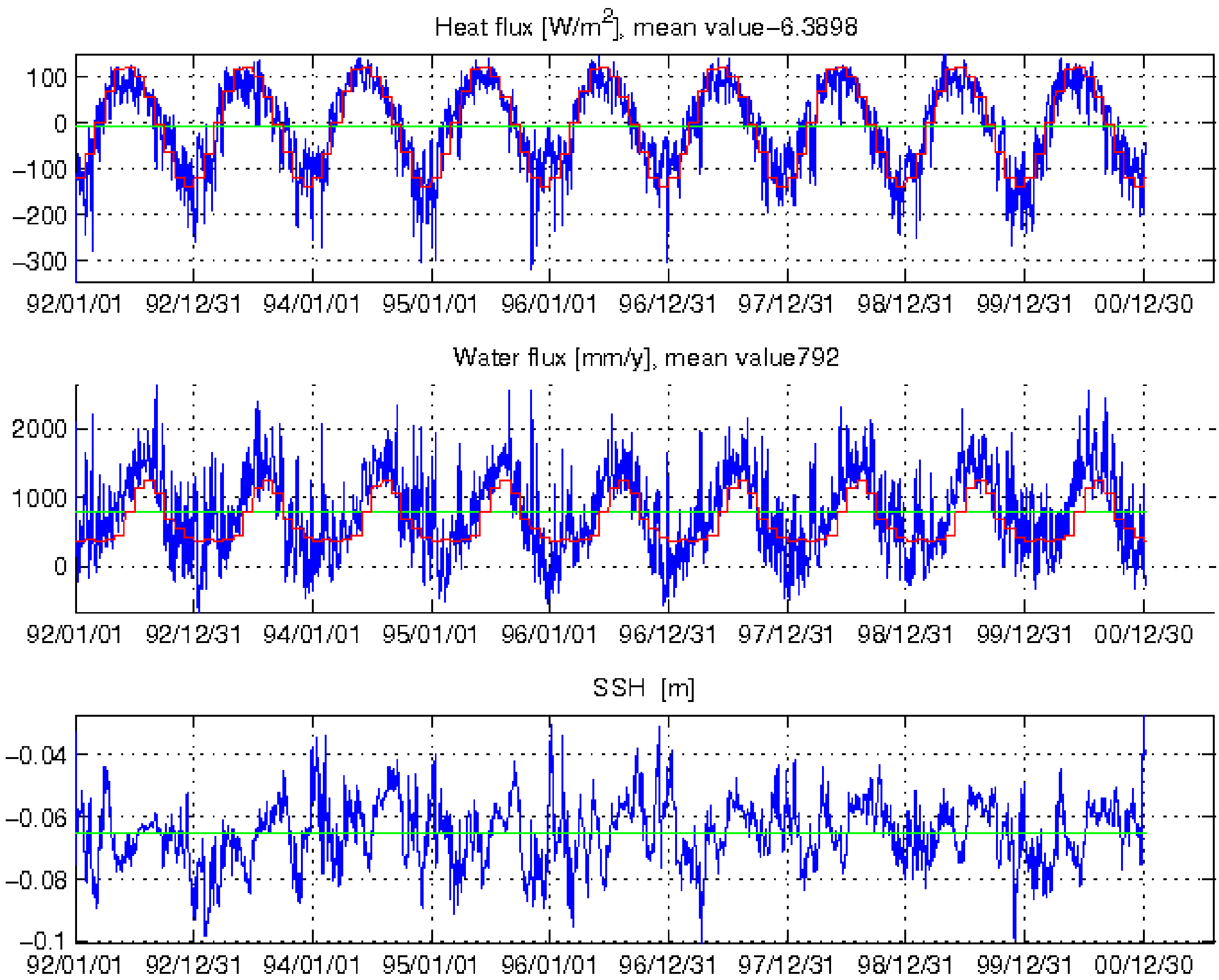

Figure 2-3 Time series for EXP2 of the basin mean heat flux (top panel), water flux (middle panel), Sea Surface Height (bottom panel). In every panel blue line is the daily mean model output, red line is the monthly mean NCEP climatology, green line is the multi-annul mean.

Heat flux and SSH don't show any significant difference between the two runs but the water flux has dramatically improved. In EXP1 the water flux has a wrong amplitude as well as a phase shift with respect the climatology. The wrong amplitude is due to the fact that the water flux is considered as the amount of water necessary to the model in order to maintain the surface salinity close to the MEDATLAS climatology, while phase error is due to the specific form of the relaxation term which becomes important when the difference between the model solution and the climatological value is largest.

For the nine years of simulation the salinity and temperature volume and surface integrals have been calculated. In the upper panel of Figure 2-4 is shown the volume integral and in the lower panel the surface integral of the temperature for EXP1. In Figure 2-5 the same quantities are represented for EXP2. Figure 2-6 and Figure 2-7 illustrate the volume and surface salinity for EXP1 and EXP2 respectively. The blue line represents the model solution, the red line the monthly mean MEDATLAS climatology and the green line the multi-annual mean. From these figures emerges clearly that the temperature values don't show any significant difference between the two runs: temperature volume integral is decreasing in both experiments, even though this tendency is slightly more accentuated in the first experiment. On the contrary the salinity trend has opposite sign: the model drift is -3,4 PSU per year in the EXP1 while it is +4,5 PSU per year in EXP2. The surface salinity has a very different behavior too, in the first experiment the values are close to climatology consistently with the fact that the two data are not completely independent because of (2.8); in EXP2 the salinity has large maximum values which suggest a mixing problem. The surface salinity curve for Exp1 is in phase with the Medatlas climatology: showing a minimum in May-June and a maximum in September, while for Exp2 the minimum is in February and the maximum in August.

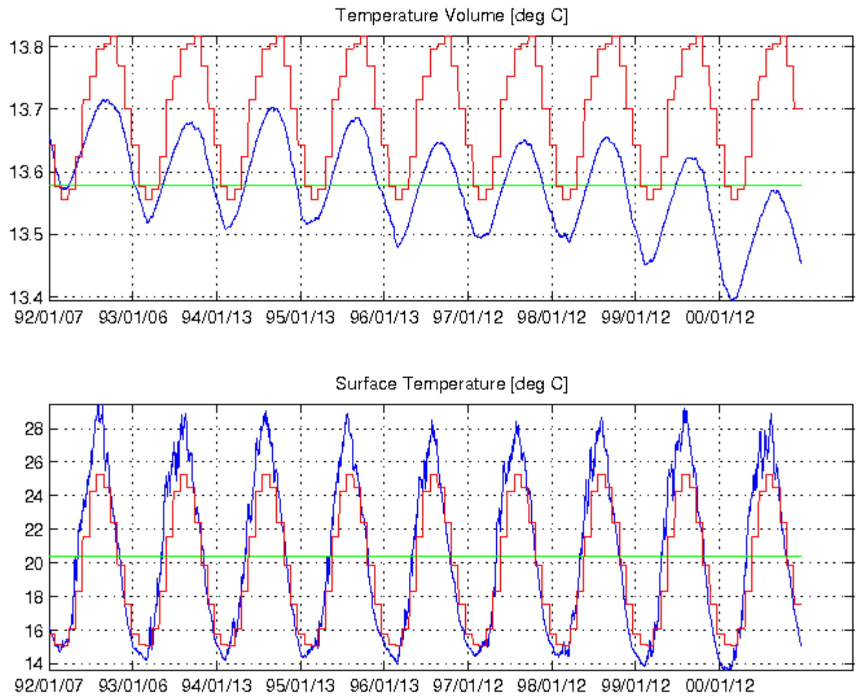

Figure 2-4 Time series of volume and surface temperature for EXP1. Blu line is the model output, red line is the MedATLAS climatology, green line is the multi-annual mean.

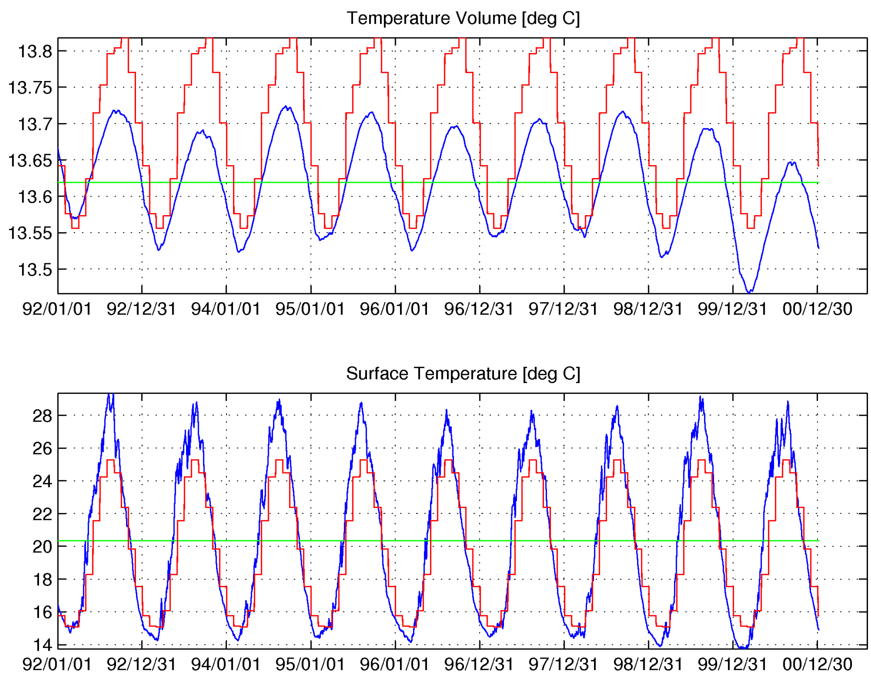

Figure 2-5 Time series of volume and surface temperature (degC) for EXP2. Blue line is the model output, red line is the MedATLAS climatology, and green line is the multi-annual mean.

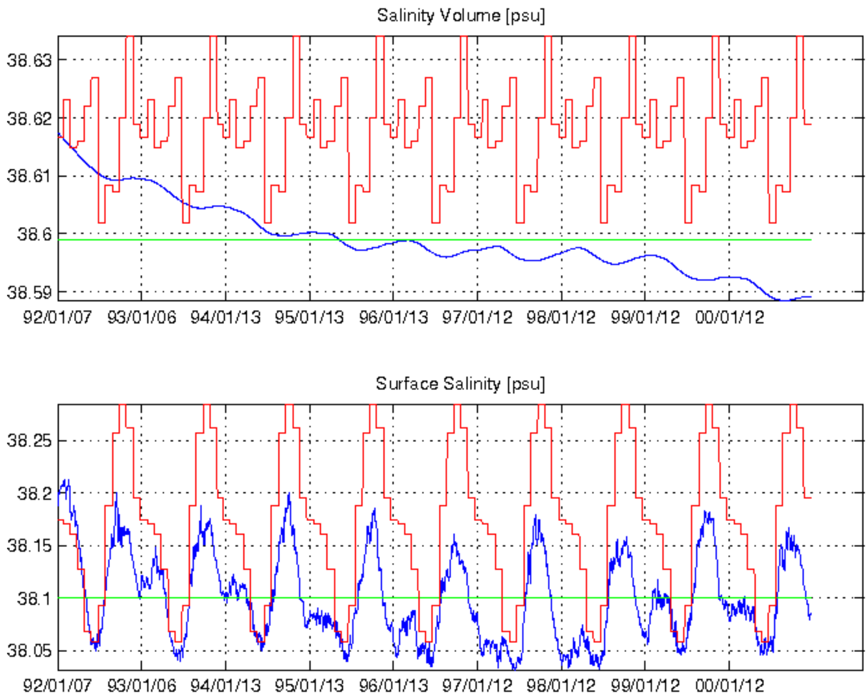

Figure 2-6 Time series of volume and surface salinity (psu) for EXP1. Blue line is the model output, red line is the MedATLAS climatology, and green line is the multi-annual mean.

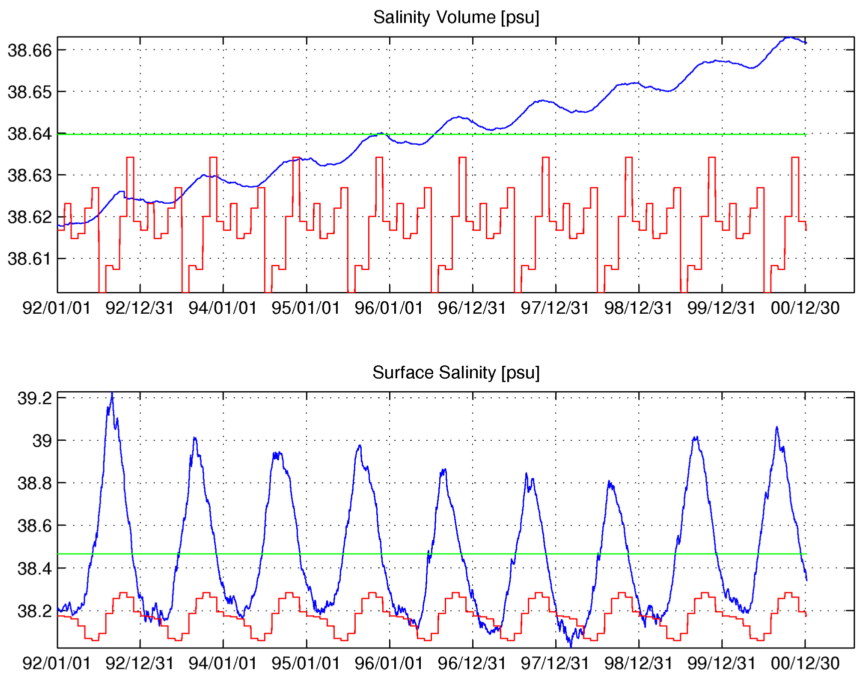

Figure 2-7 Time series of volume and surface salinity (psu) top and bottom panel respectively for EXP2. Blue line is the model output, red line is the MedATLAS climatology, and green line is the multi-annual mean.

The improvement obtained in the water flux justifies the conclusion that EXP2 has improved the simulation even if still problems are visible. In the future one of the most important improvements will be to use a new precipitation data set and revise the river runoff implementation

Additionally, particular interest has been put on identifying the spatial pattern of the drift. In order to identify the most problematic regions, the climatology of the model and of the observations (MedATLAS) for the temperature and the salinity at 1000 and 2000 meters are shown for EXP2 in Figure 2-8 and Figure 2-9. . It is evident that the drift of the salinity is related to the uniform in depth Aegean water contribution that the model creates in the Cretan passage. Observations indicate that the Aegean waters affect the salinity distribution only at 1000 meters, the model brings it down to 2000 meters. Knowing the Aegean outflow during these years, it seems very unlikely that the spreading did not involve also the deepest eastern Mediterranean layers so we cannot make conclusions about this drift.

Figure 2-10, Figure 2-11 present the temperature and climatology maps at 1000 and 2000 meters. It is now evident the cold bias of the model both in the western and eastern sub-basins. This problem is being analyzed in another thesis which started to critically examine the heat flux formulation of the model.

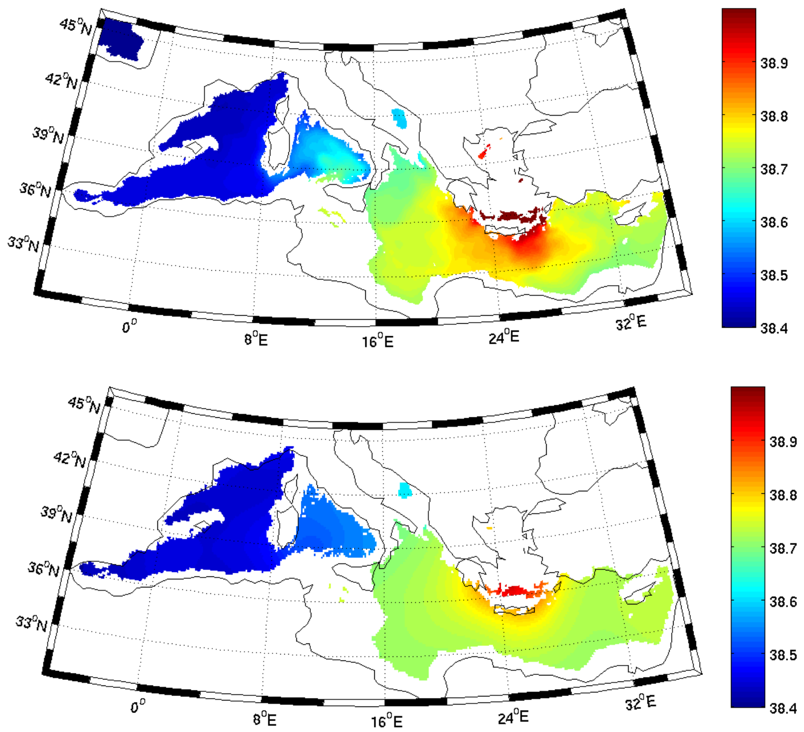

Figure 2-8 Climatological salinity [psu] at 1000 m for the model (top) and for the observation (bottom)

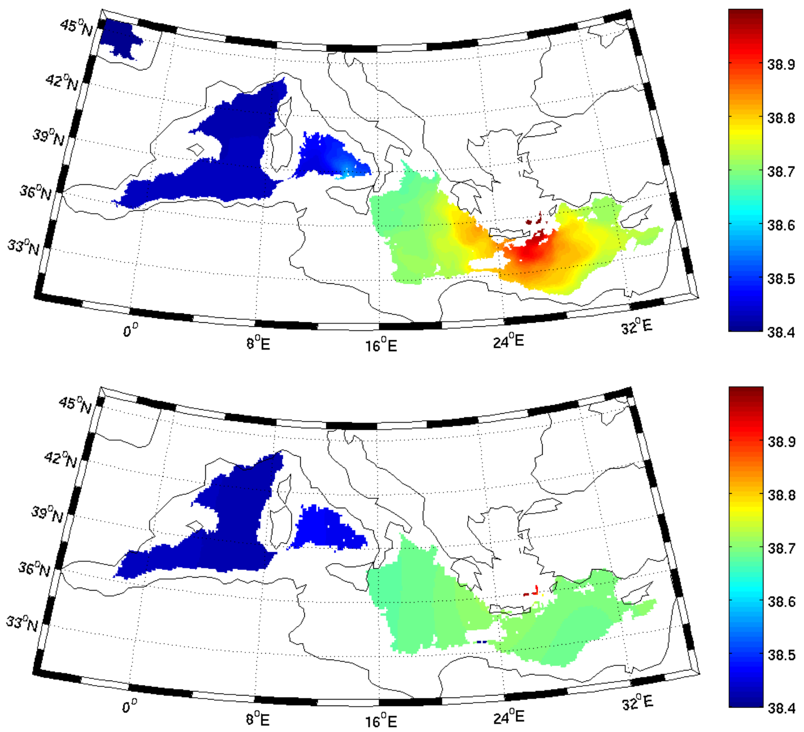

Figure 2-9 Climatological salinity [psu]at 2000 m for the model (top) and for the observation (bottom)

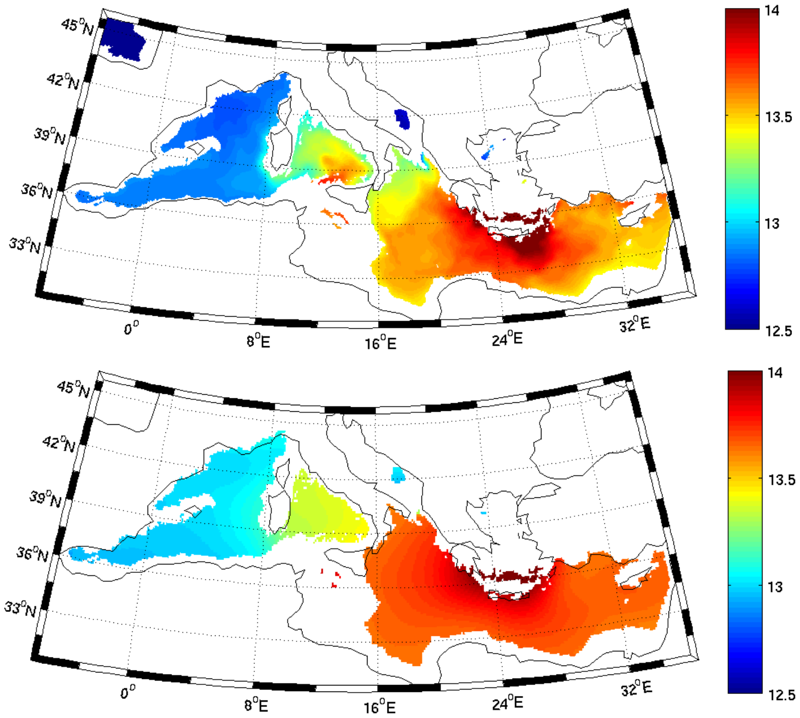

Figure 2-10 Climatological temperature [degC] at 1000 m for the model (top) and for the observation (bottom)

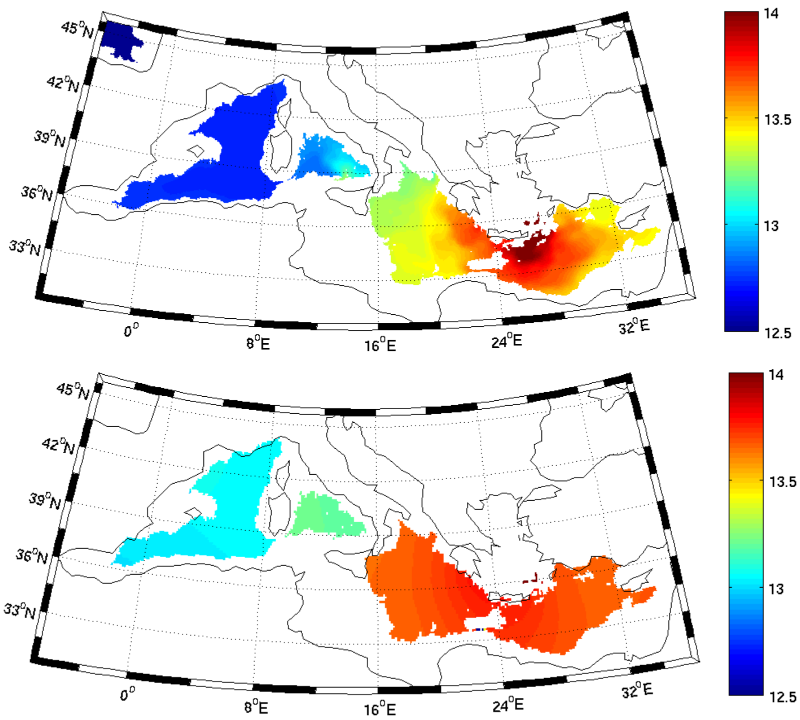

Figure 2-11 Climatological temperature [degC] at 2000 m for the model (top) and for the observation (bottom)

The comparison with the observations for EXP2 has been pushed a little bit further. The monthly mean Sea Level Anomaly has been calculated by the model for the year from 1993 to 2000 for the month of July and it is compared with a special analysis done with satellite observations In order to calculate the Sea Level Anomaly (SLA) from the sea level computed by the model, the mean dynamic topography of Dobriĉiĉ (2005) has been subtracted.. The monthly mean sea level anomaly maps computed from the observations have been taken from Pujol et al. (2005). As it can be seen from Figure 2-12 the main structure of the circulation are reproduced by the model even though the intensity and gradients are sometimes different. Both the observation and model contain a well formed Algerian current and the Alboran Sea gyres, the Asian Minor current, the cyclone in the Gulf of Lyon and in the southern Adriatic Sea are very well reproduced by the model.

The Mersa-Matruh and Shikmona gyres system are developed by the model consistently with the observations. In the Ionian Sea, the Ionian circulation inversion is very well visible from the observations but at much lower amplitude from the model. In general it is possible to conclude that the model can reproduce the circulation of the Mediterranean Sea main structures in a satisfactory way.

The comparison with observations has been done not only at a basin scale as described above but also at sub-basin scales. The top panel of Figure 2-13 shows a schematic of the mean circulation of the Ionian basin based of observation collected from mid-August to early October; the central panel shows the dynamic height calculated from observation 4 September 1997 as reported by Robinson and Sellschopp (2002). In the bottom panel the daily mean SSH calculated by the model is shown. The two quantities differ for the barotropic contribution to SSH so the comparison has to be done only in a qualitative way: the three large anticyclonic gyres are present in the observations and also in the model in approximately the correct location even if the larger one (the one closer to the Lybian cost) is smaller in the model than in the observation. The cyclonic gyre south of the Greece is overestimated by the model. The other structures present in the observations are not reproduced by the model but these structure are small and the model resolution could not be enough to reproduce them. For the same reason probably, the small scale cyclonic system developed on the eastern side of Sicily in the observation is interpreted by the model as a single quite large cyclonic area.

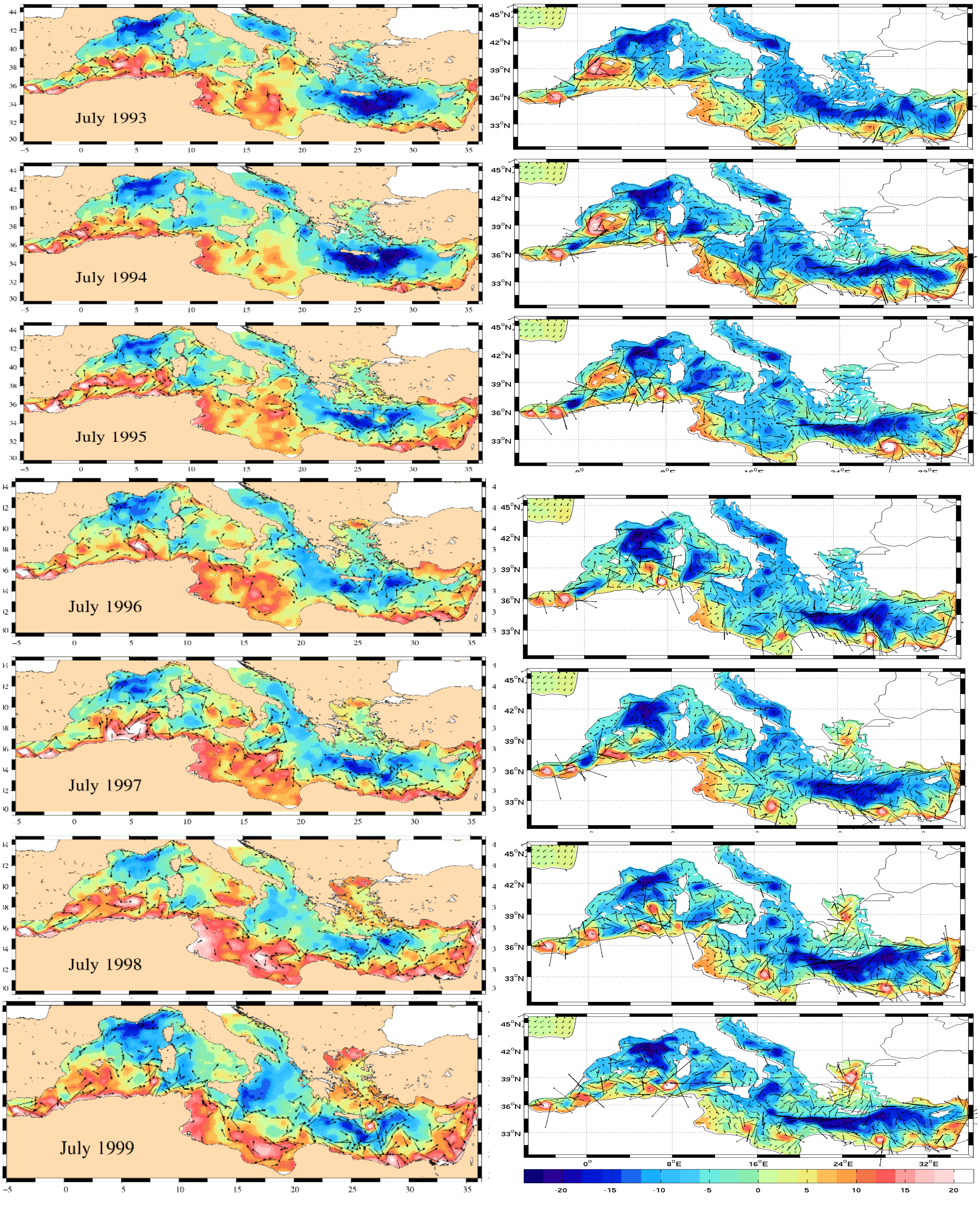

Figure 2-12 Monthly mean SLA [m] for July from 1993 to 1999. On the left there are the observations and on the right the model resuls.

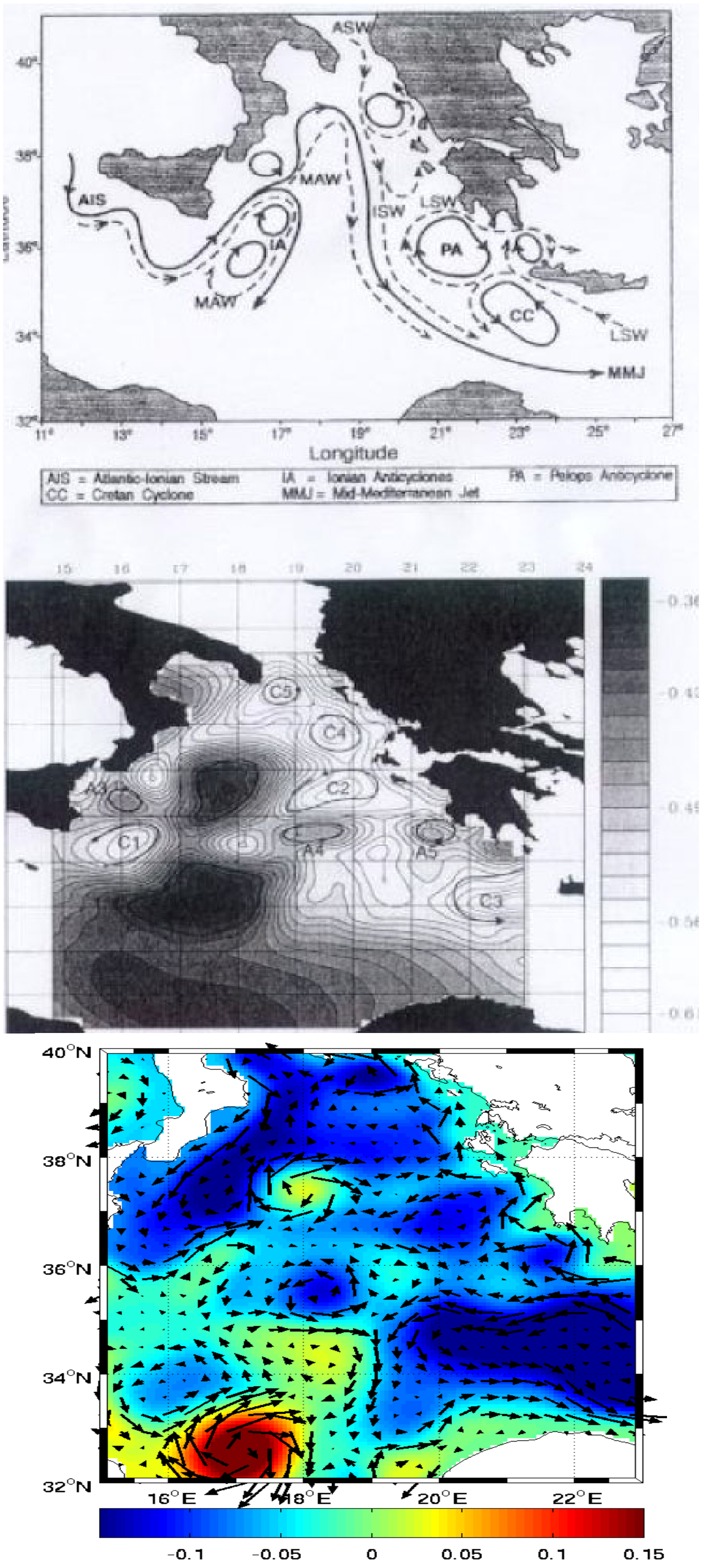

Figure 2-13 Schematic of the Ionian basin circulation (upper panel from Robinson and shellshopp, 2002), observed dynamic height [m] (central panel), model SSH [m] (lower panel)

3. Chapter: Development of the Partitioned Kalman Filter and Smoother

Kalman Filter and Rauch-Tung-Striebel Smoother (Gelb.1974) are one of the possible approaches to solve problems of estimation and control. In practice they are recursive least square estimators that performs model and observations averages weighted by their respective error covariances. The filter uses all the past observations up to the point at which the analysis is produced, the smoother uses instead observations both in the past and future with respect to the analysis time. The former is used to produce the initial condition for forecasting while the latter is mostly used in re-analysis or delayed mode analysis of the oceanic state.

The Partitioned Kalman Filter and Smoother (PKFS) is a method for approximating the Kalman Filter and Smoother method and scheme for oceanic and atmospheric data assimilation. Kalman Filter and Smoother can take into account the error dynamics and they provide estimates of the accuracy of their solution. In the other methods presented in this thesis, Optimal Interpolation (OI) and 3DVAR, there is normally no information about the data assimilation solution error. The price one pays with Kalman Filter and smoother is a larger computational cost.

Recently, Fukumori (ed. E.P. Chassignet and J. Verron, 2006) has described the differences between Kalman Filter and Smoother in a somewhat unconventional way. Let us assume that x is a prognostic variable of the model and u is a 'control variable', which can include lateral boundary conditions, forcing and sources of model errors. Given a set of observations y at different time t, the assimilation problem can be represented as:

$$\begin{pmatrix} Hx_t \\ Hx_{t+1} \\ \vdots \\ x_{t+1} - Ax_t - Gu_t \\ x_{t+2} - Ax_{t+1} - Gu_{t+1} \end{pmatrix} = \begin{pmatrix} y_t \\ y_{t+1} \\ \vdots \\ 0 \\ 0 \end{pmatrix} \qquad \text{eq: 3.1a}$$

The upper part of the equation 1 connects the observation to the model solution through the observational operator H while the lower part describes the temporal evolution of the model by A and G operators which embodied the physics and the dynamics of the model itself. We can think the Kalman Filter, as well as the OI and the 3DVAR, as algorithms which consider only the upper part of equation 3.1a, while the Smoother considers the entire set of equations and by doing that the Smoother can get a physically consistent solution of the problem, given that the dynamics can be linear and represented by the last two equations in (3.1a).

3.1 Theory of the Partitioned Kalman Filter and Smoother (PKFS)

In order to give some "insight" to the data assimilation problem it is worthwhile to introduce some fundamental concepts related to the data assimilation problem..

Let us assume that we have knowledge about the state of the ocean at time t, and we represent this by a "state analysis vector" x_t^a**.** A numerical model $M_{t,t+1}(x,u)$ describes the transition of the state vector from time t to time $t+1$:

$x_{t+1}^f = M_{t,t+1}(x,u)[x_t^a, u_t]^T$

where x_{t+1}^f is the vector describing the forecast state of the system, and u the control variables. In other words, the forecast is the prediction of a numerical model starting from an "analyzed estimate" of the state vector which is the best estimate of the state of the system.

In general M could be non linear, thus in order to apply the Kalman filter and smoother techniques, it is necessary to linearized it. We then write:

$A = dM/dx$

$G = dM/du$

so that the model can be approximated to:

$x_{t+1}{}^{f} \approx A_{t,t+1}(x) x_t{}^{a} + G_{t,t+1}(u) u_t.$ eq: 3.1b

Given an observation y at the time $t+1$ the Kalman Filter solution or analyzed state vector at time $t+1$, is written (Gelb,1974):

$$x^{a}_{t+1} = x^{f}_{t+1} + K_{t+1}\left(y_{t+1} - Hx^{f}_{t+11}\right) \qquad \text{eq: 3.2}$$

where the K_{t+1} is the Kalman gain defined as

$$K_{t+1} = B^{f}_{t+11} H^{T}\left(HB^{f}_{t+1} H^{T} + R\right)^{-1} \qquad \text{eq: 3.3}$$

where B^{f}_{t+1} is the background error covariance matrix at the time step $t+1$, H is the observational operator which transforms from model space to observational space and R is the error covariance matrix of the observations. The error covariance associated to the analyzed value can be written as:

$$B^{a}_{t+1} = B^{f}_{t+1} - B^{f}_{t+1} H^{T}\left[HB^{f}_{t+1} H^{T} + R\right]^{-1} HB^{f}_{t+1} \qquad \text{eq: 3.4}$$

The error associated to the forecast can evolve in time due to the numerical model dynamics; assuming that B_t^{f} is known at some time step t it is possible to forecast the error covariance evolution by using the so-called Riccati equation (Gelb,1974):

$$B^{f}_{t+1} = A\left\{B^{f}_{t} - B^{f}_{t} H^{T}\left[HB^{f}_{t} H^{T} + R\right]^{-1} HB^{f}_{t}\right\}A^{T} + Q \qquad \text{eq: 3.5}$$

where Q is the error covariance associated to the control variables.

Once all the filtered estimates are obtained the Smoother algorithm can give a new estimate by using the linearized dynamical equations in (3.1b). The algorithm which describes the Kalman Filter smoother is:

$$\begin{aligned} x^{s}_{t-1} &= x^{a}_{t-11} + S_{t-1}\left(x^{s}_{t} - x^{f}_{t}\right) \\ S_{t-1} &= B^{a}_{t-1} A^{T}\left(B^{f}_{t-1}\right)^{-1} \\ B^{s}_{t-1} &= B^{a}_{t-1} + S_{t-1}\left(B^{s}_{t-1} - B^{f}_{t-1}\right)S^{T}_{t-1} \end{aligned} \qquad \text{eq: 3.6a}$$

where S is the smoother gain, x^{s} is the smoother field, B^{s} is the error covariance associated to the smoother values. A useful way to re-write (3.6a) is the following form:

$$
\begin{aligned}
&x^s_{t-1} = x^a_{t-1} + S_{t-1}\left(x^s_t - x^f_t\right) \rightarrow \Delta S_{t-1} = S_{t-1}\{\Delta S_t + \Delta K_t\}\\
&\Delta S_t = x^s_t - x^a_t\\
&\Delta K_t = x^a_t - x^f_t\\
&B^s_{t-1} = B^a_{t-1} + S_{t-1}\left(B^s_t - B^f_t\right)S^T_{t-1}\\
&S_{t-1} = B^a_{t-1}A^T\left(B^f_{t-1}\right)^{-1}
\end{aligned}
\qquad \text{eq: 3.6b}
$$

Moreover the Kalman smoother can improve a posteriori the estimate of the control variables, because measurements contain information also about them in an indirect way. The equations to compute the smoothed control variables and their error covariance are reported below:

$$
\begin{aligned}
&u^s_{t-1} = u_{t-1} + F_{t-1}\left(x^s_t - x^f_t\right)\\
&Q^s_{t-1} = Q^a_{t-1} + F_{t-1}\left(B^s_t - B^f_t\right)F^T_{t-1}\\
&F_{t-1} = Q_{t-1}G^T\left(B^f_{t-1}\right)^{-1}
\end{aligned}
\qquad \text{eq: 3.7}
$$

The PKFS approximates all the above equations reducing the dimension of the model error covariance matrix B. This approach has been pioneered by Fukumori and co-authors. The basic assumptions are:

- Time-asymptotic approximation (Fukumori et al. 1993)
- State reduction (Fukumori and Rizzoli,1995)
- Partitioning of the state vector

The first approximation is justified because for stable and stationary dynamics represented by a stationary A with positive and less than 1 eigenvalues (Anderson and Moore, 1979), it is possible to show that the error covariance matrix, B, of the model reaches a quasi-stationary limit. This theorem is formulated only for linear models This approximation consists in using the asymptotic limit of the error covariance matrix instead of the time evolving one. There are several methods to find the time asymptotic of B, among them an efficient one is the doubling algorithm (Appendix A). The state reduction approximation consists in splitting the error structure in an horizontal and a vertical part. This method has been first demonstrated to be valid for oceanic data assimilation by De Mey and Robinson (1986) and never for the atmosphere. This approximation is justified by the fact that oceanic dynamics and thus error dynamics can be approximated by few vertical dynamical modes. Together with the reduction to few vertical modes in vertical, the B matrix is reduced in size also by using a coarser grid (assimilation grid) with respect to the numerical model grid (dynamical grid). While several authors have used vertical error reduction methods with Empirical Orthogonal Functions (EOF, De Mey and Benkiran, 2002), the method used here and derived by Fukumori (1999) uses the so-called dynamical modes.

Finally the partitioning consists in combining a series of reduced-state approximations that physically and statistically approximate errors of model state into independent elements (barotropic & baroclinic processes).

PKFS assumes the existence of a transformation by which the model state is approximated as a sum of l independent elements (or processes), $x'_1, x'_2, \ldots, x'_l$, with much fewer formal degrees of freedom than the model state x itself. Mathematically, applying this concept to the uncertainty δx we write:

$$\delta x \approx O_1 \delta x'_1 + O_2 \delta x'_2 + \cdots + O_l \delta x'_l \approx \left(O_1 O_2 \ldots O_l\right) \begin{pmatrix} \delta x'_1 \\ \delta x'_2 \\ \vdots \\ \delta x'_l \end{pmatrix} \approx O \delta x' \qquad \text{eq: 3.8}$$

where O_i denotes the particular transformation.

The model error covariance B^f and its inverse $(B^f)^{-1}$ can be then approximated as (Fukumori,1995):

$$\begin{aligned} B^f &\equiv \left\langle \delta x \delta x^T \right\rangle \approx O \left\langle \delta x' \delta x'^T \right\rangle O^T \approx O B' O^T \\ \left(B^f\right)^{-1} &\approx O^* \left(B^f\right)^{-1'} O^{*T} \end{aligned} \qquad \text{eq: 3.9}$$

where O* denotes the pseudoinverse of O and δx defines the error on the state vector x**.** If we take the Kalman filter gain (3.3), $K \approx B^f H^T \left(H B^f H^T + R^{-1}\right)$ this can be approximated as well as:

$$\begin{aligned} K &\equiv B^f H^T \left(H B^f H^T + R^{-1}\right) \approx \\ &\approx \left(\sum_i O_i B_i^{f'} O_i^T\right) H^T \left(H \left(\sum_i O_i B_i^{f'} O_i^T\right) H^T + R^{-1}\right) \approx \\ &\approx \sum_i O_i B_i^{f'} H_i'^T \left(H \left(\sum_i O_i B_i^{f'} O_i^T\right) H^T + R^{-1}\right) \approx \sum_i O_i K_i' \end{aligned} \qquad \text{eq:3.10}$$

where $\begin{cases} H_i^{'} \equiv HO_i \\ K_i^{'} \equiv B_i^{f'} H_i^{'T} \left(H \left(\sum_i O_i B_i^{f'} O_i^T \right) H^T + R^{-1} \right) \end{cases}$ are the observation matrix and the Kalman gain for the i^{th} element. Similarly the smoother gain can be approximated as:

$$S \equiv B^a A^T \left(B^f\right)^{-1} \approx \left(\sum_i O_i B_i^{a'} O_i^T \right) A^T \left(\sum_j O_j^{*T} B_i^{f'} O_j^* \right)^{-1} \qquad \text{eq: 3.11}$$

The Smoother gain can be further approximated assuming that the variations within a partition remain independent from the space spanned by the other elements, that is $O_j^* A O_i \approx 0$ when i≠j.

$$S \approx \sum_i O_i B_i^{'} A_i^T \left(B_i^f\right)^{-1} O_i^* \approx \sum_i O_i S_i^{'} O_i^* \qquad \text{eq: 3.12}$$

where $A_i^{'} \equiv O_i^* A O_i$ is the reduced state transition matrix corresponding to the i^{th} element. Likewise $S_i^{'} \equiv B_i^{'} A_i^{'T} \left(B_i^{'f}\right)^{-1}$ is the smother gain for the i^{th} element of the partition.

In the PKFS used in this thesis we will use a transformation that will subdivide the model state variables and errors in baroclinic and barotropic modes, as it will be discussed later.

3.2 How to assess the product of an assimilation scheme

Usually in data assimilation problems for the ocean and the atmosphere there are more state vector variables to be estimated than measurements, thus the inverse problems are rank deficient. There exist an infinite number of solutions that could reduce the model data difference. The assessment of the assimilation must be evaluated carefully based on self consistency and independent data (Fukumori et al. 1999).

Concerning the consistency of the solution it is convenient to introduce the following relations (Gelb.1974):

$$\left\langle \left[y - H\left(x^{sim}\right)\right]\left[y - H\left(x^{sim}\right)\right]^T \right\rangle = R + HB^{sim}H^T$$
$$\left\langle \left[y - H\left(x^{f}\right)\right]\left[y - H\left(x^{f}\right)\right]^T \right\rangle = R + HB^{f}H^T \qquad \text{eq: 3.13}$$
$$\left\langle \left[y - H\left(x^{a}\right)\right]\left[y - H\left(x^{a}\right)\right]^T \right\rangle = R - HB^{a}H^T$$

where B^{sim}, B^f, B^a, are the error covariance matrices of the simulation, forecast and analysis respectively. B^{sim} may be computed from the variances assuming that the error is proportional to the variability of the dynamical fields.

From this system it is possible to write the equations for two quantities which measure the skill of the forecast relative to the simulation, and those of the analyzed solution respect to the forecast one. They are:

$$\left\langle \left[y - H\left(x^{sim}\right)\right]\left[y - H\left(x^{sim}\right)\right]^T \right\rangle - \left\langle \left[y - H\left(x^{f}\right)\right]\left[y - H\left(x^{f}\right)\right]^T \right\rangle = HB^{sim}H^T - HB^{f}H^T$$
$$\left\langle \left[y - H\left(x^{f}\right)\right]\left[y - H\left(x^{f}\right)\right]^T \right\rangle - \left\langle \left[y - H\left(x^{a}\right)\right]\left[y - H\left(x^{a}\right)\right]^T \right\rangle = HB^{a}H^T + HB^{f}H^T \qquad \text{eq: 3.14}$$

The first equation of 3.14 measures the ability of the model to keep the correction information and to propagate it consistently in time, the latter is an indication of the quality of the forecast with respect to the analysis (Fukumori et al. 1999).

The comparison with independent data can address the question of the accuracy of the solution but usually in the reanalysis experiments it is quite difficult to find independent measurements because the accuracy increase assimilating as much data as possible so there is a tendency to assimilate all the available measurements.

Moreover, if everything is consistent, the error associated with the simulation should be higher than the error associated with the forecast which in turn should be higher than the error associated to the analysis; their theoretical values should reflect that behavior too.

3.3 Academic case study

The objective of this study is to evaluate the capacity of the PKFS to give a satisfactory solution to the estimation problem, given the many approximations needed to make it working. We decided then to study its behavior in an academic modeling framework such as a barotropic steady state model. We will verify and test only the approximations related to the order reduction in horizontal, the steady state assumptions and the approximations to the Kalman gain. The PKFS software has been coded in an original form and it works on PC cluster. The stability of the code and its results has been checked also on a vector machine as NEC-SX6 supercomputer.

3.3.1 Numerical Model and twin experiment

The numerical model employed in this study is based on the OPA 8.1 code implemented for a barotropic, mid-altitude ocean. The model domain is a squared closed box with flat bottom, located from 20 to 70 degrees north. The grid is composed by 50x50 points and model resolution is 1 degree. An implicit free surface scheme is chosen in order to have the sea surface height as prognostic variable. No slip lateral boundary conditions are imposed. Constant values for horizontal viscosities are selected, as well as for the quadratic bottom drag coefficient.

Using the same formalism in chapter 2,the momentum equations are then:

$$
\begin{cases}
\dfrac{\partial u}{\partial t} - fv = -g\dfrac{\partial \eta}{\partial x} + A_v\dfrac{\partial u}{\partial z} \\
\dfrac{\partial v}{\partial t} + fu = -g\dfrac{\partial \eta}{\partial y} + A_v\dfrac{\partial v}{\partial z} \\
\dfrac{\partial \eta}{\partial t} + \dfrac{\partial}{\partial x}\left(uH_0\right) + \dfrac{\partial}{\partial y}\left(vH_0\right) = 0
\end{cases}
$$

where the boundary conditions for the surface are:

$$
A_v \left.\frac{\partial u}{\partial z}\right|_{z=\eta} = \tau_w^x
$$

$$
A_v \left.\frac{\partial v}{\partial z}\right|_{z=\eta} = \tau_w^y
$$

and the boundary condition for the bottom are:

$$A_v \left.\frac{\partial u}{\partial z}\right|_{z=-H} = \rho_o c_d |u_b| u_b$$

$$A_v \left.\frac{\partial v}{\partial z}\right|_{z=-H} = \rho_o c_d |v_b| v_b$$

The momentum flux is given by a simple analytical wind stress of the form:

$$\tau_x(j) = -\tau_0 \cos\left(\frac{\pi\theta_j^*}{\theta_0}\right)$$

where $\theta_0 = \theta_{\max} - \theta_{\min}$ and $\theta_j^* = \theta_j - \theta_{\min}$

The solution of this problem is the well known mid-latitude steady state anticyclonic gyre with the western boundary intensification (Pedlosky, 1987). The solution will be a mixture of Munk and Stommel solutions since we have chosen to use both the horizontal viscosity and the bottom drag.

In order to show the impact of PKFS we need to set up an experiment where observations are used to “correct” the model solution which is deviated from reality. In an academic test case such as ours, we use the method of the “twin experiments”. We assign one experiment to represent ‘truth’ while we set up another ‘perturbed’ experiment (called simulation thereafter) to be the deviated model solution. We then take synthetic observations or pseudo-observations from the true model and we try to insert them in the deviated model trying to bring it toward the “true” solution.

In our case we have decided also to use as “control variable” the wind stress: this is an interesting choice since many of the model errors in the complex oceanic problem can be related to the inaccurate knowledge of the wind stresses and hopefully we will learn more on how to do the complex oceanic case.

The barotropic wind driven gyre is clearly a privileged study case since many of the basic assumptions of the PKFS can be considered valid. In particular it is a linear solution of the model equations and the dynamical equations can be really written as in 3.1b. Thus in our case, the PKFS is used to correct errors on the winds by inserting pseudo-observations in the simulation to obtain the analysis which should be our best estimate of the “truth”. If the assimilation scheme works the analyzed state should be closer to the true state then the simulation one.

3.3.2 The PKFS implementation

Following out previous discussion, the PKFS will be defined on a coarser resolution grid. Such an assimilation grid is composed by 10x10 points with a resolution of 5 degrees. Figure 3-1 shows the model (fine resolution, light lines) and the assimilation grid (coarse resolution, heavy line). The red dots in that figure are the locations where the pseudo-observations are sampled.

In this twin experiment we take 100 pseudo-observations of sea surface height sampled from the “true state” every day at the observational points of Figure 3-1. Once the pseudo-observation are sub-sampled “from the truth”, a spatially independent white noise is added to the measurements: the added noise variance is $1e^{-6}$ m. This choice is dictated by two very different considerations: from one hand we want reproduce as much as possible realistic applications where observations have errors, on the other hand adding that noise to the observations justify the existence of a diagonal matrix R. The data error covariance matrix R helps the convergence of the doubling algorithm since it is an added diagonal term in the Kalman gain (equation: 3.3) and if B is close to be singular it will make the inverse more stable.

The choice of the horizontal PKFS grid has to be done optimizing the accuracy of the solution and the computational time required to implement and run the assimilation model. Clearly from the accuracy point of view the best solution should be to have a PKFS grid equal to the OGCM grid, however this choice increase dramatically the dimension of the problem and then the computational time required. Eventually the grid of PKFS has to be chosen as a compromise between accuracy of the solution and computer time available.

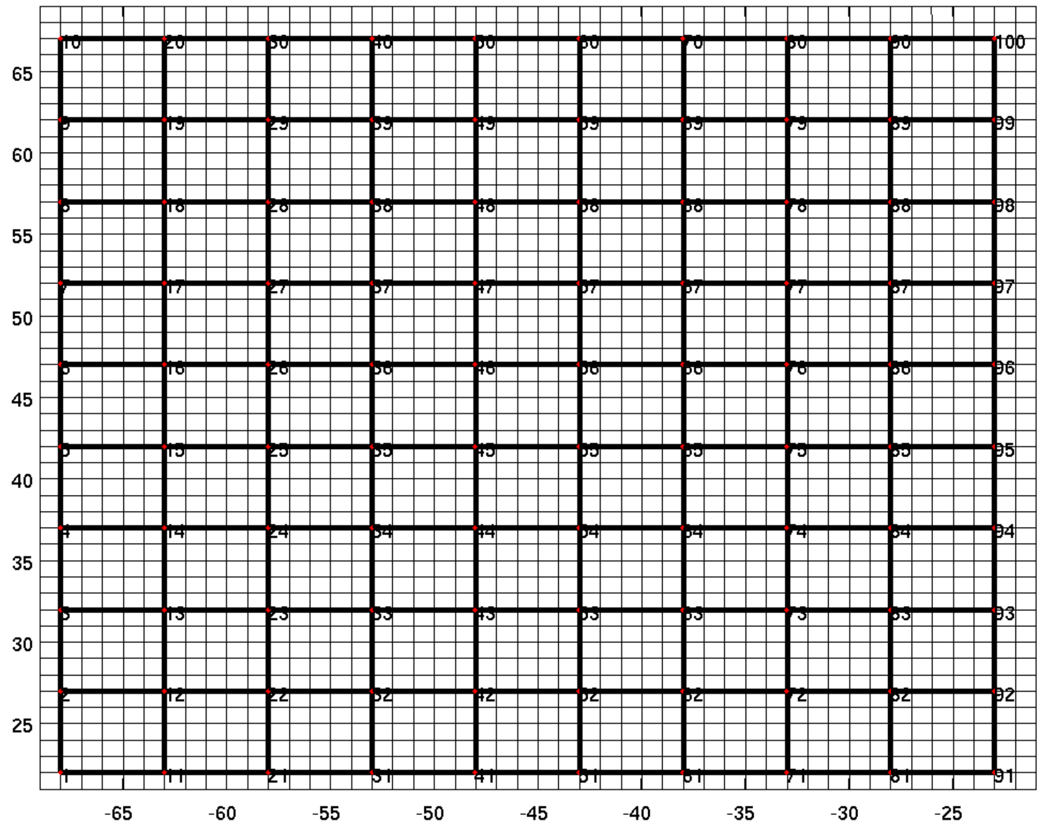

Figure 3-1: Locations of the observation (red dots) respect to fine grid (light lines), coarse grid(heavy lines).

Once the PKFS grid has been chosen the objective mapping operator has to be implemented. This operator, which can be modeled as a matrix, performs the transformation from the coarse to the fine grid and its pseudo-inverse performs the transformation from the fine to the coarse grid. The upper panel of Figure 3-2 is an example of the transformation from coarse to fine grid. The resulting fine representation is transformed back to the coarse grid again and it is shown in the bottom panel of the same figure. The starting vector of the transformation is a coarse vector of zeros except in one coarse grid point where the value is forced to be one (not shown). The representation of the starting coarse field is practically identical to the bottom panel of Figure 3-2. The perfectly good agreement between the original field and the coarse grid field obtained after the objective analysis demonstrates that the operator is well computed.

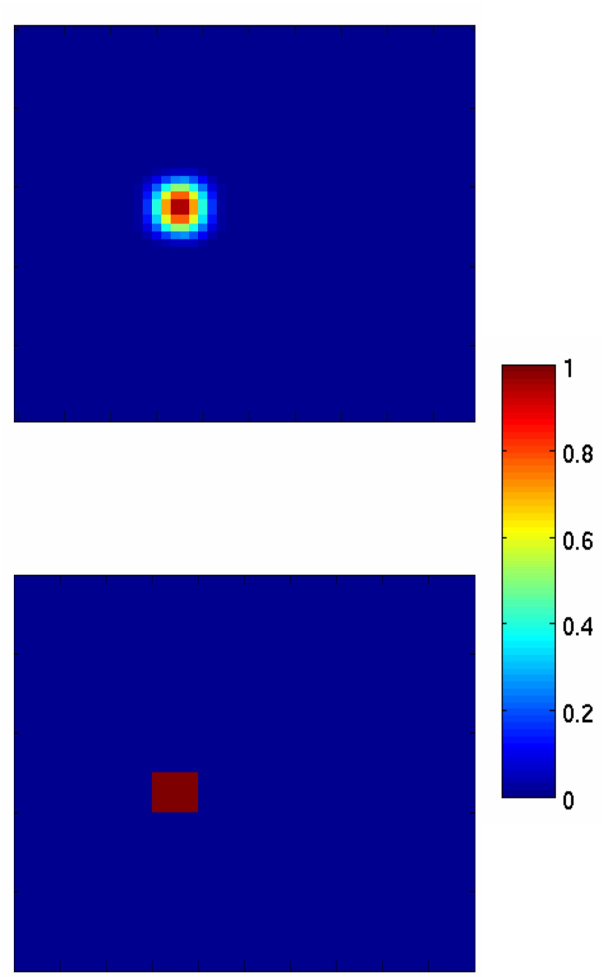

Figure 3-2: Top panel result transformation coarse to fine grid . Bottom panel result transformation fine to coarse grid

The most time consuming part of the implamantation of the PKFS is the estimation of the transitions matrices. Since the dynamical model is barotropic the state vector is composed of barotropic zonal and meridional current velocities and the sea surface height:

$$x = \begin{vmatrix} \eta_{bt} \\ u_{bt} \\ v_{bt} \end{vmatrix}$$

The control variables are the zonal and meridional wind stress that is:

$$u = \begin{vmatrix} \tau_x \\ \tau_y \end{vmatrix}$$

The state transition matrix A**,** the control transition matrix G**,** and the observation matrix H**,** are computed using a Green function method. which consists of perturbing each state variable at each model grid point and run the numerical model for a period which should be equal to the assimilation time period which in this case is one day. Then the amplitude of the barotropic mode is computed from the difference between the perturbed and the unperturbed fields.

It is possible to define the j^{th} column of the linearized state transition matrix as:

$$(\mathrm{A})_j = \frac{\partial M}{\partial \mathrm{x}} \mathrm{e}_j \approx M\left(\mathrm{x}_{t-1} + \mathrm{e}_j, \mathrm{u}_{t-1}\right) - M\left(\mathrm{x}_{t-1}, \mathrm{u}_{t-1}\right) \qquad \text{eq: 3.15}$$

where M is the non linear model, x is the state vector, u is the control variable, and e_j is a vector of zeros except for j^{th} value which is one. Once the state transition matrix is computed it is necessary to investigate its stability. In order to be stable the maximum eigenvalues of A should be less then one. In our case it is 1.225 then A is unstable thus it is forced A to be stable normalizing it by 0.999:

$$\mathrm{A} = \Lambda\lambda\Lambda^{-1}$$

$$\mathrm{A}_{stable} = \Lambda\lambda\left(\mathrm{I} \cdot \frac{0.999}{\max(\lambda)}\right)\Lambda^{-1}$$

From now on the subscript "stable" will be omitted for convenience but A_{stable} will be used instead of A.

In order to evaluate how good the linear-coarse model A can simulate the behavior of the full resolution non linear one (M) we show an example of how a perturbation of the sea surface height is propagated by the two models. Figure 3-3 shows the sea surface height initial perturbation which is equal for the two models. The top panels of the Figure 3-4, Figure 3-5, and Figure 3-6, show an example of the results of the computation for one day time integration of the equation:

$$\mathrm{x}_{t+1} \approx \mathrm{Ax}_t + \mathrm{Gu}_t$$

where G is the control transition matrix and u_t is equal to zero. The bottom panels of the same figures show the results of the computation of the full non linear model for the same period of time and with the same control variable value, u_t, that is:

$x_{t+1}=M_{t,t+1}(x,u)[x_t , u_t]^T$.

In particular the upper panels of the Figure 3-4,Figure 3-5, and Figure 3-6 are a representation of sea surface height, zonal and meridional velocity respectively using the linear coarse model (A) while the lower panels are a representation of the same variables for the nonlinear-fine model (*M*). Similarities between the two solutions confirm the good approximation of the linear-coarse model respect to the full resolution non linear one. It is interesting to notice that the response to the SSH perturbations is however non-local (due to fast barotropic wave dynamics) that makes it hard to do data assimilation, even if the chosen study case is extremely simple with respect to ocean dynamics. We shall furthermore keep in mind that the similarity between the A and M models is very case-dependent and that the similarity could not be as good for more realistic problems.

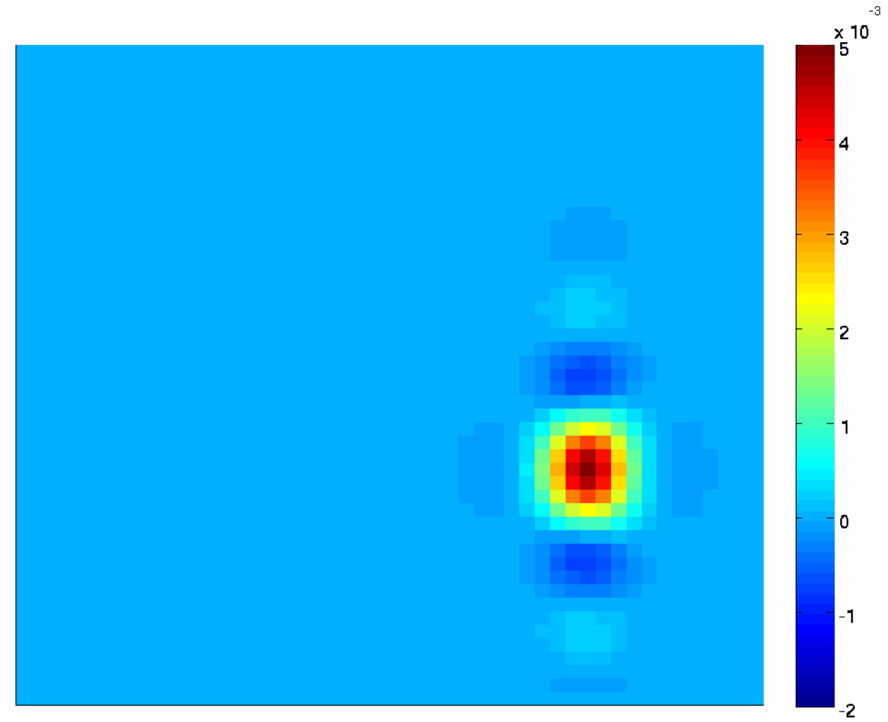

Figure 3-3: Initial perturbation of the Sea Surface Height (m) for both A and M models.

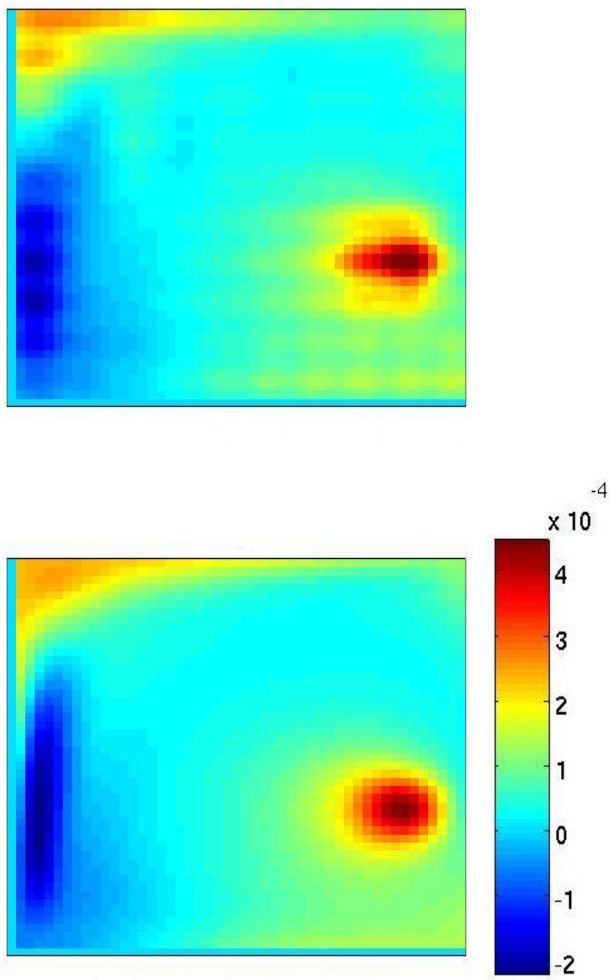

Figure 3-4: Top panel: Sea Surface Height estimated by linear model (A) after 1 day, Bottom panel: Sea Surface Height estimated by the non-linear model (M) after 1 day

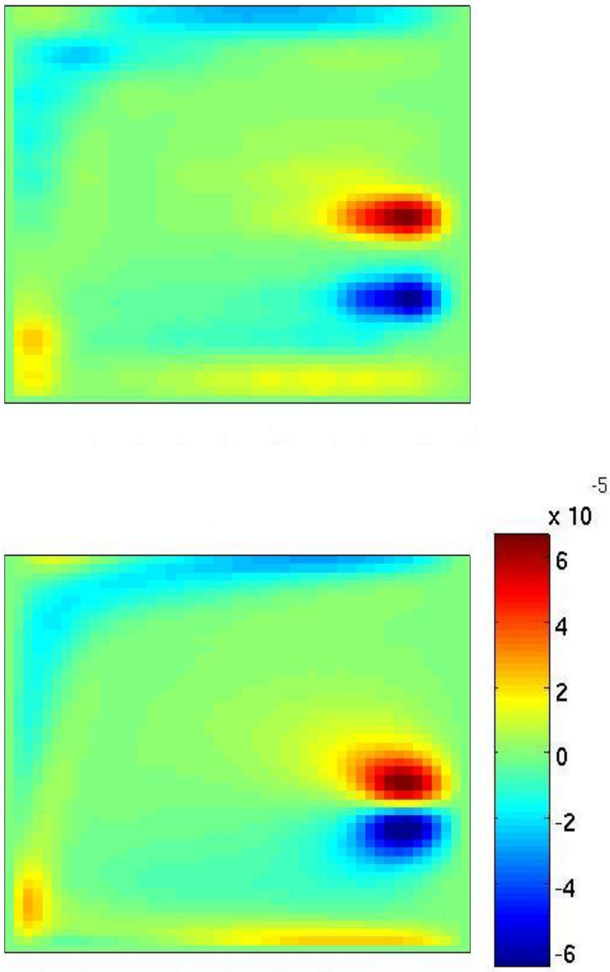

Figure 3-5: Top panel: Zonal velocity estimated by linear model (A) after 1 day, Bottom panel: Zonal velocity estimated by full non-linear model (M) after 1 day

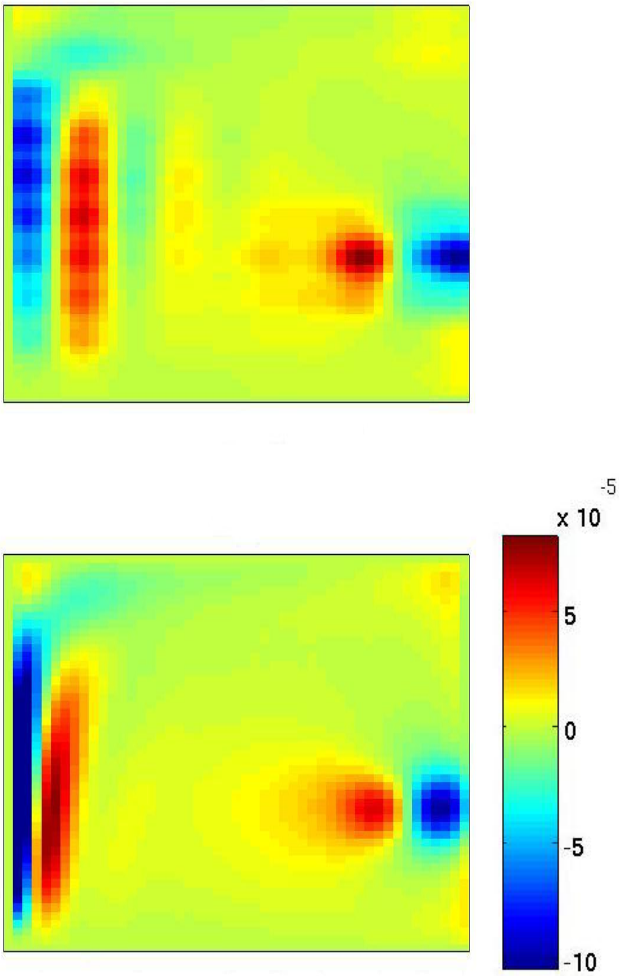

Figure 3-6: Top panel: Meridional velocity estimated by linear model (A) after 1 day, Bottom panel: Meridional velocity estimated by the non-linear model (M) after 1 day

The time asymptotic limit of the model error covariance matrix is found integrating the model A many times, as shown by the Riccati equation (3.5), it is worthwhile to see if the state transition matrix can approximate the non linear full resolution model for a longer period. Figure 3-7 shows an example of the initial zonal velocity perturbation and Figure 3-8,Figure 3-9,Figure 3-10, illustrate the propagation of that perturbation after three days with the full resolution non linear model and the coarse linear one. As expected the similarities are less than the previous 1 day case but is the solution is still very similar.

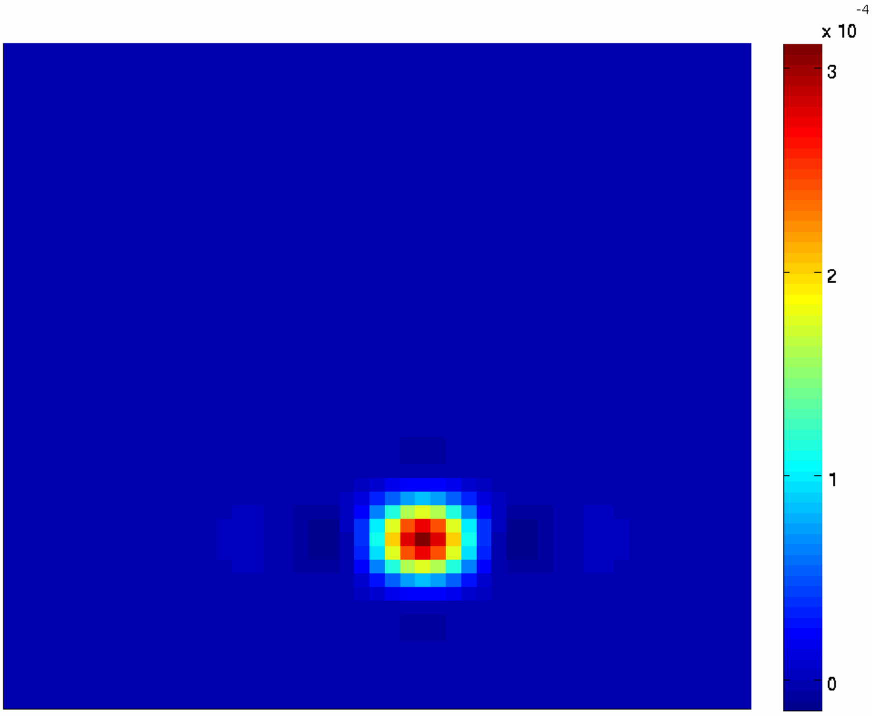

Figure 3-7; Initial perturbation of the zonal velocity (ms^{-1}).

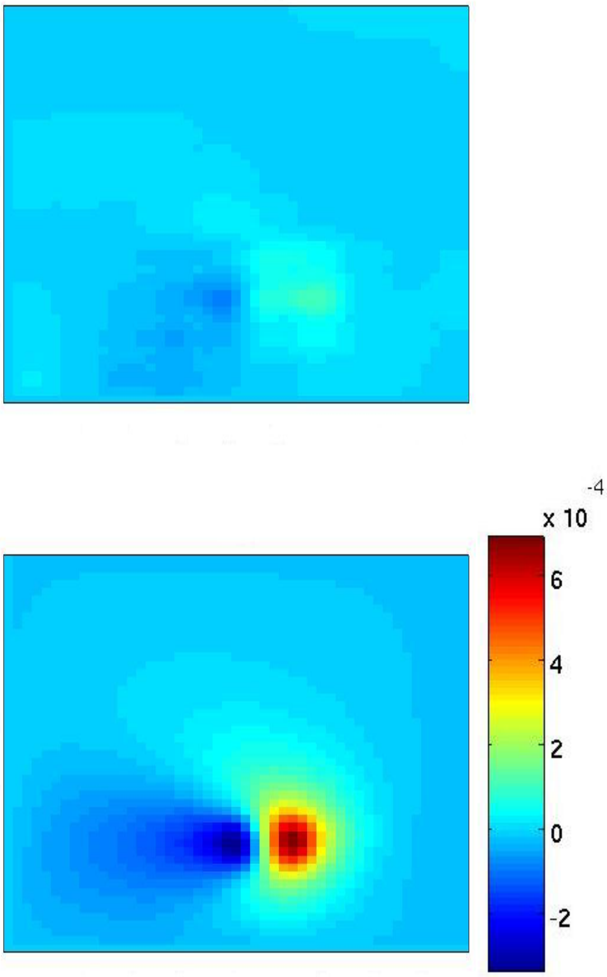

Figure 3-8: Top panel: Sea Surface Height estimated by linear model (A) after 3 days, Bottom panel: Sea Surface Height estimated by the non-linear model (M) after 3 days

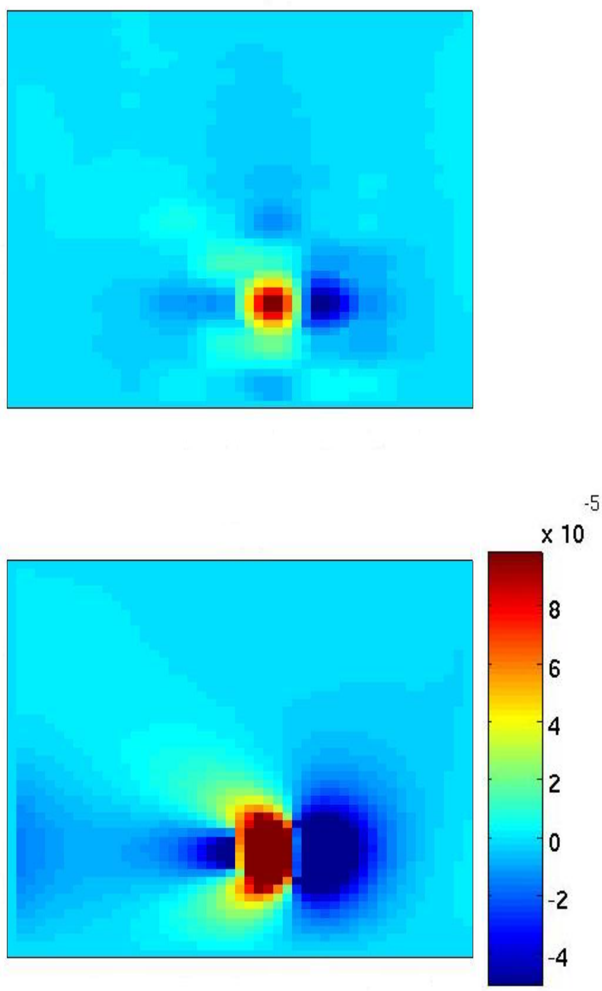

Figure 3-9: Top panel: Zonal velocity estimated by linear model (A) after 3 days. Bottom panel: Zonal velocity estimated by the non-linear model (M) after 3 days

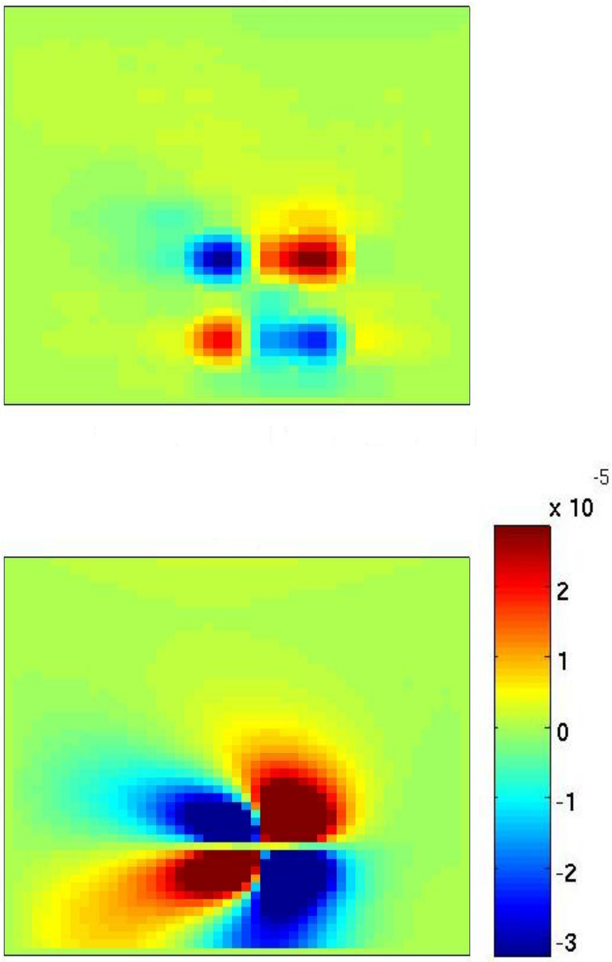

Figure 3-10: Top panel: Meridional velocity simulated by linear model (A) after 3 days. Bottom panel: meridional velocity simulated by the non-linear model (M) after 3 days

The control transition matrix is built using the same approach that we used for A but perturbing the control variables. In fact, similarly to A, the j-th column of the control transition matrix is defined as:

$$(\mathrm{G})_{\mathrm{j}} = \frac{\partial M}{\partial \mathrm{u}} \mathrm{e}_{\mathrm{j}} \approx M\left(\mathrm{x}_{\mathrm{t}-1}, \mathrm{u}_{\mathrm{t}-1} + \mathrm{e}_{\mathrm{j}}\right) - M\left(\mathrm{x}_{\mathrm{t}-1}, \mathrm{u}_{\mathrm{t}-1}\right) \quad \text{eq: 3.16}$$

Figure 3-11 shows an example of the zonal wind stress initial perturbation. The top panels of the Figure 3-12,Figure 3-13,Figure 3-14 show the evolution of that perturbation calculated using the coarse resolution linear model ($\mathrm{x}_{\mathrm{t}+1} \approx \mathrm{Ax}_{\mathrm{t}} + \mathrm{Gu}_{\mathrm{t}}$); while the bottom panels using the full resolution non-linear model ($\mathrm{x}_{\mathrm{t}+1} = M_{t,t+1}(\mathrm{x,u})[\mathrm{x}_{\mathrm{t}}, \mathrm{u}_{\mathrm{t}}]^{\mathrm{T}}$). Since there is good aggrement between top and bottom panels we can conclude that the linearization the full non linear model with respect to the control variable (τ_x) is a good approximation of *M*.

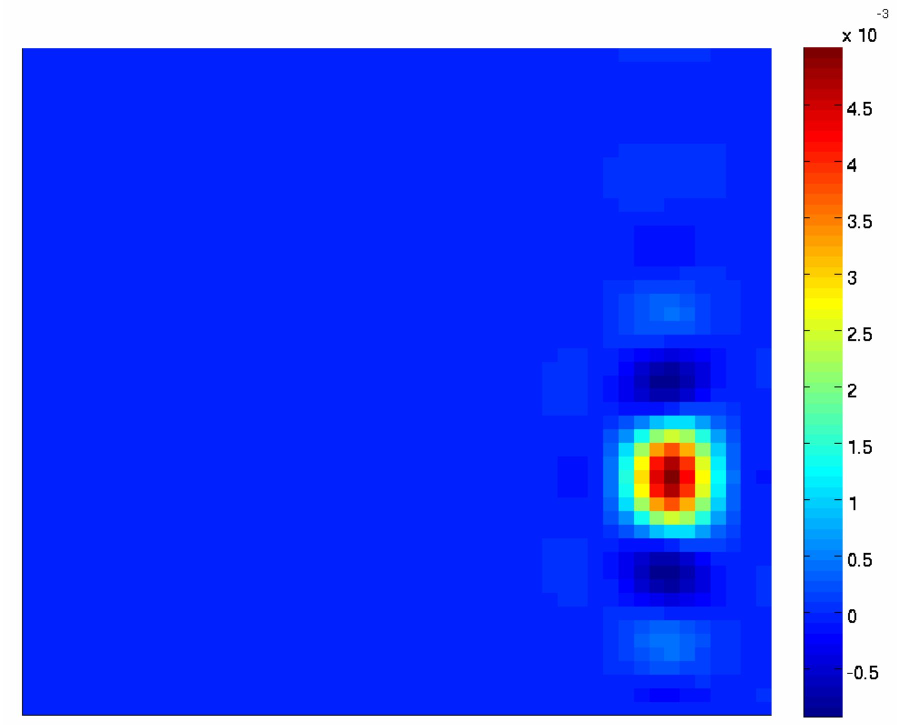

Figure 3-11: Initial perturbation of the zonal wind stress

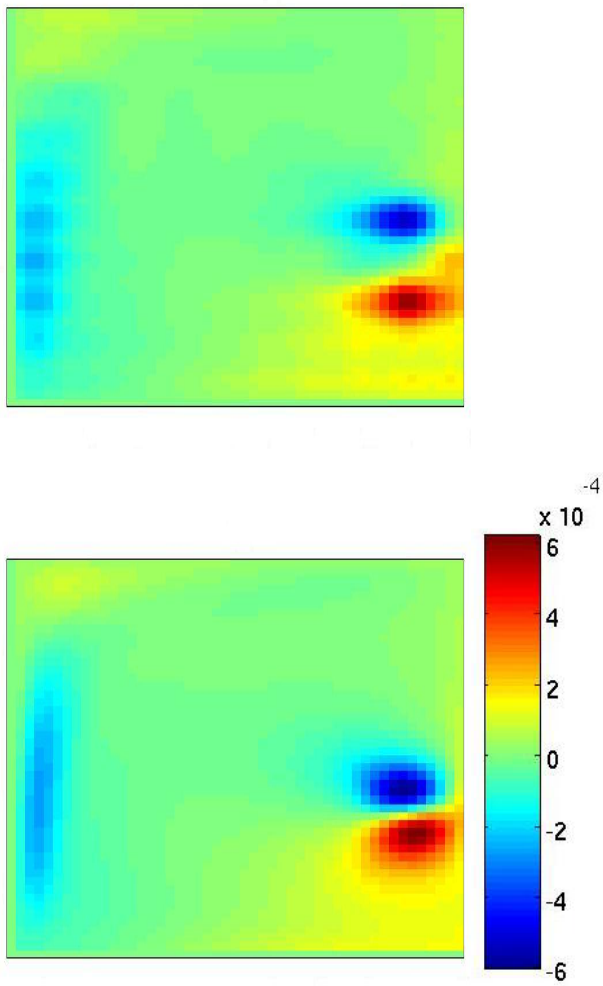

Figure 3-12: Upper panel: Sea Surface Height estimated by the linear model (G) after 1 day, Bottom panel: Sea Surface Height estimated by the non-linear model (M) after 1 day

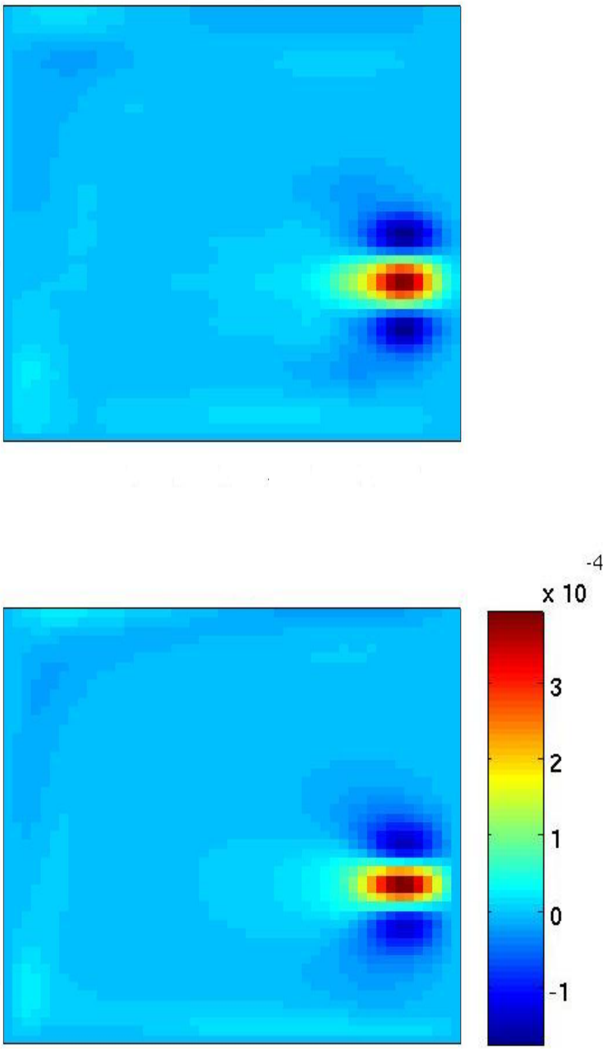

Figure 3-13:Top panel: Zonal velocity estimated by linear model (A) after 1 day, Bottom panel: Zonal velocity estimated by the non-linear model (M) after 1 day

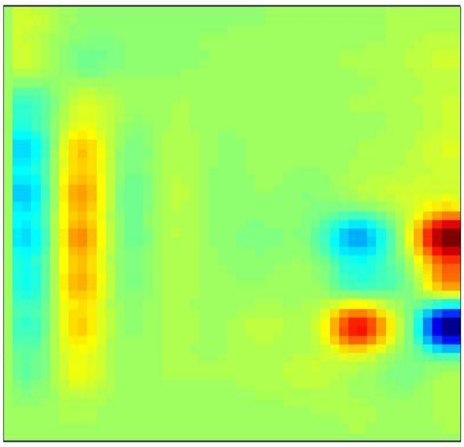

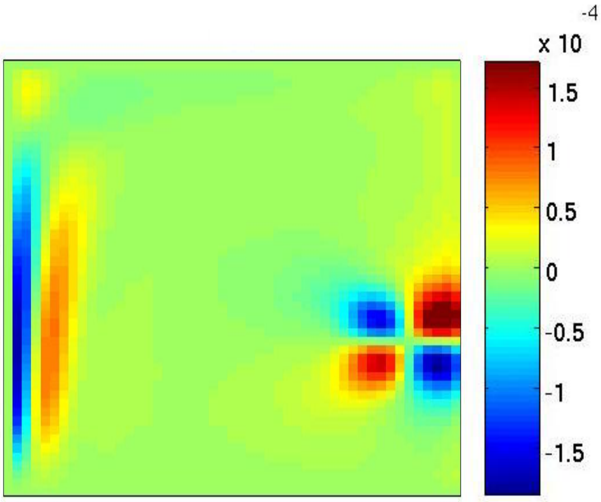

Figure 3-14:Top panel: Meridional velocity estimated by linear model (G) after 1 day, Bottom panel: Meridional velocity estimated by the non-linear model (M) after 1 day

The last operator which has to be linearized is the observation operator, which transforms the state vector from the model space to the observational space.

The linearization of H is obtained applying the same Green's function method: the j-th columns of the observation matrix are defined as:

$$(\mathrm{H})_j = \frac{\partial H}{\partial \mathrm{x}} \mathrm{e}_j \approx H(\mathrm{x} + \mathrm{e}_j) - H(\mathrm{x})$$

The Figure 3-15 represents the Sea Surface Height in the model space (right panel), and in the observation space (left panel). The dots are the location of the observations and their colors corresponds to the value of the Sea Surface Height. In this case the correspondence is perfect since observations are located at model grid points so that H is only a subsampling operator of the perturbed model solution.

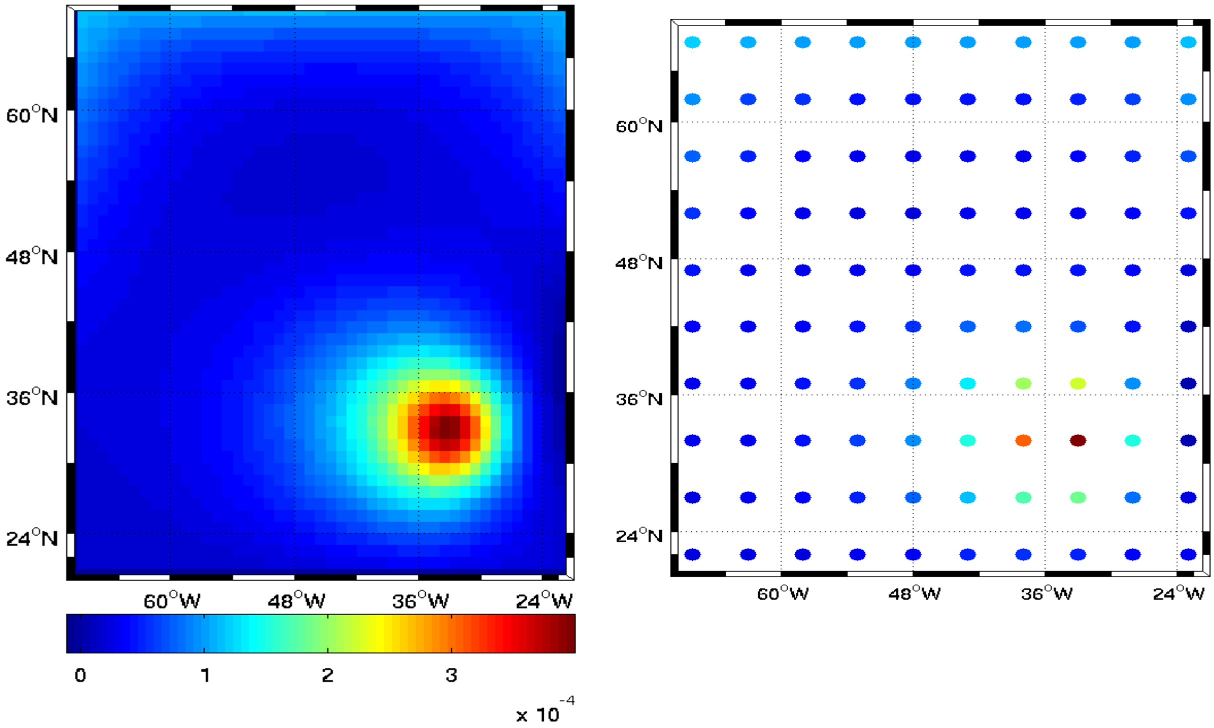

Figure 3-15:Representation of the Sea Surface Height in the model space and in the observational space.

3.4 Test of the PKFS method applied to the academic case

3.4.1 Steady State case

The first application of the PKFS is a for a steady state academic case with zonal only winds. The ‘true’ solution of this steady state case is a “Stommel-like circulation” whose analytical solution is well known, allowing us to speculate on the limitations of some of the approximations done in PKFS.

The “truth” is constructed integrating the model from the state of rest for 600 days with a temporally constant, but latitudinal varying, zonal wind stress. The meridional wind stress is imposed to be zero everywhere. The zonal wind stress assumes a sinusoidal shape with values ranging from -0.01 N/m^2 at 20 degrees north (southern boundary of the domain) and +0.01 at 70 degrees north (northern boundary of the domain). After a spin up period, the model sets on its equilibrium reproducing a "Stommel-like" solution which is shown in Figure 3-16. Pseudo-observations will be sampled from the 'truth' from the last 300 days of the 'truth' experiment.

The perturbed simulation state is computed using a different wind stress forcing. The zonal wind stress is equal to the one used in the true state solution, while the meridional wind stress assumes values different from zero. The meridional wind stress is constant with latitude but varies longitudinally in a sinusoidal way. The values at the East and West boundaries are zero and in the center of the domain is maximum, about 0.01 N/m^2. Figure 3-16 shows the steady state solution for the "simulated" state. The error in the wind stress is constant in time and it is shown in the Figure 3-17

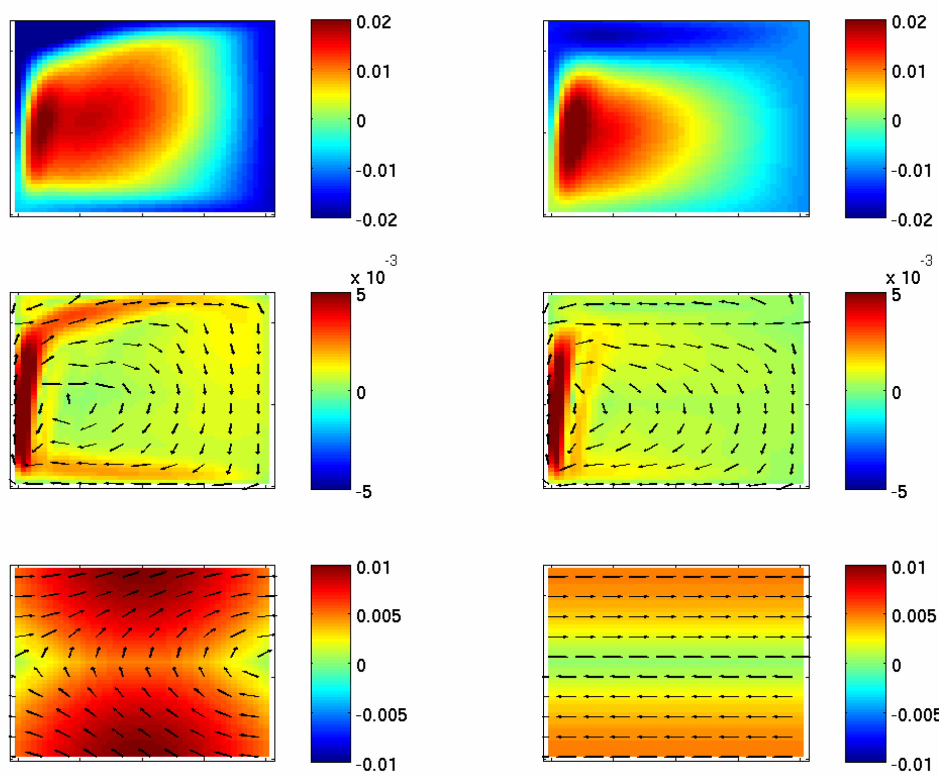

Figure 3-16 Left column: Steady state Sea Surface Height (m), Velocity (m/s), Wind Stress(N/m^2) respectively for the simulation, Right column: steady state Sea Surface Height (m), Velocity (m/s), Wind Stress(N/m^2) respectively for the "truth"

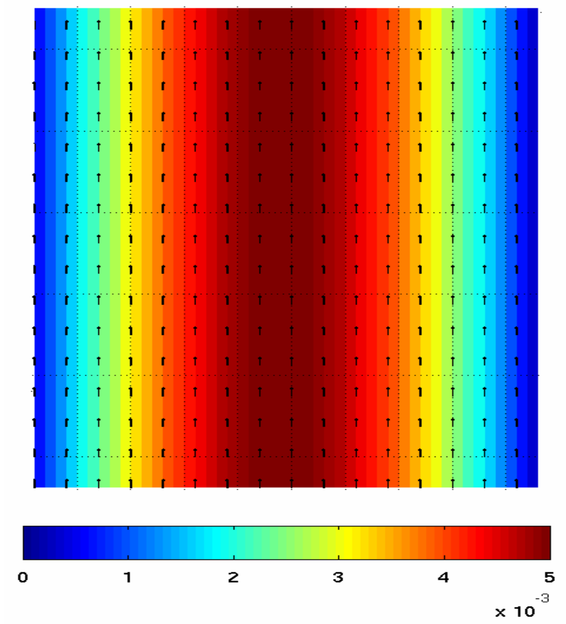

Figure 3-17: Root mean square error of the Wind Stress used to force the simulation run (Nm-^{2})

Figure 3-18 shows the sea surface height values on the pseudo-observational points. The pseudo-observations are obtained adding a white noise to the true values. As soon as the noise is added the measurements become time dependent, oscillating around their exact values (green circle Figure 3-18).

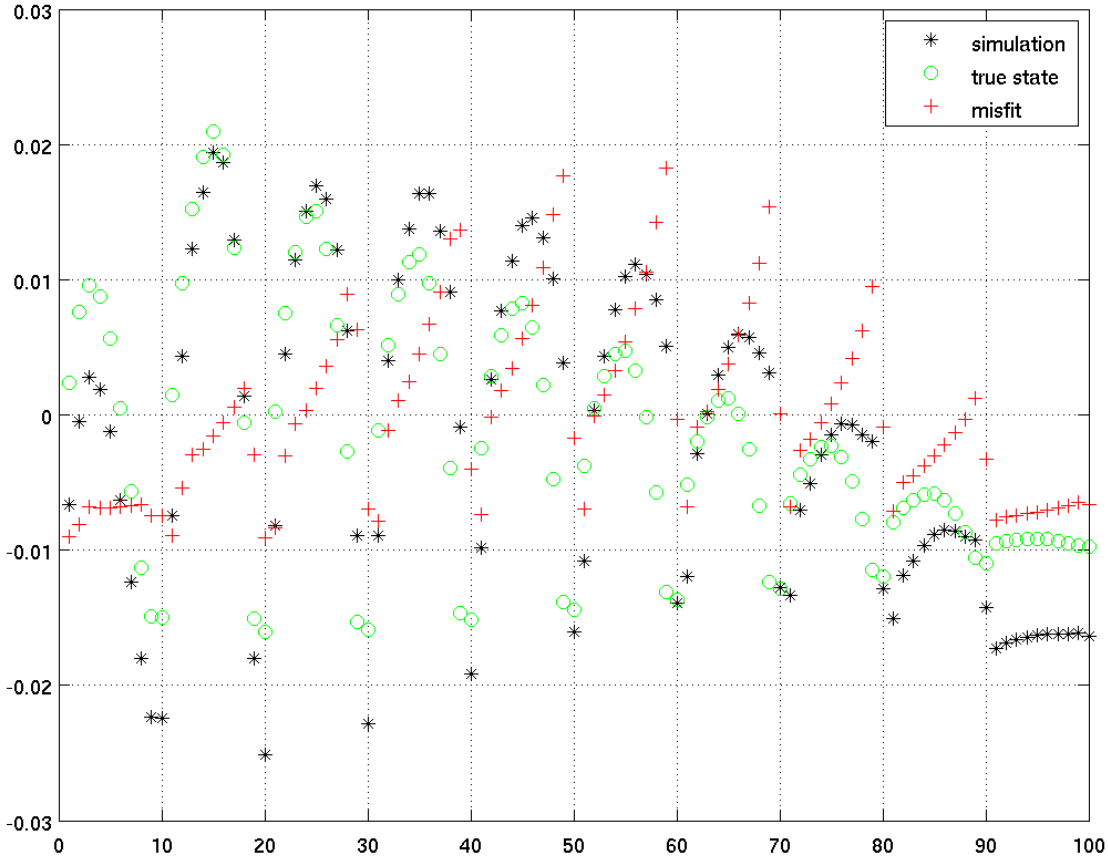

Figure 3-18 Sea surface height values sub sampled in the measurements positions for simulation (black asterisks), true state (green circle) and their difference (red crosses) . The numbers on the abscissa correspond to the position of the measurements shown in Figure 3-1.

Since in our case the error add to the pseudo-observations has been modelled to be uncorrelated in space and with variance of $1e^{-6}$ m^2, the error covariance matrix of the observations R is chosen to be diagonal with uniform vales of $1e^{-6}$ m^2.

Moreover because in our case the error is all concentrated in the control variable of the wind stress, the first guess of the error associated to the forecast can be modeled as:

$$B^f_{first\_guess}=GQG^T \qquad \text{eq: 3.17}$$

where G is the control transition matrix (eq: 3.16) and Q error covariance matrix of the control variables (eq: 3.5). In this experiment it is decided to be as much conservative as possible imposing the covariances of the error of the control variable and of the observational equal to zero. In particular the Q matrix is defined as:

$$
Q = \left|\begin{array}{cc|cc}
\langle \delta\tau_x^i \delta\tau_x^i \rangle & \langle \delta\tau_x^j \delta\tau_x^i \rangle & \langle \delta\tau_x^i \delta\tau_y^i \rangle & \langle \delta\tau_x^j \delta\tau_y^i \rangle \\
\langle \delta\tau_x^j \delta\tau_x^i \rangle & \langle \delta\tau_x^j \delta\tau_x^j \rangle & \langle \delta\tau_x^j \delta\tau_y^i \rangle & \langle \delta\tau_x^j \delta\tau_y^j \rangle \\
\hline
\langle \delta\tau_y^i \delta\tau_x^i \rangle & \langle \delta\tau_y^j \delta\tau_x^i \rangle & \langle \delta\tau_y^i \delta\tau_y^i \rangle & \langle \delta\tau_y^j \delta\tau_y^i \rangle \\
\langle \delta\tau_y^j \delta\tau_x^i \rangle & \langle \delta\tau_y^j \delta\tau_x^j \rangle & \langle \delta\tau_y^j \delta\tau_y^i \rangle & \langle \delta\tau_y^j \delta\tau_y^j \rangle
\end{array}\right| = \left|\begin{array}{cc|cc}
1e^{-6} & 0 & 0 & 0 \\
0 & 1e^{-6} & 0 & 0 \\
\hline
0 & 0 & 1e^{-6} & 0 \\
0 & 0 & 0 & 1e^{-6}
\end{array}\right| \qquad \text{eq: 3.18}
$$

where $\delta\tau_x^i$ is the zonal wind stress error associated to i-th grid point and the values of the diagonal element are expressed in N^2m^{-4}. Then the first guess of the background error covariance matrix is calculated from eq 3.17. Finally R Q and $B^f_{first\_guess}$ are used as inputs in the doubling algorithm, which solves the equation 3.5, in order to find the time asymptotic limit of the error background covariance matrix of the forecast B^f.

As first assessment of the PKFS skills a comparison among the simulation, filtered, smoother and forecast estimates with the assimilated data is presented. In particular the filtered solution is obtained assimilating 100 SSH data once a day while the forecast is the solution of the numerical model between two daily assimilation cycles. The forecast starts from a filtered initial condition and ends before the insertion of the new observations, in our case the next day . Figure 3-19 shows the root mean square error respect to the observations as a function of time for all the numerical experiments. The small oscillations of each curve are caused by the measurement noise at each data insertion time.

It has to be underlined that filter and smoother solutions are not independent from the data against which we are comparing, while the simulation and the forecast are. In particular the forecast, as already mentioned above, is independent because it is the model output during the filter run just before the insertion of that particular observation

As it is expected from the theory, the simulation has the biggest error of about 7 mm. The forecast shows a lower error which, after very few assimilation cycles, starts to oscillates around 4 mm, corresponding to an improvement of 40%. The filter and the smoother solutions show the lowest error, less 3 mm, and the skill of two runs is comparable, with 55% of the simulation error corrected. Except for the very beginning the smoother is better than the filter and the best solution is achieved in about 15 days. This time could be interpreted as the time it takes to the control variables in the smoother procedure to modify the filter solution. Even if the set up of the model is not realistic and then the 15 days value can be not accurate, it is plausible to have some delay in smoother performance compared to the filter run. In the filter method the information is forcedly inserted into the oceanic system, while with the smoother it is the modified wind stress that corrects the filter solution.

The fact that the smoothed solution is better than the filtered one is in agreement with the theory. The smoother run in fact uses also formally future observations and then it should be capable to acquire more information. Nevertheless this is not trivial because the smoother, in this implementation, does not use directly the observations but their information is hidden in the increment computed from the filtered analysis. In practice the smoother does not assimilate directly the sea surface height but it finds the wind stress necessary to obtain the measured sea surface height. So the smoother is just a simulation forced by the so called smoothed wind stress.

The cyan curve in Figure 3-19 is called data update and it is the mean amplitude of the SSH corrections. It is calculated as the root mean square difference between the filtered and the forecast solution. This quantity gives a rough idea of the impact of the insertion of measurements into the model. The fact that the data update (cyan curve) is always less than the filter root mean square error (green curve) implies that the major improvement is due to the capability of the model to acquire the information and to propagate it in time. On the other hand if the data update were bigger than the analysis it would meant that the information acquired by the model would be immediately lost.

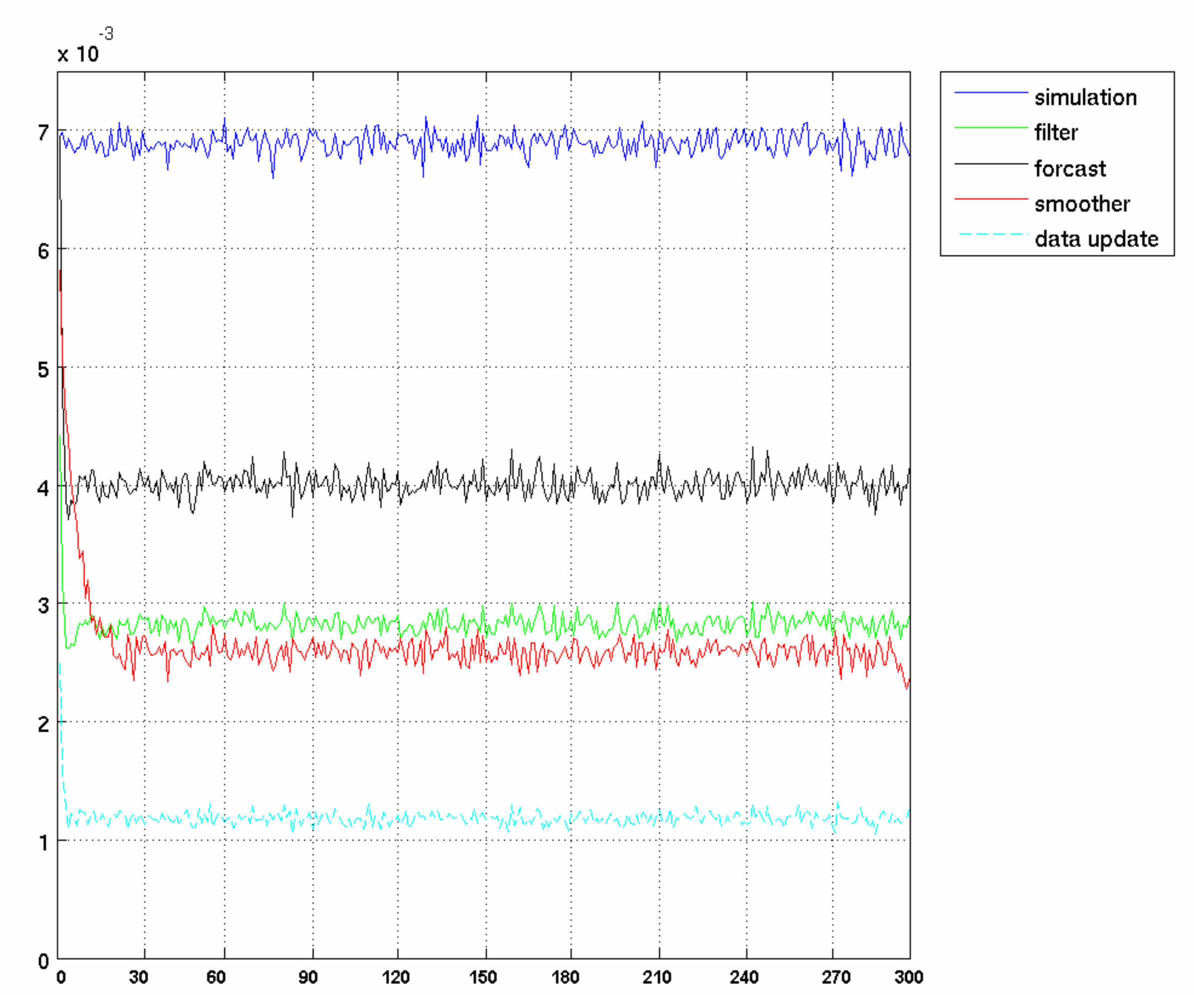

Figure 3-19:Time series (in days) for the basin mean Sea Surface Height root mean square erros [m] for the simulation (perturbed experiment), filter (assimilation of data in the past), smoother (assimilation of data both in the past and future), forecast (solution before the insertion of the observations starting from a filter initial condition), data update (basin mean aplitude of the SSH corrections). The model error matrix is chosen to beas in eq: 3.18

In order to better assess the PKFS performance we should use independent data. In our case the independent data are the current velocities from the true run. Figure 3-20 represents the basin mean root mean square error computed by the difference of filter, smoother and simulation with the true run: the analyzed estimates are better than the simulation for sea surface height and the meridional velocity, while the filtered zonal velocity is worse . This is due to the fact that the smoother algorithm cannot find a good ‘smoothed’ wind stress for the zonal velocity component. This problem will be solved by choosing a different initial background error covariance matrix as explained further below.

In order to evaluate in which part of the basin the errors are bigger the root mean square error as function of space is calculated. Sea surface height, zonal and meridional velocity are represented in Figure 3-21, Figure 3-22, Figure 3-23 respectively. For all the analyzed fields the error is organized in longitudinal bands with the highest value in the southern area. Further investigation has demonstrated that the error developed in that area are dependent from the specification of error covariance matrix of the control variable.

We decided then to perform a second assimilation experiment where we have used the information that the error is associated only to the control variable τ_y, the meridional wind stress. In particular, the error covariance matrix of the control variable Q, is then defined as:

$$Q = \left|\begin{array}{cc|cc}
\langle \delta\tau_x^i \delta\tau_x^i \rangle & \langle \delta\tau_x^j \delta\tau_x^i \rangle & \langle \delta\tau_x^i \delta\tau_y^i \rangle & \langle \delta\tau_x^j \delta\tau_y^i \rangle \\
\langle \delta\tau_x^j \delta\tau_x^i \rangle & \langle \delta\tau_x^j \delta\tau_x^j \rangle & \langle \delta\tau_x^j \delta\tau_y^i \rangle & \langle \delta\tau_x^j \delta\tau_y^j \rangle \\
\hline
\langle \delta\tau_y^i \delta\tau_x^i \rangle & \langle \delta\tau_y^j \delta\tau_x^i \rangle & \langle \delta\tau_y^i \delta\tau_y^i \rangle & \langle \delta\tau_y^j \delta\tau_y^i \rangle \\
\langle \delta\tau_y^j \delta\tau_x^i \rangle & \langle \delta\tau_y^j \delta\tau_x^j \rangle & \langle \delta\tau_y^j \delta\tau_y^i \rangle & \langle \delta\tau_y^j \delta\tau_y^j \rangle
\end{array}\right| = \left|\begin{array}{cc|cc}
0 & 0 & 0 & 0 \\
0 & 0 & 0 & 0 \\
\hline
0 & 0 & 1e-6 & 0 \\
0 & 0 & 0 & 1e-6
\end{array}\right| \qquad \text{eq: 3.19}$$

The results are shown in Figure 3-24,Figure 3-25,Figure 3-26, Figure 3-27. In this experiment all the basin mean analyzed fields are better then the simulation ones, moreover the error decreases everywhere in the basin.

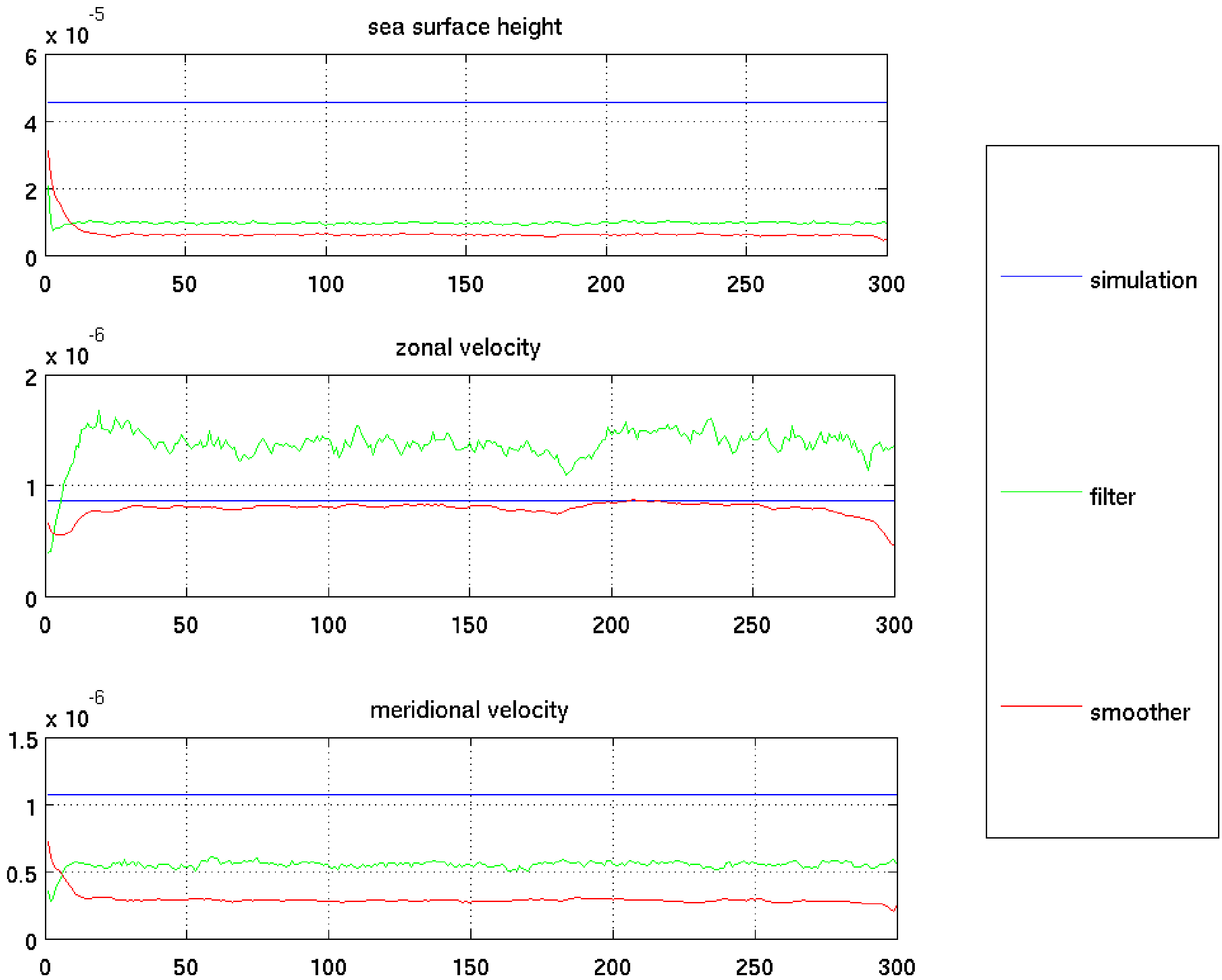

Figure 3-20: Time series basin mean root mean square error for the Sea Surface Height (m), zonal velocity (ms-1), and meridional velocity (ms-1) as a function of time (days) .The model error matrix is chosen to be as in (3.18)

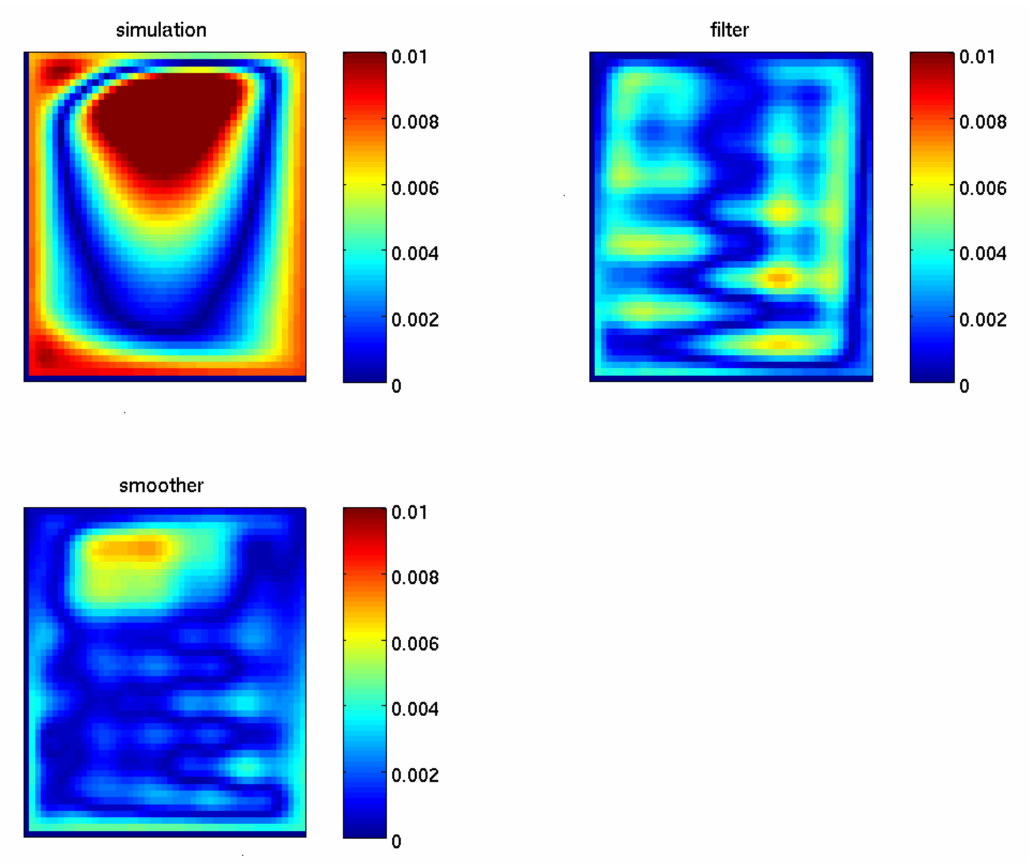

Figure 3-21: Spatially varying root mean square error of the Sea Surface Height (m). The model error matrix is chosen to be as in (3.18)

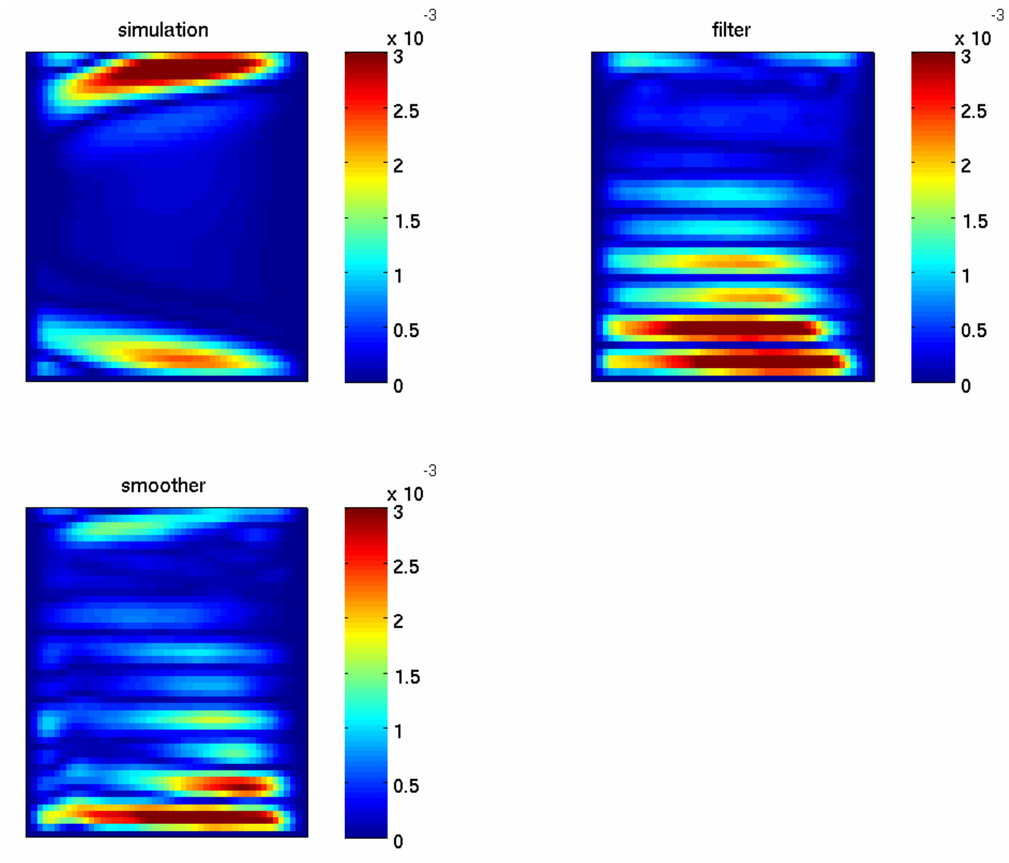

Figure 3-22: Spatially varying root mean square error of the Zonal Velocity (ms^{-1}) The model error matrix is chosen to be as in (3.18)

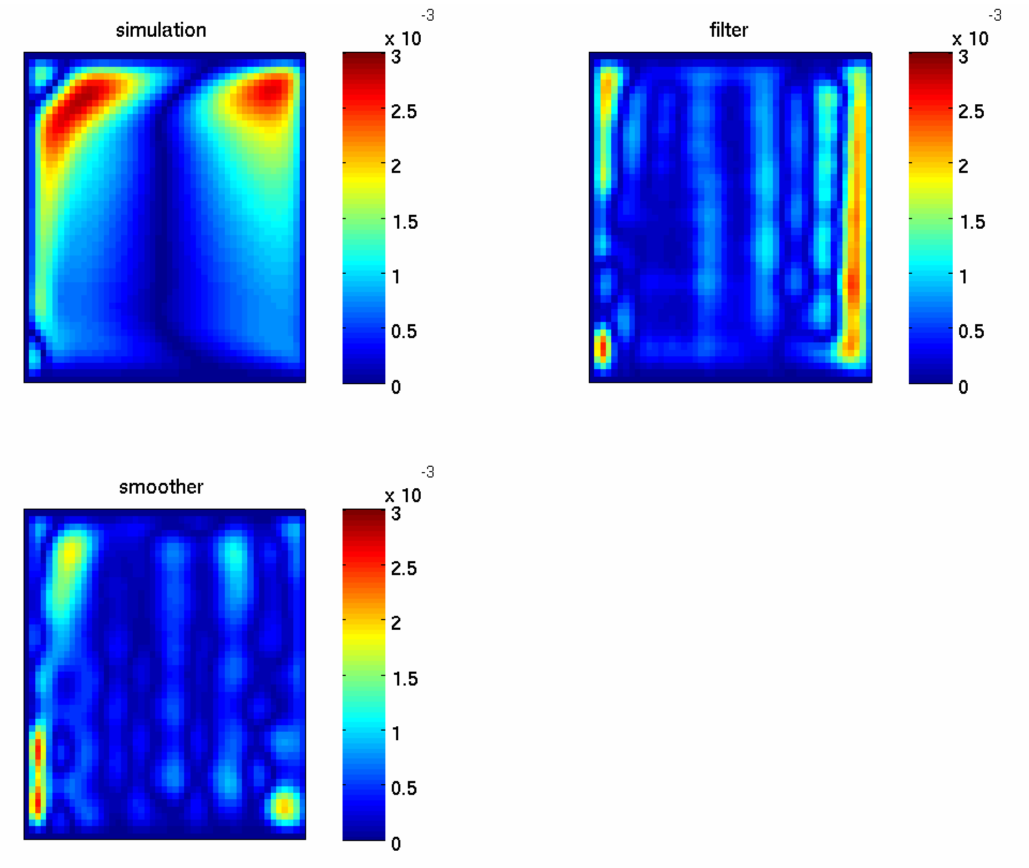

Figure 3-23: Spatially varying root mean square error of the Meridional Velocity (ms^{-1}) The model error matrix is chosen to be as in (3.18)

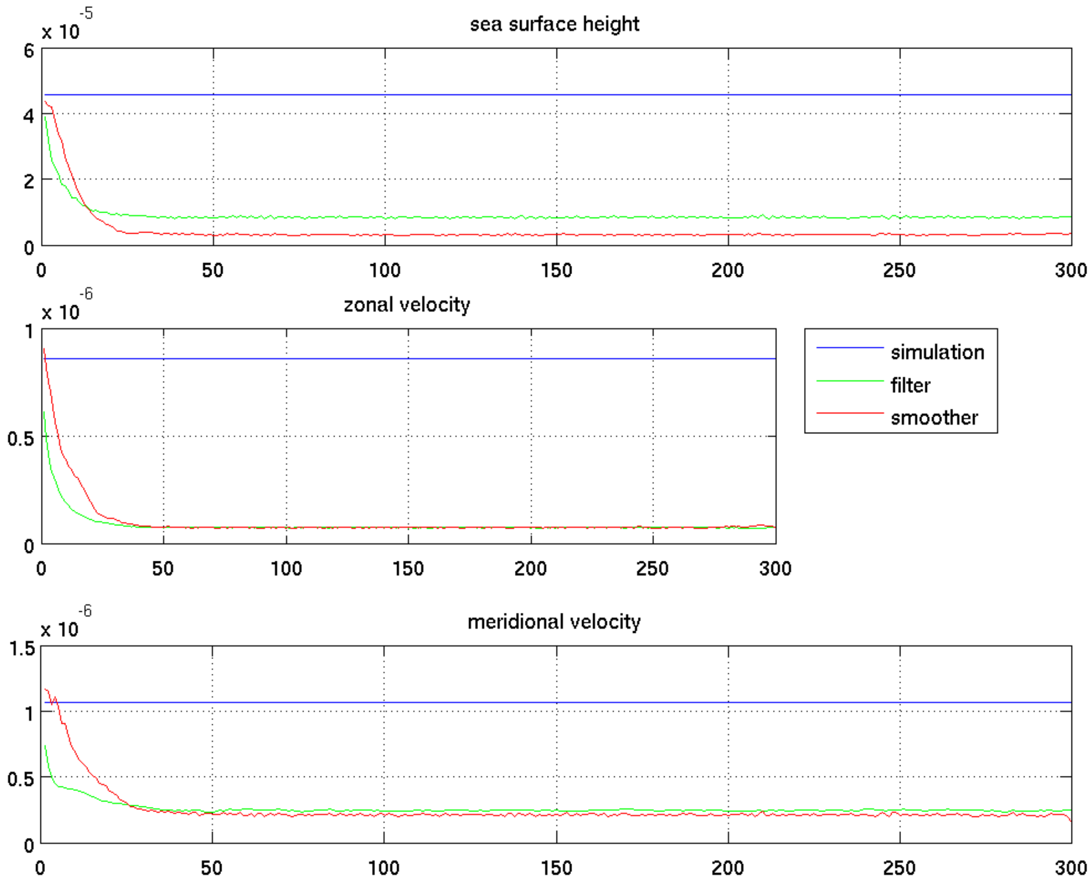

Figure 3-24 Time series basin mean root mean square error of the Sea Surface Height (m),Zonal Velocity (ms-1), Meridional Velocity (ms-1) as a function of time (days). The model error matrix is chosen to be as in (3.19)

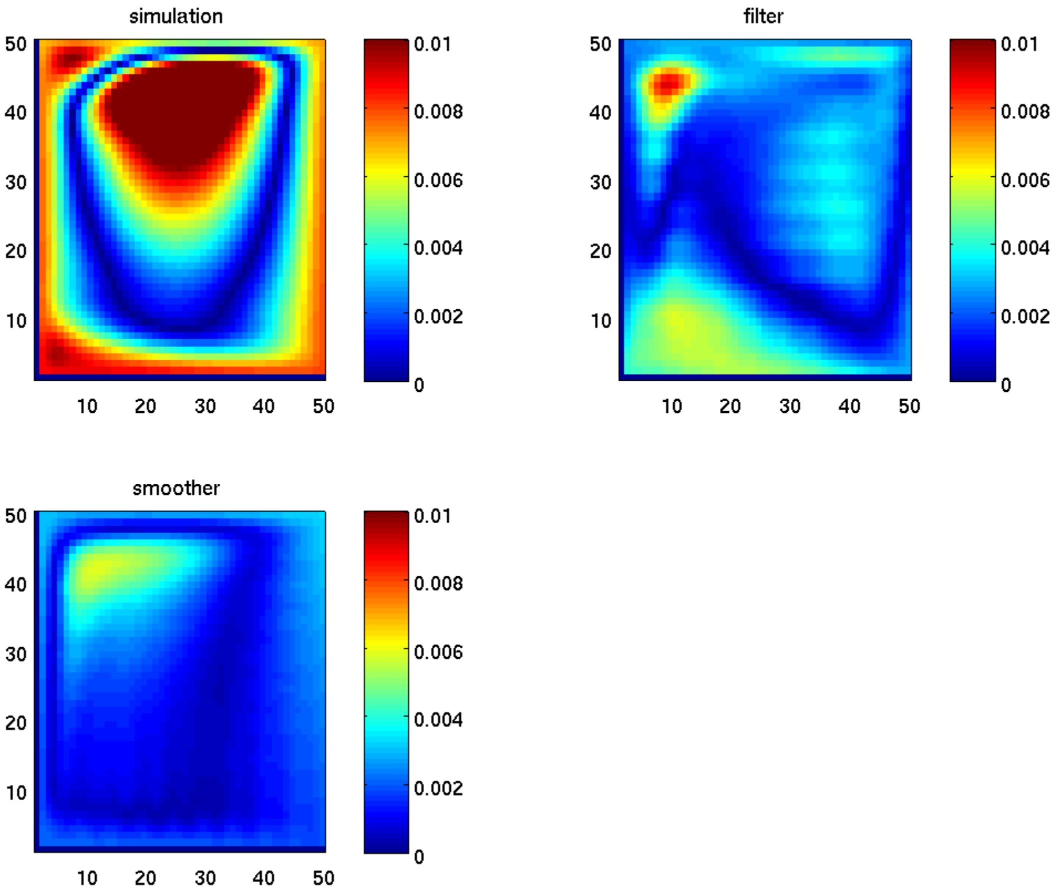

Figure 3-25 Spatially varying root mean square error of the Sea Surface Height (m) The model error matrix is chosen to be as in (3.19)

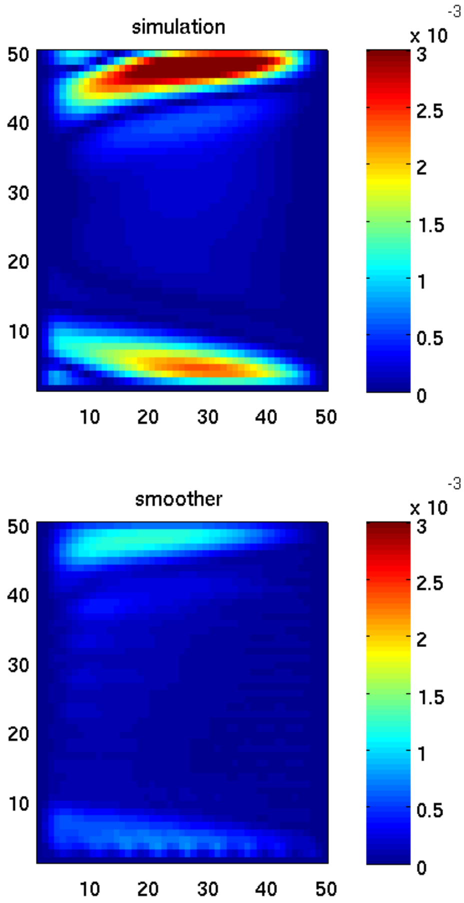

Figure 3-26: Spatially varying root mean square error of the Zonal Velocity (ms^{-1}) The model error matrix is chosen to be as in (3.19)

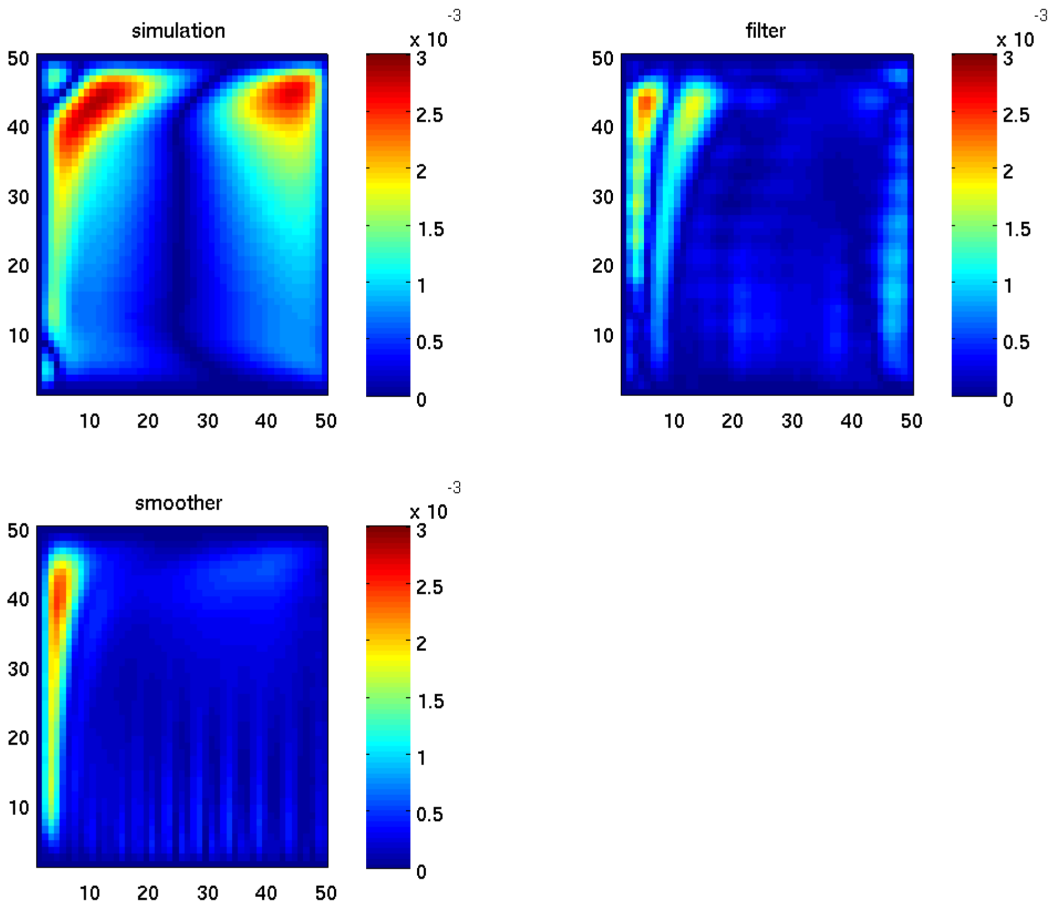

Figure 3-27: Spatially varying root mean square error of the Meridional Velocity (ms-1) The model error matrix is chosen to be as in (3.19)

Since the smoother changes the wind stress, it is interesting to compare the wind tress error in the smoother and the simulation. In Figure 3-28 illustrates the root mean square error of the wind stress for the smoothed solution of the experiment with the error associated also to the meridional component. Comparing it with Figure 3-17 it is evident that the error of the smoothed wind stress decreased everywhere respect to the simulation one.

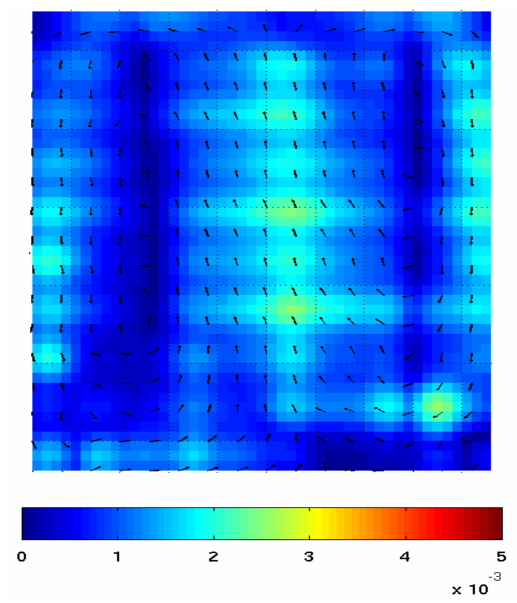

Figure 3-28: Root mean square error of the smoothed wind stress (Nm^{-2}) The model error matrix is chosen to be as in (3.18)

3.4.2 Time Dependent case

This experiment is conceptually identical to the previous one but in this case the wind stress in the 'true' and perturbed experiments is time dependent: the wind stress changes every day. The wind stress for the true experiment has been constructed using an algorithm which generates random numbers. For each coarse grid point two time series of random numbers has been produced: one for the zonal component and one for the meridional component of the wind stress. The using objective analysis technique, the "coarse grid" wind stress has been interpolated on the dynamical model grid. The perturbed wind stress used to force the simulation experiment has been computed adding to the "true" wind stress a space-time independent perturbation which has been at first generated on the coarse grid. Then, using the same objective analysis technique, it has been interpolated on the fine dynamical model grid and added up to the "true" wind stress.

The "true run" is 728 days long. The first half of this period is considered as spin up and only the last 364 days are used for the assimilation experiment. In this case the solution obviously does not reach a steady state value and the pseudo-observations are sampled every day at each assimilation grid point as in the steady state case. However this time the time variability of the observations is greater than in the previous case due to the fact that the true solution is time dependent.

The measurement covariance matrix is the same as before, that is, R is diagonal with values of 1e-6m^2 for the sea level errors. The error covariance of the control variable, Q, is now computed as a full matrix: let's define the matrix $\boldsymbol{\delta\tau}$ as

$$\boldsymbol{\delta\tau} = \begin{vmatrix} \tau_x^{i,j} - \bar{\tau}_x & \cdots & \tau_x^{i,t} - \bar{\tau}_x \\ \vdots & \ddots & \vdots \\ \tau_x^{n,j} - \bar{\tau}_x & \cdots & \tau_x^{n,t} - \bar{\tau}_x \\ \tau_y^{i,j} - \bar{\tau}_y & \cdots & \tau_y^{i,t} - \bar{\tau}_y \\ \vdots & \ddots & \\ \tau_y^{n,t} - \bar{\tau}_y & \cdots & \tau_y^{n,t} - \bar{\tau}_y \end{vmatrix}$$

where i=[1...n] is the number of grid points, j=[1...t] is the number of realizations and $\bar{\tau}_x^i$ and $\bar{\tau}_y^i$ are the time mean zonal and meridional wind stress respectively, then the control variable error covariance matrix is $Q = \left\langle \boldsymbol{\delta\tau\delta\tau}^{\mathbf{T}} \right\rangle$. Computing the error covariance in this way we assume that the biggest error is in the regions of greater variability which is a plausible hypothesis.

As in the steady state case the first assessment of the analyzed field is made comparing the basin mean root mean square difference between the pseudo-observations and the different estimates given by the filter and smoother algorithms. The results are shown in Figure 3-29.: once again the simulation error is the biggest one compared to the analyzed fields and to the forecast one. The filter solution is the better one showing the lowest error. The performance of the smoother solution is comparable with the filter but the mean error is higher. The smoother again improves the solution with respect to the filter with a delay, This behavior confirms the hypothesis that the smoother needs some time to improve the filter solution since the corrections are imposed through the atmospheric forcing and not directly to the ocean system as in the filter. The overall improvement of the smoother, filter and forecast solutions is more then 50% with respect to the simulation, meaning that the basin mean error for the smoother, filter and forecast is, on average, half of the simulation one. Moreover the data update rms values are small compared to the error of smoother and filter, suggesting that the filter and smoother improvements retain the information from the pseudo-observations

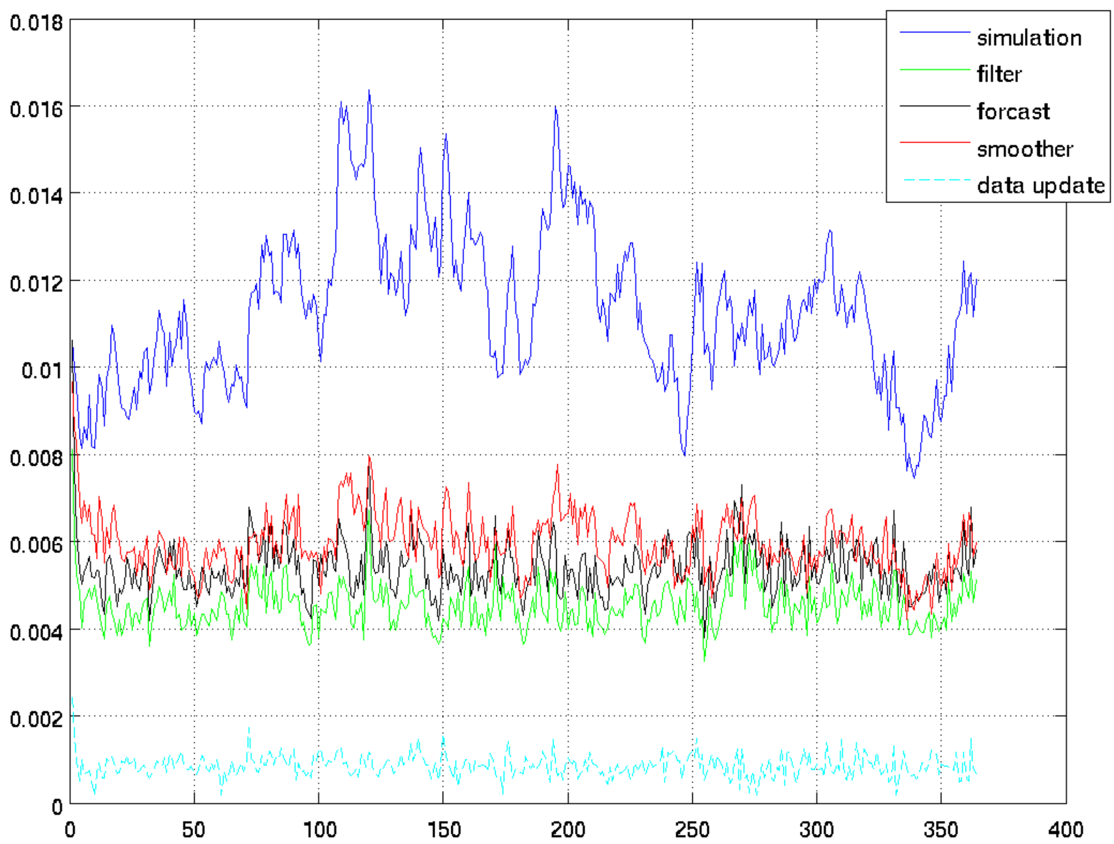

Figure 3-29: Time series basin mean root mean square error for the Sea Surface Height (m) calculated as the difference between the different estimates and the 'true solution' at the pseudo-obcervational points. The simulation is the perturbed run, the smoother and filter are the assimilated estimates, forecast (solution before the insertion of the observations starting from a filter initial condition), data update (basin mean amplitude of the SSH corrections).

Further assessment can be done using directly the "truth" so that the assessment of the data assimilation impact can be done on the non-assimilated variables, such as the meridional and zonal velocity fields. Figure 3-30 shows the basin mean root mean square error for the sea surface height, for the zonal velocity (second panel) and for the meridional velocity. (third panel). The major improvement, as expected, is on the assimilated SSH: in fact the sea surface height error decreases more then the 70% but also the zonal and meridional velocity errors decrease of about 50%.

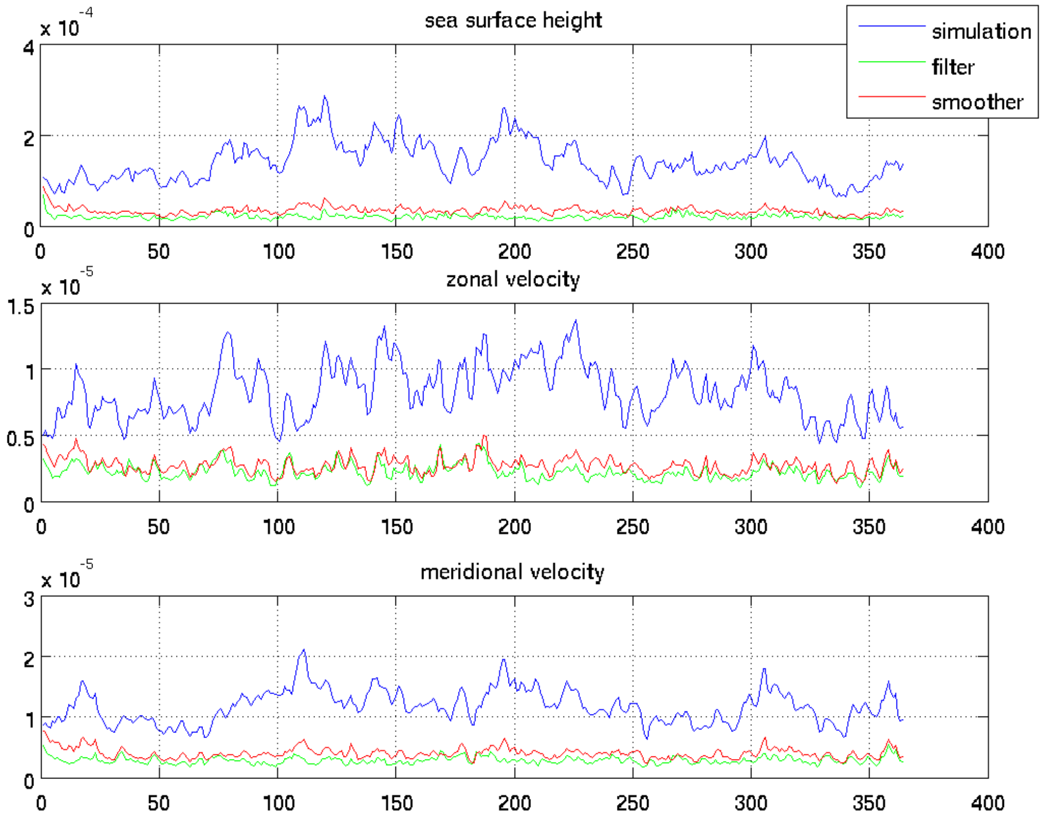

Figure 3-30: Time series basin mean root mean square error of the Sea Surface Height (m),Zonal Velocity (ms^{-1}), and Meridional Velocity (ms^{-1})

The Figure 3-31,Figure 3-32,Figure 3-33 show the root mean square error respectively for sea surface height, zonal and meridional velocity, computed as a difference with truth and as a function of space. The spatial structure of the error shows a decrease in every part of the basin for all the variables.

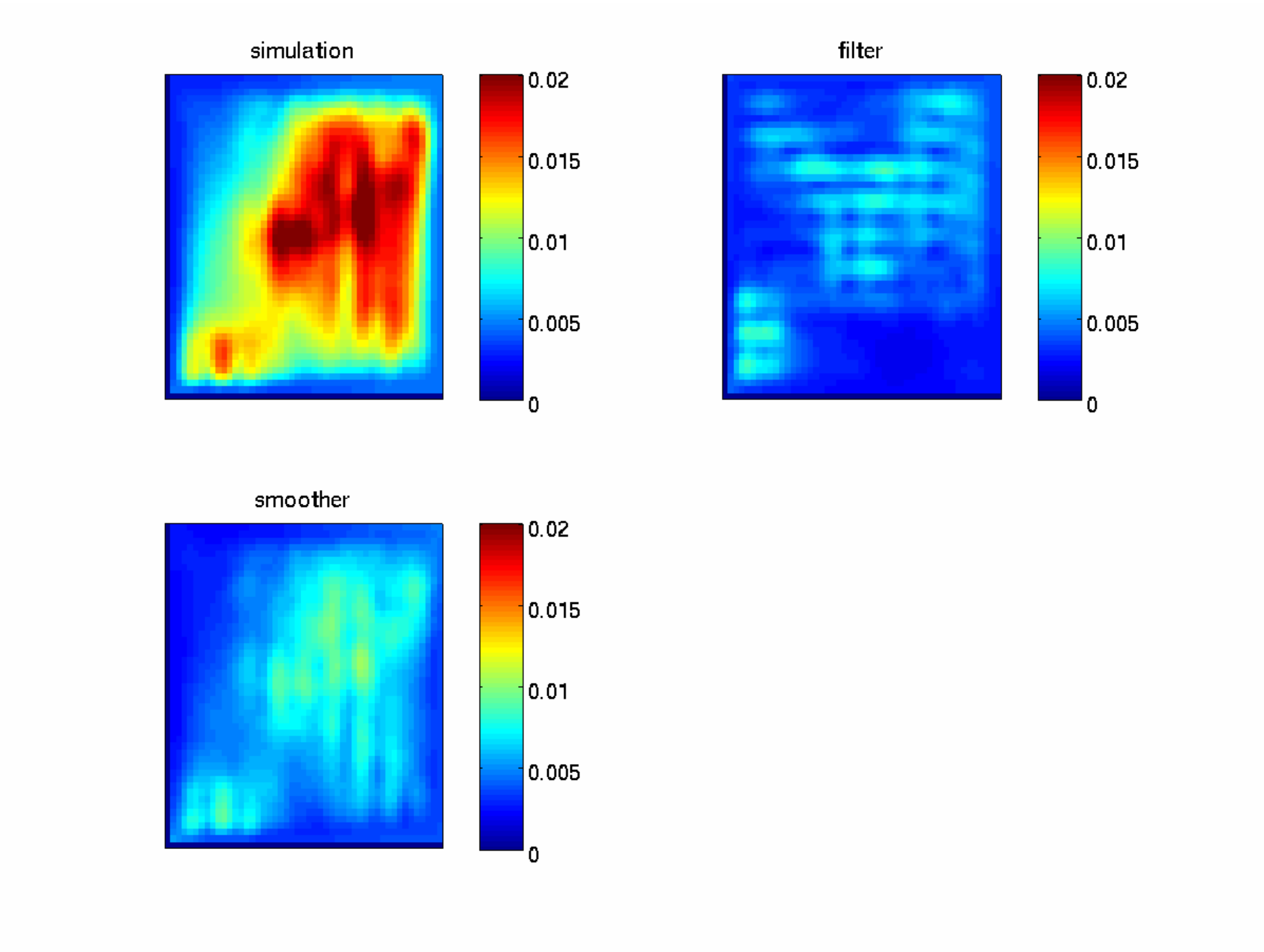

Figure 3-31: Spatially varying root mean square error of the Sea Surface Height (m) averaged over 364 days

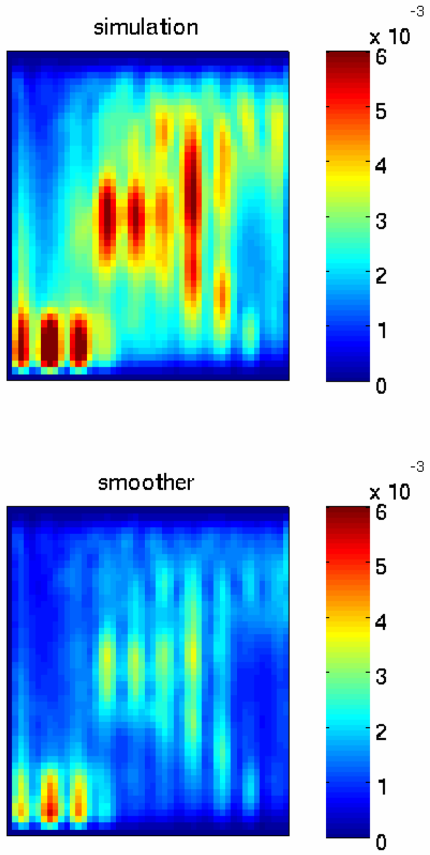

Figure 3-32: Root mean square error of the Zonal Velocity (ms^{-1}) averaged over 364 days

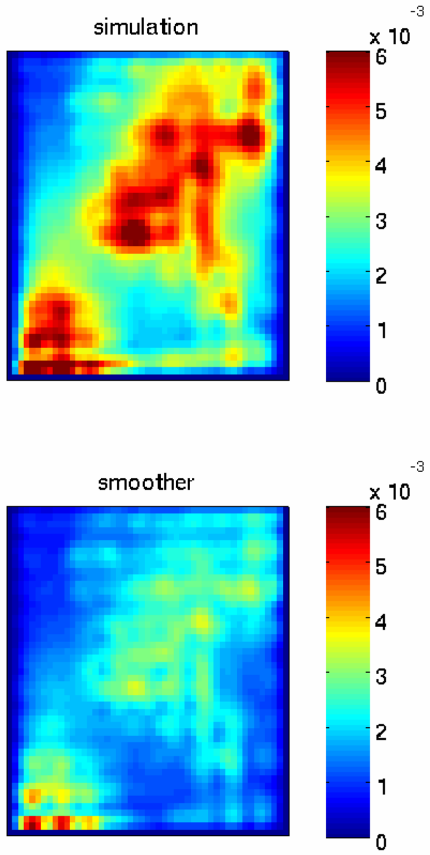

Figure 3-33: Spatially varying root mean square error of the Meridional Velocity (ms^{-1}) averaged over 364 days.

We want now to assess in a different way the quality of the PKFS solutions. The previous case is not precise enough in principle, even if practically and most of the times, is the only way. Comparing with observations which are much less than the degrees of freedom of the problem cannot in fact demonstrate the uniqueness of the optimal solution found. In this condition there exist an infinite number of estimated fields which can reduce the starting error of an arbitrary amount.

We will use here the consistency checks that we explained in section 3.2. The left column of the Figure 3-34 shows the theoretical error variance assigned to the simulation, to the forecast, and to the filter estimate computed using equation 3.4. The right column shows their correspondent values computed using the simulation, filter and smoother solutions. The patterns and values are very similar for all the pictures and this is a clear indication of consistency between the theoretical value of the error associated with the different solutions and the real one, obtained from the estimates. The filter and forecast errors are smaller than the simulation ones, as expected and found before already.

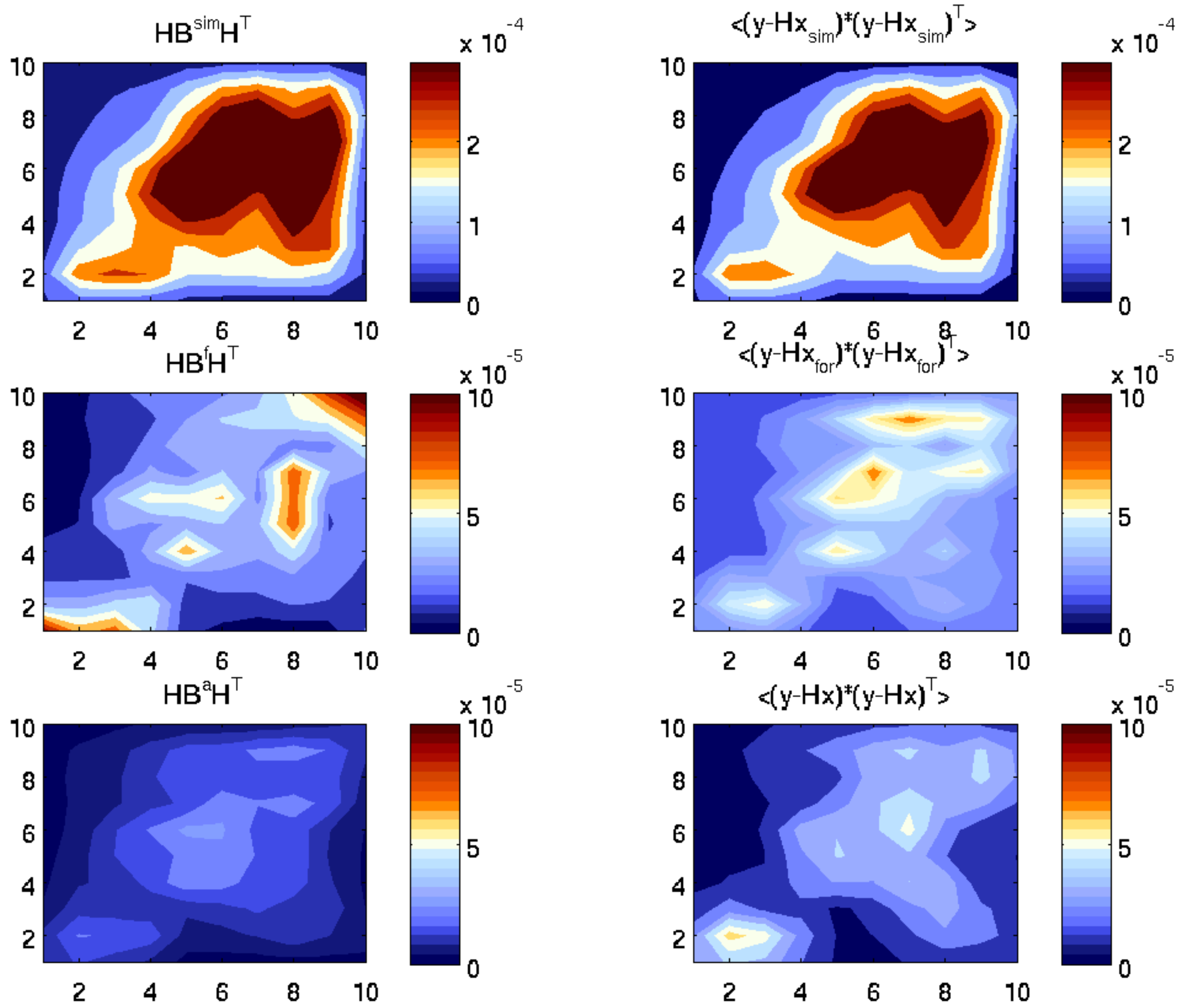

Figure 3-34 Left column and from top to bottom: Theoretical values of the error for the simulation, forecast and filter and for SSH. Right column in the same order: correspondent quantities calculated from the different estimates. The values are expressed in meters.

Finally the last consistency assessment is done visualizing the left and the right hand side of the equation 3.14. The top left image of Figure 3-36 shows the difference between the simulation and the forecast errors while on the top right panel their theoretical values are shown. The bottom right panel shows the difference between the forecast and the filter estimate errors and on the right their theoretical value. The top panels tell us that the model has a good skill in keeping the correction information done at initial time of the forecast. The lowest panels indicate that the impact of assimilating measurements is actually larger in reality of what it would be expected from the theory. The similarities between the left column images and the right ones is an important indication of the consistency of the solutions.

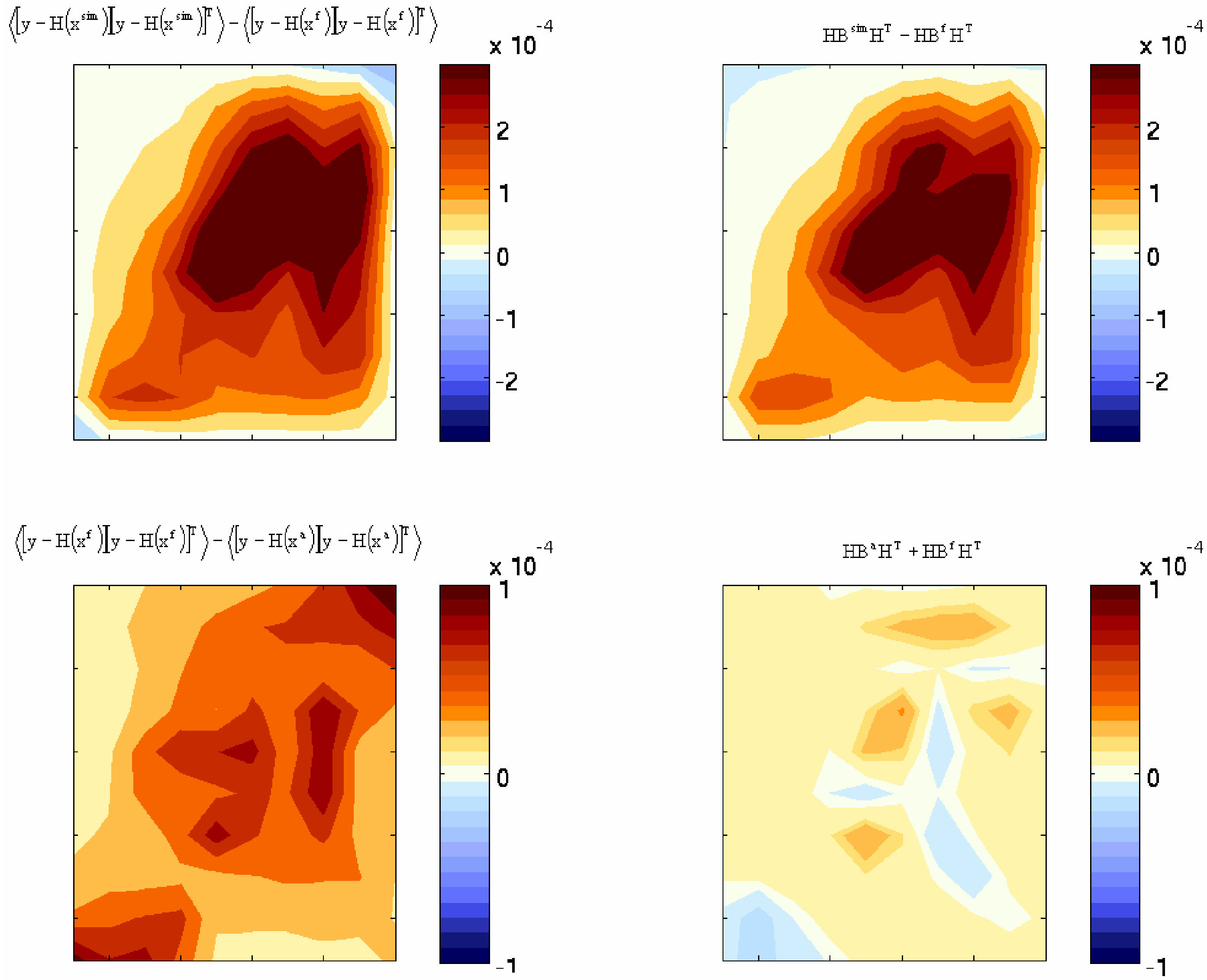

Figure 3-35: Difference of model-observation residuals (m): upper panels model simulation minus analysis (right) and its expected value (left). Bottom panels forecast minus analysis (right) and its expected value.

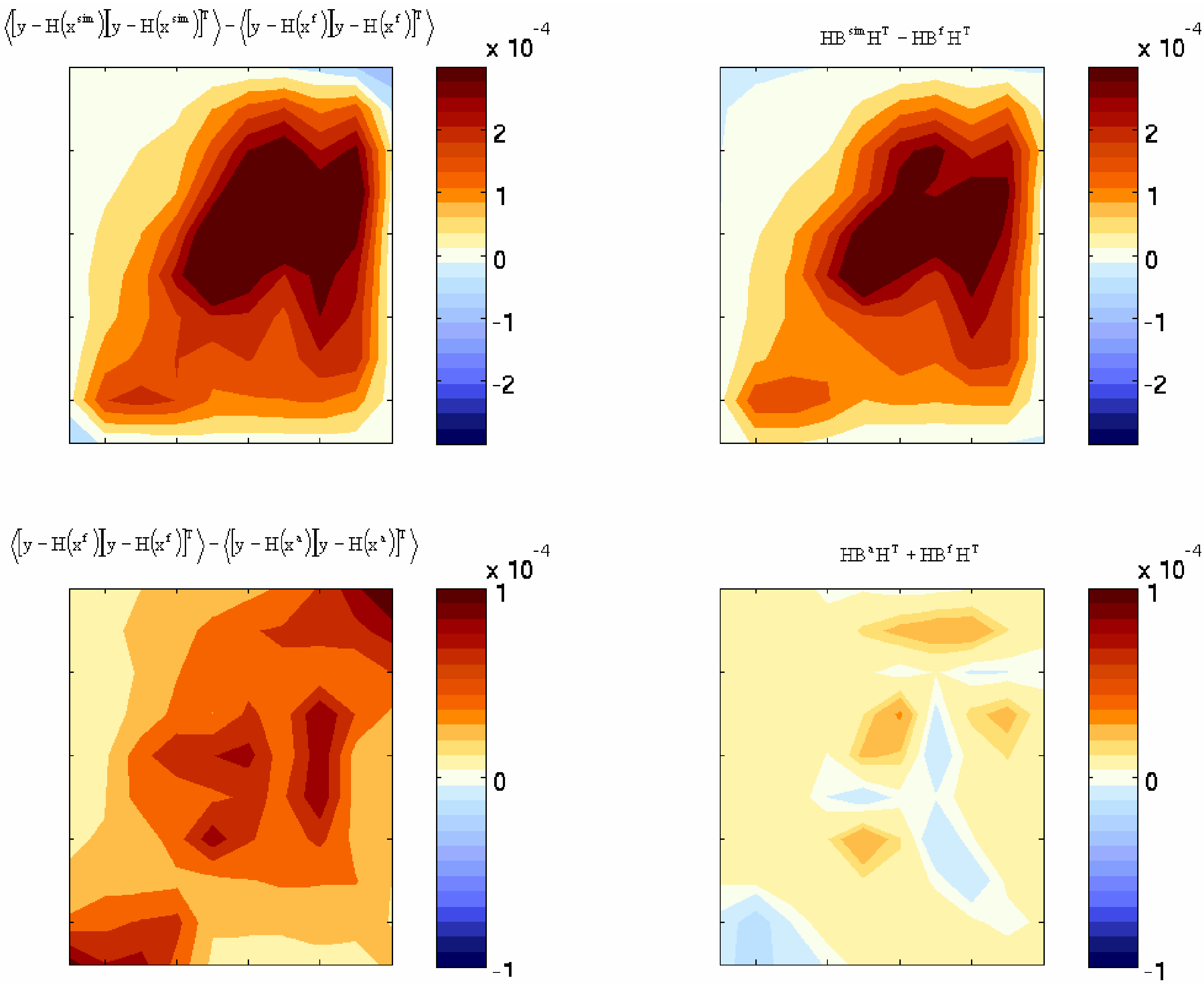

Figure 3-36: Difference of model-observation residuals (m): upper panels model simulation minus analysis (right) and its expected value (left). Bottom panels forecast minus analysis (right) and its expected value.

4. Chapter: Re-analysis of the Mediterranean Sea circulation: intercomparison between optimal interpolation and 3dvar techniques

In this chapter we present two reanalysis experiments of the Mediterranean Sea done with different assimilation schemes. The general circulation model configuration for both experiments is the same and it has been described in chapter 2. The assimilation scheme used are a Reduced Order Optimal Interpolation (ROOI) and 3Dvar. The ROOI is applied using the SOFA code developed by De Mey and Benkiran (2002) and it will be described in section 4.1. The 3Dvar code has been developed by Dobriĉiĉ and Pinardi (2008) and it will be described in section 4.2.

From a mathematical point of view the OI and the 3Dvar are methods to minimize the variance of the error taking into account measurement and model errors and their respective covariances. In other words these two methods minimize a cost function which can be written as:

$$\Im(\mathrm{x}) = \frac{1}{2}\left[(\mathrm{x}-\mathrm{x}_b)^T \mathrm{B}^{-1}(\mathrm{x}-\mathrm{x}_b) + (H(\mathrm{x})-\mathrm{y})^T \mathrm{R}^{-1}(H(\mathrm{x})-\mathrm{y})\right] \quad \text{eq.1}$$

where B is the error background covariance matrix, R is the observational error covariance matrix, H is the non linear observational operator, y is the vector of the measurements, x_b is the background state vector and x is the analyzed state vector. The two main differences between the OI and the 3Dvar are:

- The OI finds a local minimum identified by the observations within a prescribed influential radius while the 3Dvar finds a global minimum.
- The OI uses the analytical solution of the gradient of the cost function equal to zero while the 3Dvar finds the gradient numerically. It minimizes the gradient using a numerical

recursive algorithm whose iteration are stopped when the value of the cost function gradient is small with respect to its initial value.

The minimum of the cost function used in OI is the same as used in the Kalman Filter but in OI the error background matrix is fixed and the error propagation equations are not considered. The error covariance matrix is specified a priori both in OI and 3Dvar.

4.1 Reduced Order Optimal Interpolation

SOFA is the acronym for System for Ocean Forecast and Analysis (De Mey and Benkiram, 2002) and it is a multivariate reduced order optimal interpolation scheme. Optimal interpolation is one of the possible methods to find a solution of a least square problem and it is based on Kalman filter algorithm. Hereafter few basic concepts will be revisited.

An observation y_o is formally linked to the true state x_t by the stochastic equation: $y_o = H(x_t) + \varepsilon$ where *H* is the non linear observation operator, and ε is the observational noise which is assumed to be unbiased and with covariance R. The full nonlinear model *M* is used to predict the state vector x at time t+δt, that is $x^b_{t+\delta t} = M_{t,t+\delta t}(x_t)$ where x is the analyzed valued at time step t. The update step for the time t+δt is given by $x = x_b + K(y_o - H(x_b))$ where K is the Kalman gain matrix which can be written as $K = BH^T(HBH^T + R)^{-1}$ where B is the background error covariance matrix and H is the linearized form of *H.*

Optimal interpolation is a particular case of the Kalman filter where the error background covariance matrix B can be written in a simplified form as

$$B = D^{\frac{1}{2}} C D^{\frac{1}{2}} \qquad \text{eq: 4.1}$$

where D is a diagonal matrix of the error variances which can be predicted with an external scheme from the previous analysis error variances, and C is a correlation matrix which is assumed to be constant in time. Since optimal interpolation does not evolve dynamically the errors, the modeling and the parameterization of B contain most of the physics of the estimation problem. SOFA is termed “multivariate” because the state vector considers several model variables at the same time if not all as in our case (Dobricic et al., 2005). The order reduction is obtained projecting the state vector onto Empirical Orthogonal Functions (EOFs). In order to explained better this concept it is useful to write the spectral factorization of the error background covariance matrix:

$$B = V^{T}\Sigma V \qquad \text{eq: 4.2}$$

where V is the orthogonal matrix whose column are the eigenvectors of the error covariance matrix and Σ is the diagonal matrix whose diagonal elements are the eigenvalues. In order to have the same degrees of freedom of the equation 4.1 it is possible to assume time dependent eigenvalues and stationary eigenvectors. Writing the error background covariance matrix as in equation 4.2 has two main advantages:

- EOFs or eigenvectors define spatially coherent, multivariate modes of variability which are more meaningful than correlation (Von Storch and Navarra, 1999)
- The spectrum of the eigenvalues is usually red; henceforth it allows to reduce the number of eigenvector used.

Once the reduction is done, two subsets of vectors are obtained: the one which generates the reduced state space and the one which generates the null space. If the errors between the two spaces are weakly correlated trough the dynamical processes, the attempt to control the null space is explicitly discharged. A process is described by the null space if it projects on the vector basis which generates such space. If a state variable is partly projected onto the null space, that part will not be corrected by assimilation. Mathematically it is possible to write $V=S|\underline{S}$ where the S is the reduced space, $\underline{S}$ the null space and the vertical bar (|) indicates the column-wise juxtaposition of both matrices. Now it is possible to write the error background covariance matrix as:

$$B \cong S^{T}BrS \qquad \text{eq. 4.3}$$

where Br is the covariance matrix in the reduced space. We note that this matrix is singular because of the order reduction.

Actually in SOFA uses also a form of 'filter partitioning' like the one discussed for the Kalman filter of chapter 3 It subdivides the horizontal and vertical parts of the error covariance matrix and uses EOFs for the vertical part. This approach was first explored by De Mey and Robinson (1987) and it is justified because in the ocean the vertical coordinate has a low vertical mode dimension. SOFA then writes in S the vertical EOFs and leaves the horizontal part in the Br.

It is possible then to think that at each horizontal grid point i $\in$ [1..h] of the model a background error covariance matrix $\tilde{B}(i,i')$ is specified whose relationship with the full error background covariance matrix is $B = \begin{vmatrix} \cdots & \cdots & \cdots \\ \cdots & \tilde{B}(i,i') & \cdots \\ \cdots & \cdots & \cdots \end{vmatrix}$. The horizontal background error covariance matrix is $Br = \begin{vmatrix} \cdots & \cdots & \cdots \\ \cdots & \tilde{B}r(i,i) & \cdots \\ \cdots & \cdots & \cdots \end{vmatrix}$ and the vertical part is $S = \begin{vmatrix} \tilde{S}(1) & 0 & \cdots & \cdots \\ 0 & \tilde{S}(i) & \cdots & \cdots \\ \cdots & \cdots & \cdots & 0 \\ \cdots & \cdots & 0 & \tilde{S}(h) \end{vmatrix}$ from which $\tilde{B}(i,i') = \tilde{S}^T(i)Br\tilde{S}(i)$. For each model grid point we could then have a different set of vertical error covariance EOFs $\tilde{S}$. We now model the horizontal part as:

$$Br(i,i') = \Lambda(i,i')^{\frac{1}{2}} C(i,i') \Lambda(i,i')^{\frac{1}{2}} \qquad \text{eq: 4.4}$$

In equation 4.4 Λ is the diagonal matrix containing the singular values and C contains the horizontal covariances associated to each EOF.

In this particular implementation of SOFA for the Mediterranean Sea, the horizontal covariances of the modes are modeled as Gaussian functions of distance with an influence radius of 60 km. The EOFs are calculated from an historical model simulation for a period 1993-1997 (Demirov et al., 2002). They are calculated for the 13 geographical regions (Figure 4-3) and for 4 seasons; 20 EOFs are kept for each region and season. (Dobriĉiĉ et al., 2005). The EOFs are quadrivariate containing surface elevation η, barotropic stream function ψ, temperature T and salinity S resulting in a state vector of this form:

$$x = \begin{vmatrix} \eta \\ \psi \\ T \\ S \end{vmatrix} \qquad \text{eq: 4.5}$$

The relationships among the variables can be described using the statistical tools but sometimes the covariance among the variables calculated only from the statistics may results in corrections which are physically inconsistent. Hence it is useful to constrain the relationship among the errors in the state variables to satisfy some physical relationships. At the zero order in the perturbation expansion in the Rossby number, it is possible to find the geostrophic balance (Pedlosky, 1987), so it is possible to assume that also the error EOFs should satisfy this relationship (e.g. Daley 1991) as well as the physical fields do. The geostrophic balance of the EOFs can be calculated from the formula of Pinardi et al. (1995):

$$\delta\eta = \frac{f\delta\psi}{gh} - \frac{1}{\rho_o h}\int_{-h}^{0}\left(\frac{\partial\rho}{\partial T}\delta T + \frac{\partial\rho}{\partial S}\delta S\right)(z+h)dz \qquad \text{eq: 4.6}$$

where $\delta\eta$ is the anomaly sea surface height, g is the gravity acceleration, f is the Coriolis parameter, $\delta\Psi$ is the anomaly barotropic stream function, δT the temperature and δS the salinity anomalies, ρ_o is the reference density typically 1024 gm^{-3} and h is the bottom supposed to be at the constant depth of 1000m. The usage of this relationship has the advantage to impose geostrophic constraints on the corrections for $\delta\eta$ knowing the δT and δS values. However we need to note that the assumption of flat bottom at 1000 meters will force us to assimilate observations only where the topography is at least 1000 meters deep.

The OI produces an estimate from observations on the T,S, psi and eta model state variables but not directly on velocities. Thus we have chosen to change 'a posteriori' the barotropic velocity field using the barotropic stream function corrections and a relationship based on the geostrophic balance:

$$\delta u_b = \frac{1}{h}\frac{\partial(\delta\psi)}{\partial y}$$
$$\delta v_b = \frac{1}{h}\frac{\partial(\delta\psi)}{\partial x} \qquad \text{eq: 4.7}$$

where u_b and v_b are the barotropic velocities which can be calculated from the total model velocities (u,v) each analysis time as:

$$u_b = \frac{1}{h}\int_{-h}^{0} u\,dz$$
$$v_b = \frac{1}{h}\int_{-h}^{0} v\,dz \qquad \text{eq: 4.8}$$

The corrections on the barotropic component of the velocity can generate fast barotropic gravity waves which can cause numerical instabilities on the model. In order to reduce the impact of the propagation of that waves a "divergence damping filter" is used (Talangrand, 1972). The assimilation cycle is one day long using the FGAT method (First Guess at Appropriate Time) as described in Dobriĉiĉ et al. (2007). This method consists in calculating the misfits, difference between the observation and the model, at the correct time while the corrections are inserted at once at the end of each day.

4.2 3Dvar

The 3Dvar is the acronym for three-dimensional variational method which iteratively finds the minimum of the cost function written below:

$$\Im(x) = \frac{1}{2}\left[(x - x_b)^T B^{-1}(x - x_b) + (H(x) - y)^T R^{-1}(H(x) - y)\right] \qquad \text{eq: 4.9}$$

The nomenclature of the previous section is maintained. It is defined three-dimensional because it finds the global minimum in the 3 spatial dimensions without considering the time dimension. The general form of equation 4.8 contains the non linear operator *H* which has to be linearized around the background state ($H = \frac{dH}{dx}$) in order to create a quadratic cost function with a single global minimum. Defining the misfits as $d = [y - H(x_b)]$ and the increment as $\delta x = x - x_b$ it is possible to rearrange equation 4.8 as:

$$\Im(x) = \frac{1}{2}\delta x^T B^{-1}\delta x + \frac{1}{2}(H\delta x - d)^T R^{-1}(H\delta x - d) \qquad \text{eq: 4.10}$$

The inversion of the background error covariance matrix might be very expensive from computational point of view if B is very large as it actually is and it can be very inaccurate if B is close to be singular. In order to avoid the inversion of B it is possible to write

$$B=VV^T \qquad \text{eq. 4.11}$$

where V might be a non-squared matrix. Since the inverse of a not-squared matrix is defined by its pseudo-inverse V^* the inverse of B may be written as $B^{-1}=(V^T)^*(V)^*$

Using the above relationships the cost function can be written as

$$\Im(x) = \frac{1}{2}\delta x^T \left(V^T\right)^* V^* \delta x + \frac{1}{2}(H\delta x - d)^T R^{-1}(H\delta x - d).$$

If a least square problem is define as: $\delta x = Vv$ whose solution is $v = V^*\delta x$, then the cost function becomes $\Im(x) = \frac{1}{2}v^T v + \frac{1}{2}(HVv - d)^T R^{-1}(HVv - d)$

The 3Dvar used in this study is the one implemented by Dobriĉiĉ and Pinardi (2008) and it is multivariate scheme as well as the OI described in the previous section. The state vector is defined by $x = [T, S, \eta, U, V]^T$ where T, S, U, V are the three dimensional temperature salinity, zonal and meridional velocity fields respectively.

The V matrix is modelled as linear combination of operators which transforms the increment from the control space to the physical space (Dobriĉiĉ and Pinardi., 2008):

$$V = V_D V_{uv} V_\eta V_H V_V. \qquad (4.12)$$

where V_v transforms from the vertical reduced space defined by EOFs to the temperature and salinity profiles defined in the physical space, V_H applies the horizontal covariance modelled to be Gaussian, V_η is the operator which calculates the sea surface height correction from the temperature and salinity fields, V_{uv} calculates the correction for the velocity field based on the geostrophic balance, V_D applies the divergence dumping filter to the current velocity corrections.

The EOFs used to model V_v are the same ones described for the optimal interpolation scheme discussed in the previous section, the horizontal radius of influence for the Gaussian function has been chosen to be 60 Km as for the SOFA.

The 3Dvar schemes permit the modellization of quite complex linear observational operator as in the case of V_η. In the 3Dvar implementation of Dobriĉiĉ and Pinardi.(2008) a barotropic model is used to calculate the correction on the anomaly sea surface height, and barotropic velocity. The equations which govern the barotropic model are shown below.

$$\frac{\partial \bar{u}}{\partial t} - f\bar{v} = -gH\frac{\partial \eta}{\partial x} - \int_{-H}^{0}\left[\int_{-z}^{0}\frac{\partial(\delta b)}{\partial x}dz'\right]dz + \gamma\nabla^2\bar{u}$$

$$\frac{\partial \bar{v}}{\partial t} + f\bar{u} = -gH\frac{\partial \eta}{\partial y} - \int_{-H}^{0}\left[\int_{-z}^{0}\frac{\partial(\delta b)}{\partial y}dz'\right]dz + \gamma\nabla^2\bar{v}$$

$$\frac{\partial \eta}{\partial t} + \left(\frac{\partial \bar{u}}{\partial x} + \frac{\partial \bar{v}}{\partial y}\right) = 0$$

$\bar{u}$ and $\bar{v}$ are barotropic components of the velocity, f is the Coriolis parameter, g gravity acceleration, H bottom depth, η surface elevation, γ is the coefficient of horizontal viscosity, and $\delta b = g(\delta\rho/\rho_0)$ is the buoyancy anomaly. The density perturbations are calculated using the linearized form of the density equation: $\delta\rho = \alpha\delta T - \beta\delta S$ where α and β are expansion coefficients for temperature and salinity. In this model, as described by Dobriĉiĉ et al.(2008) the bottom friction and the non linear advection term are neglected.

The advantage of this formulation respect to a simple geostrophic balance described in the previous section is that the correction can be calculated also in areas where the topography is shallower than

1000 meters depth. Eventually the operator V_η calculates the corrections for the sea surface elevation, and the barotropic component of the velocity while V_{uv} produces the corrections for the baroclinic component of the velocity using the geostrophic relation.

In order to save computer time the iteration to find the minimum of the function are done with a multi-grid approach. That means at first the solution is found on a coarse grid, $1/4^{th}$ of degree in this particular implementation and then this solution is used as a first guess in order to find the solution on the fine resolution which is $1/16^{th}$ of degree in our case.

4.3 Observations

Both reanalysis will use a comprehensive observational in situ and satellite data set that includes:

- Satellite sea surface temperature data
- In situ temperature and salinity profiles
- Satellite sea level anomalies from altimetry

For sea surface temperature we use a time series of satellite maps interpolated on the model grid. The data are available from 1985 and they are obtained with an Optimal Interpolation scheme from the satellite data; provided from the satellite oceanographic group of CNR-ISAC (Marullo et al. 2007).

The in situ data set is built on the historical data archive of MedATLAS (Maillard et al. 2003) and it contains vertical profiles of temperature and salinity from bottles, thermometers, XBT, MBT, and CTD sensors. The spatial distribution of the pair of salinity and temperature measurements for a period 1985-2000, is shown in Figure 4-1 and the spatial distribution of temperature measurements only for the same period is presented in Figure 4-2

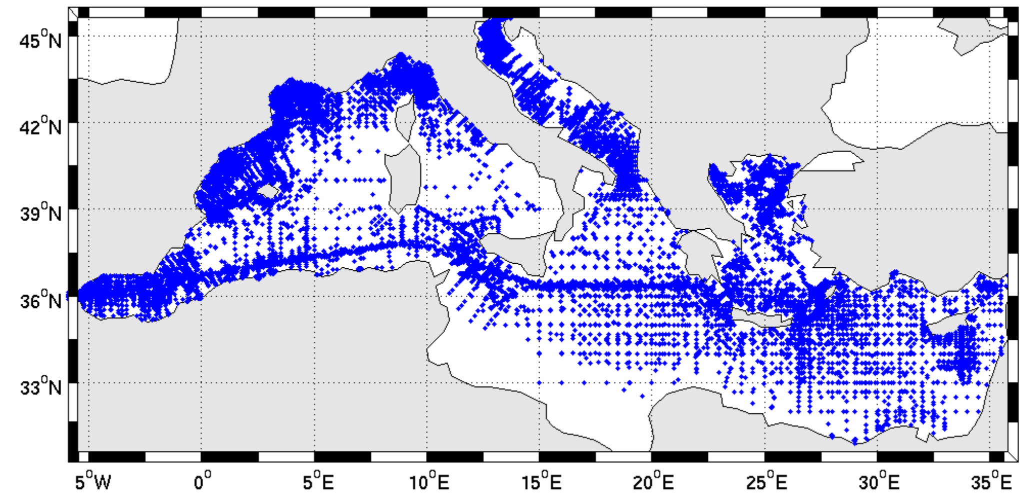

Figure 4-1: Spatial distribution of the pair measurements of temperature and salinity collected from bottle and CTD sensor from 1985 to 2000.

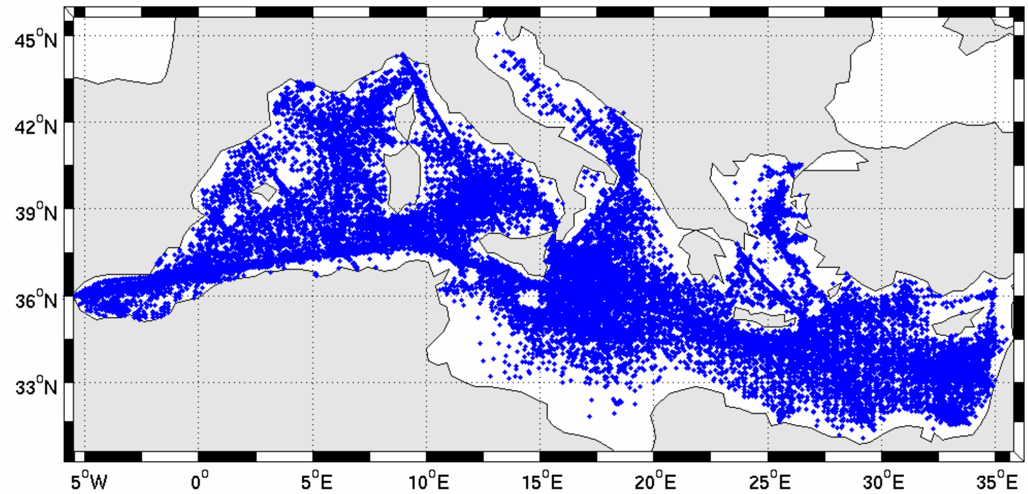

Figure 4-2 Spatial distribution of the temperature measurements collected from XBT, MBT, thermometer sensor from 1985 to 2000.

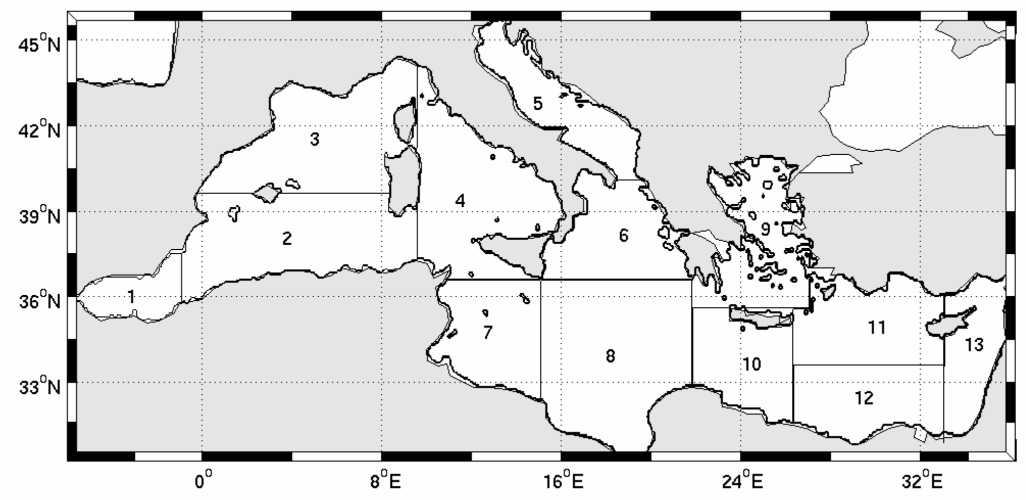

Figure 4-3: Regions of the Mediterranean Sea.

. The vertical profiles have been separated in thirteen geographical regions, shown in Figure 4-3, characterized by different dynamical regimes. Then the profiles are further divided by month and a visual quality check has been applied to each group of data. The quality check consists in calculating the mean vertical profile for temperature and salinity in each region from the monthly gridded climatology, provided by MedATLAS (Rixen et al, 2002). Then the comparison between the mean profiles with all the data belonging to each region and month is done.

Figure 4-4 shows an example of the visual check performed: on the left panel there are all the temperature profiles and on the right there are the salinity ones for region number 4 in June from 1985 to 2000. The red line is the mean profile computed from the grid-data while the black profiles are the original measurements. In case a data of a black profile differs significantly from the mean then it is considered an outliers and the entire profile is discharged. Figure 4-5 and Figure 4-6 represents the number of profiles as a function of region and year for the pair of salinity and temperature measurements and temperature only respectively after the quality check has been applied.

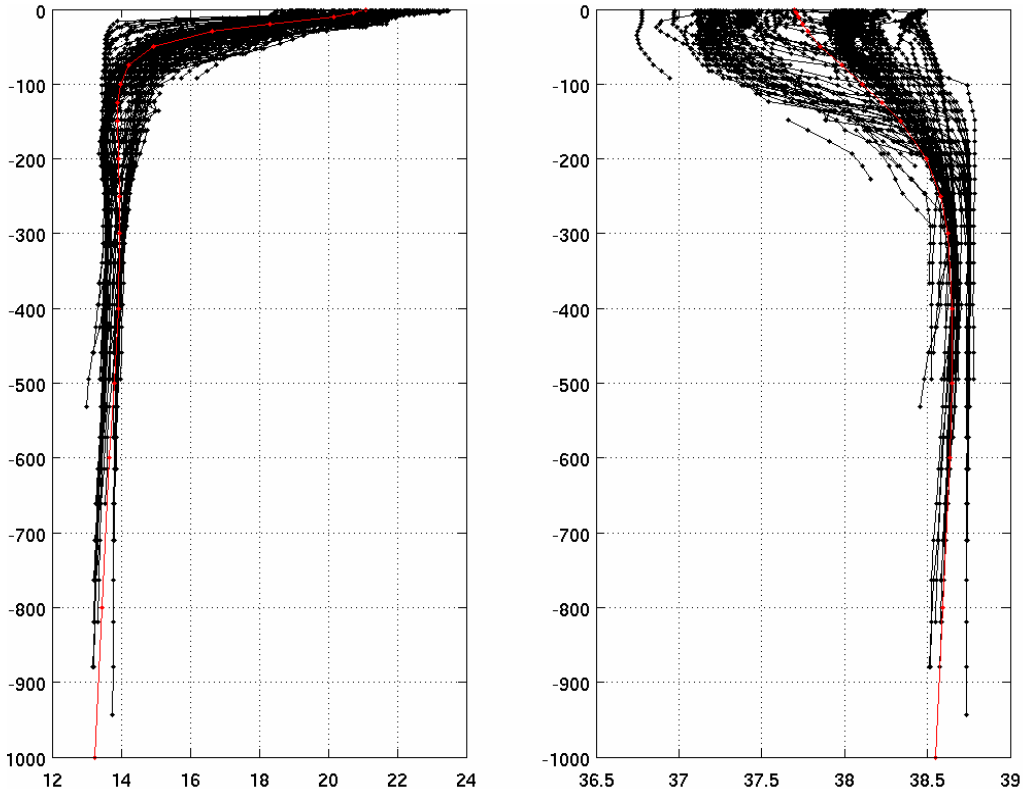

Figure 4-4: On the left panel there are the temperature profiles (black) and the mean one (red line) collected in the region number 4 from 1985 to 2000. On the right panel there are the salinity profiles (black) and the mean one (red line) for the same region and period.

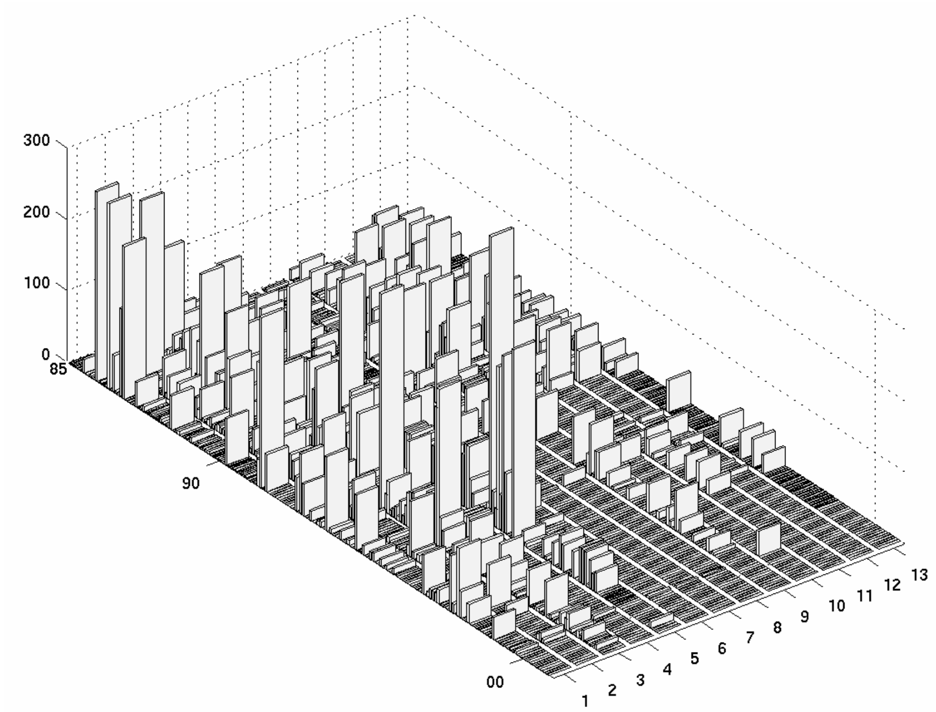

Figure 4-5: Number of pair of salinity and temperature measurements as function of regions and months.

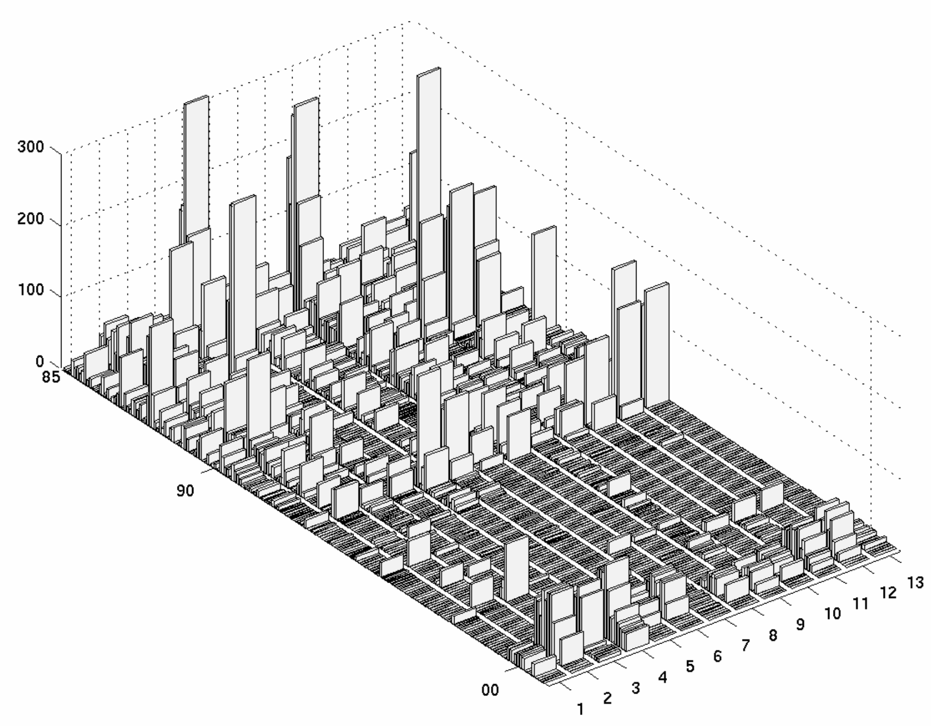

Figure 4-6: Number of and temperature measurements as function of regions and months

The satellite sea level anomaly measurements are taken from ERS1 ERS2, Envisat, Topex/Poseidon satellite missions. These data are the same used by Pujol et al.(2005). Pre-processing of this data set is described by Pujol et al (2005), i.e.:

- Intercalibration among the satellites using the Topex/Poseidon as reference orbit: “global crossover adjustment” (Le Traon and Ogor 1998).
- Geophysical corrections as inverse barometer, tide, tropospheric, ionospheric.
- Measurements noise reduction applying Lanczos and median Filters
- Long wavelength correction

The corrected data were re-sampled every 7 km using cubic spline.

Figure 4-7 shows the spatial distribution of SLA observation using all the satellite available and Figure 4-8 shows the number of SLA data for each day in the Mediterranean basin.

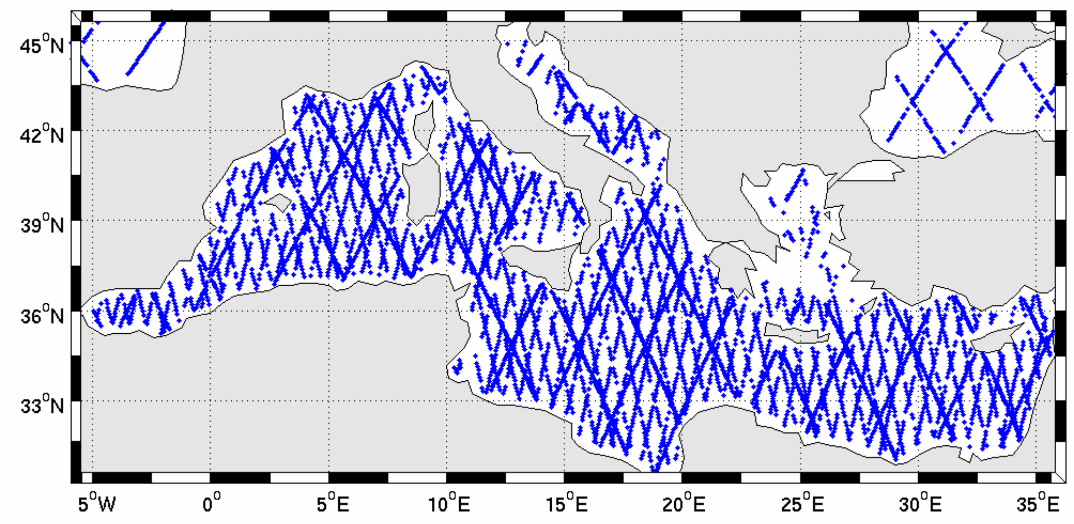

Figure 4-7 : Spatial resolution of SLA data for the four satellites considered, ERS-1, ERS-2, Topex-Poseidon and Envisat.

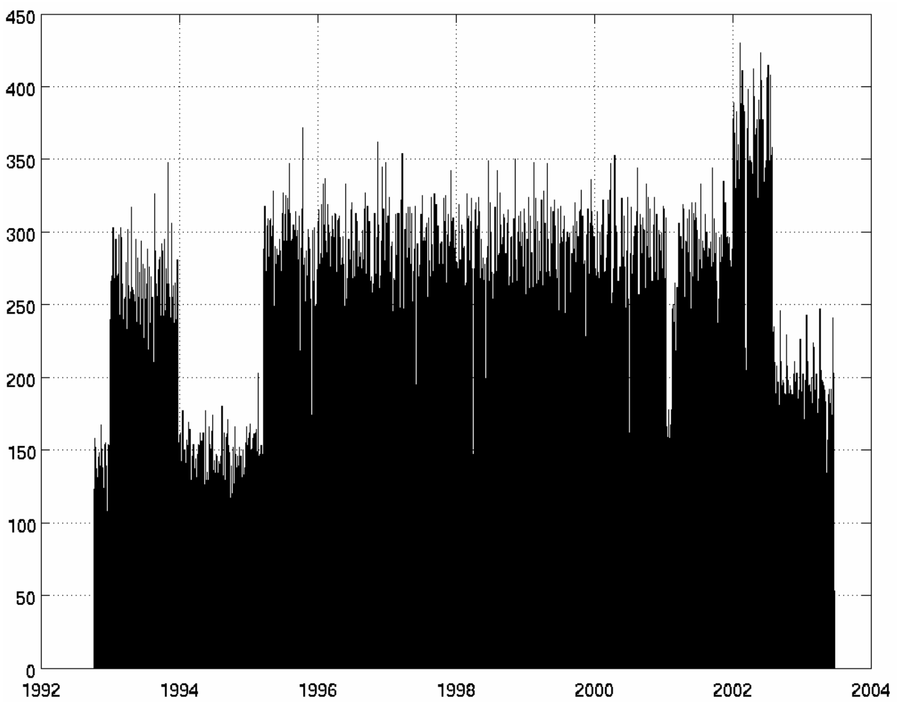

Figure 4-8: Number of observations per day in the Mediterranean Sea collected from all the available satellites.

The SLA is not a prognostic variable of the model but the Sea Surface Height (SSH) is; thus in order to calculate the SLA the Mean Dynamic Topography of Dobriĉiĉ et al.(2005) is subtracted from Sea Surface Height.

4.4 Results

This section presents a generic assessment of the 3Dvar and SOFA reanalysis and a comparison between the two solutions.

Figure 4-9 shows the volume salinity integral in the Mediterranean basin as function of time: the green line is computed from the MedATLAS monthly mean climatology, the blue line from the SOFA and the black line from the 3Dvar estimates. A positive drift in the estimates is evident and it is more accentuated in the SOFA ($8*10^{-3}$ psu/yy) then in the 3Dvar ($5*10^{-3}$ psu/yy).

At the contrary the surface integral of the salinity doesn't show any drift, as shown in Figure 4-10. The two solutions are in agreement with each other and they are consistent with climatological values. From 1987 to 1991 the surface salinity annual mean value presents a tendency to decrease and then it increases again starting from 1990. The last three years it remains constant settling to slightly higher values respect to the climatology. For all the period the salinity has a seasonal cycle whose amplitude is comparable with the climatological one. In order to investigate the increase of salt in the whole water column Figure 4-11 and Figure 4-12 present the salinity anomalies (with respect to climatology) horizontal integral as function of depth and time for the SOFA and 3Dvar estimates respectively. Both estimates show the same trend: the salinity starts to increase in the upper part of the water column then it spread to intermediate and bottom depths where it is trapped. Even though the salinity increases in the upper part of the water column seems to be correct for this period of time, as shown later, the increase of salt at depths may an effect of compensation for the cold temperature drift of the model (to be shown later). It is worth to notice that 3Dvar reaches only half of the SOFA anomaly values at intermediate and bottom depths.

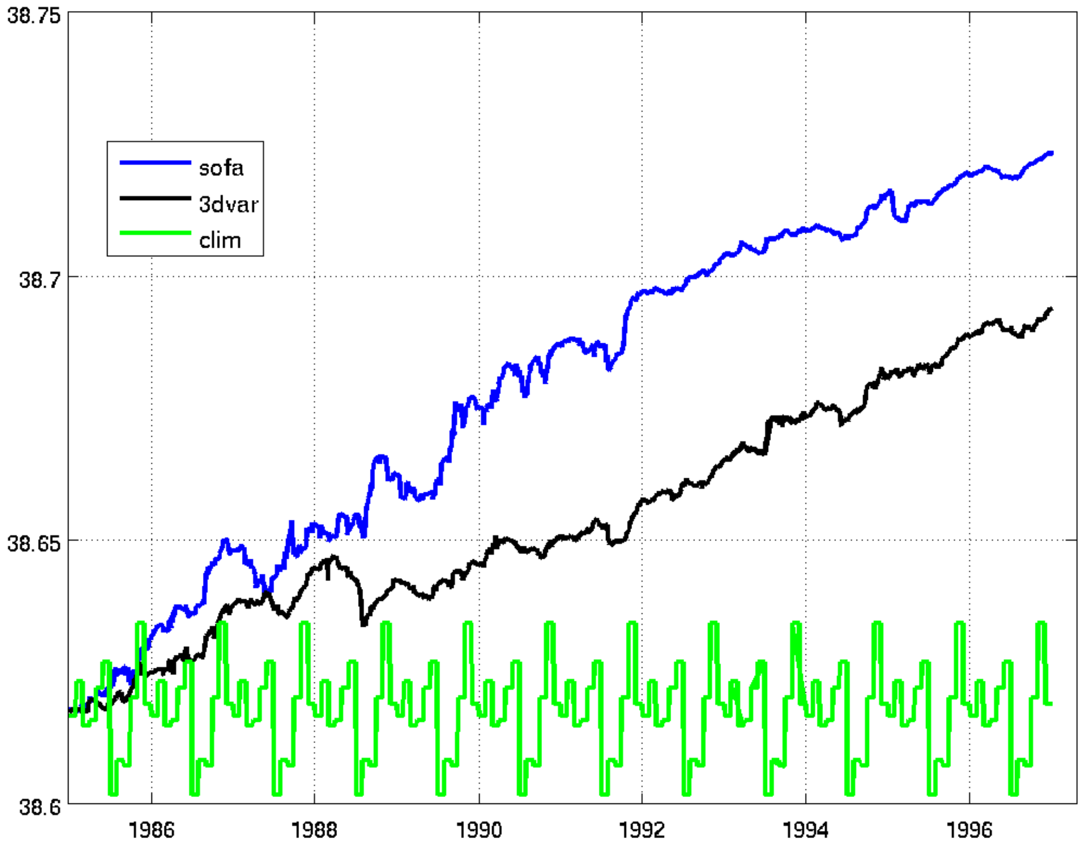

Figure 4-9: Salinity volume integral (psu). Blue line is the SOFA solutions, Black line is the 3Dvar solution and the green line is the monthly mean climatology.

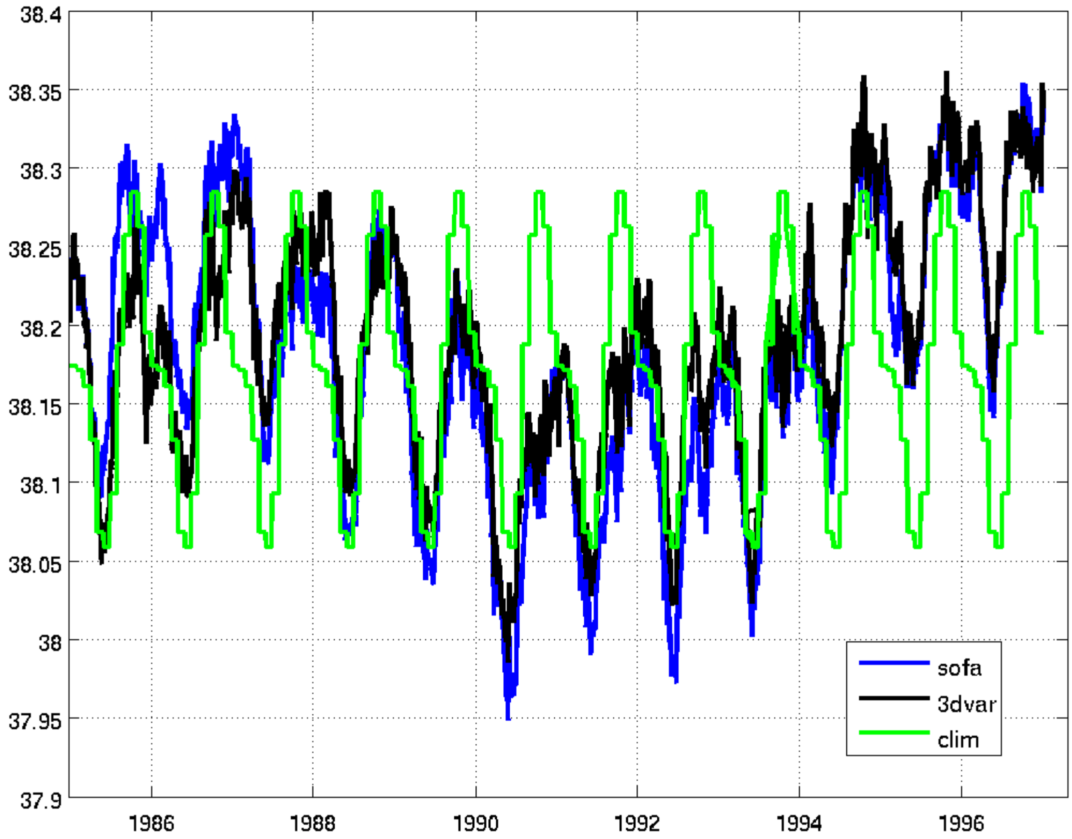

Figure 4-10: Surface salinity integral (psu). Blue line is the SOFA solutions, Black line is the 3Dvar solution and the green line is the monthly mean climatology.

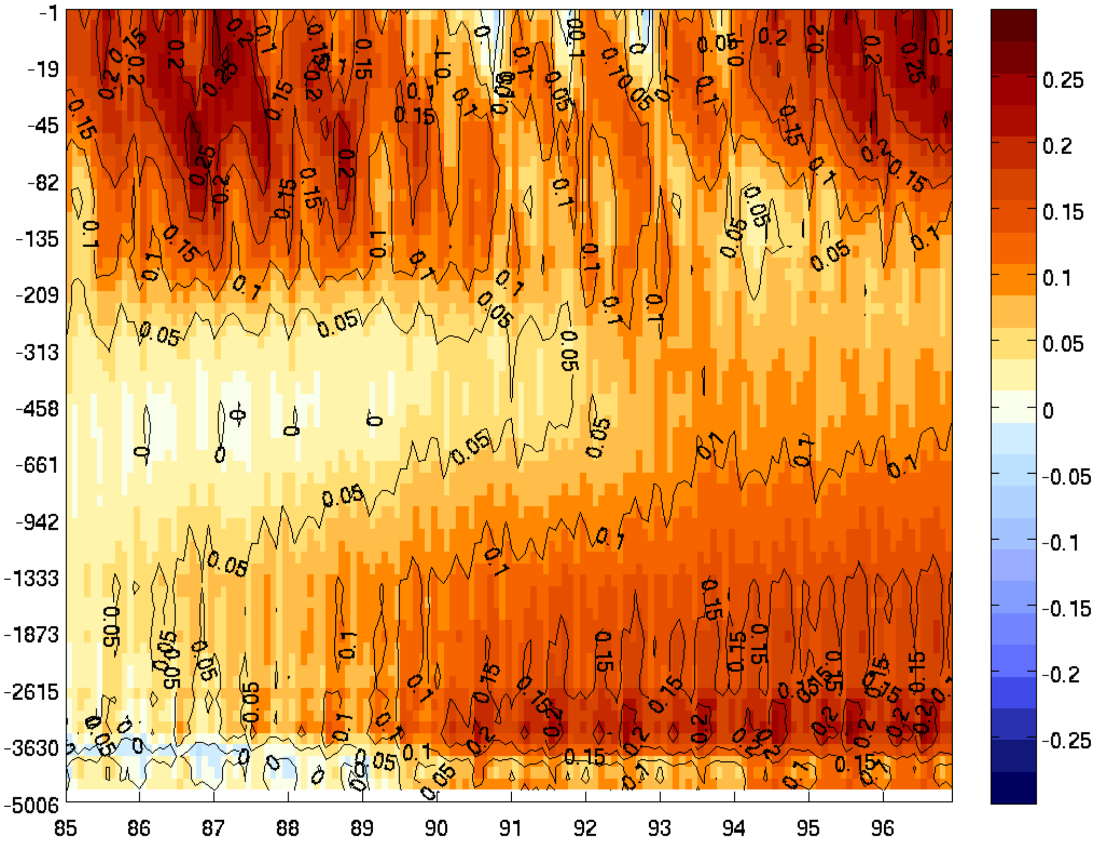

Figure 4-11 Salinity integral anomaly (psu) as function of depth and time calculated as model minus climatology for the SOFA experiment.

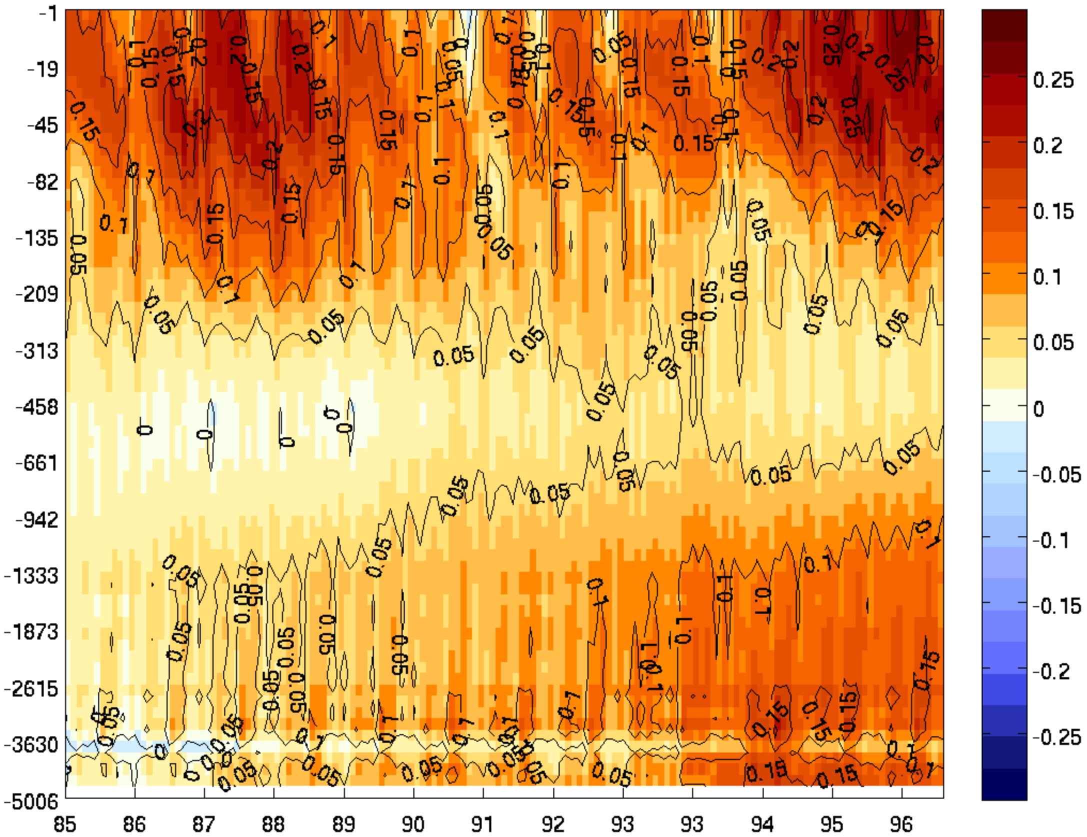

Figure 4-12: Salinity integral anomaly (psu) as function of depth and time calculated as model minus climatology for the 3Dvar experiment.

Many applications of the re-analysis estimates concern the climate change issues; in this context one of the most important quantity to be assessed in the model is the heat content shown in Figure 4-13. The volume temperature doesn't show a relevant drift neither in the SOFA nor in the 3Dvar estimates. The temperature annual cycle varies quite significantly from year to year. Usually the SOFA solution is colder then the 3Dvar one except in the last two years and the difference between the two solutions is visible in the extreme values (February and September) during some years.

The surface temperature values for the two estimates are compared to satellite observations in Figure 4-14 and they are quite close.

The vertical distribution of the temperature anomalies with respect to the climatology, horizontally averaged, is shown in Figure 4-15 and Figure 4-16 for SOFA and 3Dvar respectively. It is evident that both re-analysis estimates present the same patterns. There is a clear warm bias in the first 100 meters and a cold one between 100 and 900 meters, stronger in SOFA than in 3DVAR. The shallower part of the water column shows an alternation of positive and negative anomalies which indicates that the seasonal cycle in the model is more pronounced than in the climatology. In the bottom layers, from 900 meters downward, the temperature increases, more in SOFA than in 3Dvar again. In particular the biggest difference at intermediate depths between the SOFA and the 3Dvar estimates are in the two periods 1990-1992 and 1994-1996. Going into details SOFA shows lower heat content than 3Dvarr in 1990-1992 and viceversa in the period 1994-1996 We still have to continue the assessment of these events with independent data.

In order to better assess the skill in SST reconstruction, the root mean square error (RMSE), the bias (BIAS) and the anomaly correlation (AC) are computed. The RMSE shown in Figure 4-17, presents a quite large error especially in SOFA in the first year then the two curves converge to an annual mean error of about 0.6 degrees Celsius. Moreover it is interesting that the error shows a seasonal cycle: in summers the error is larger then in winters. In particular looking at the bias calculated as model minus observations it is clear that the model SST is warmer then the observed one. The mean bias is about 0.3 degrees Celsius and it accounts for a relevant part of the total error: almost the 50%. The AC score has been computed subtracting the monthly mean from observations and re-analysis estimates and is shown in Fig.4-19. The AC presents quite high values whose inter-annual mean for both the experiments is about 0.7 decreasing to values of 0.3 during winters. Also in this case it is possible to recognize a seasonal pattern but opposite respect to RMSE and bias: the AC shows a better performance f the estimates during summer than in winter. This may be due to the fact that eddies are more pervasive during winter and the correlation of their SST with observations more difficult to achieve. A high resolution model put particular emphasis on this problem since eddies of few tens of kilometres may be formed that could give a strong contribution to the decrease of the AC.

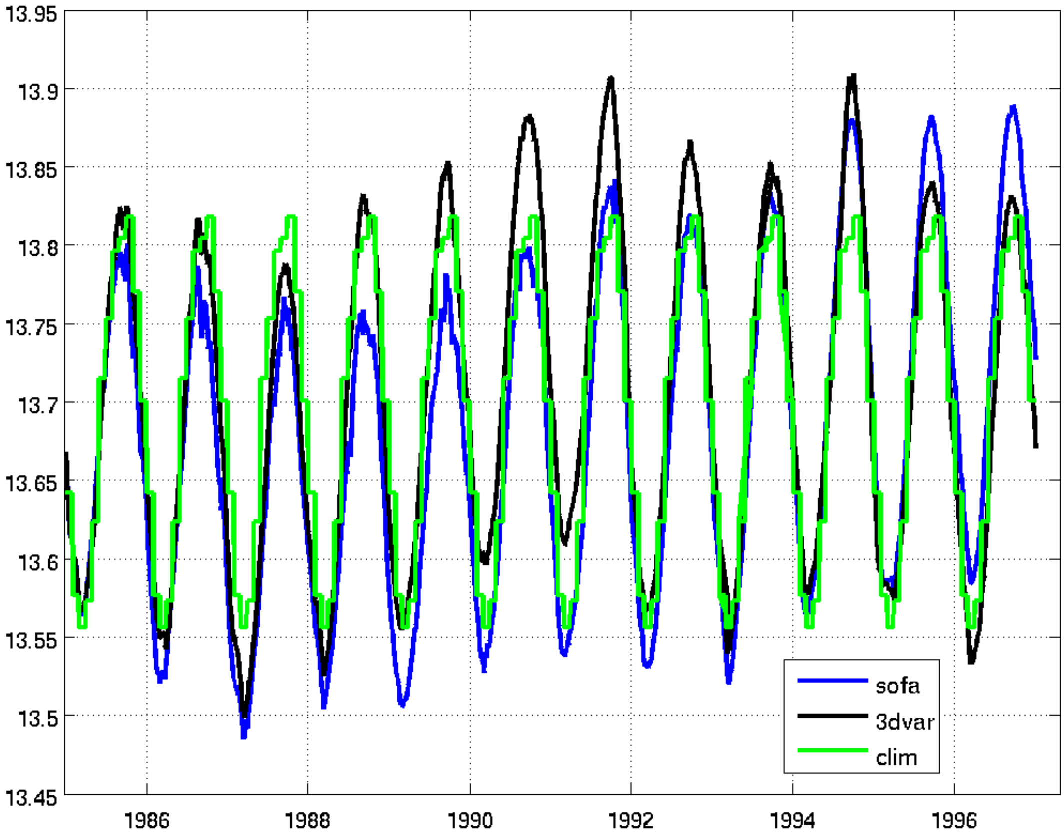

Figure 4-13: Temperature volume integral [degC]. Blue line is the SOFA solutions, Black line is the 3Dvar solution and the green line is the monthly mean climatology.

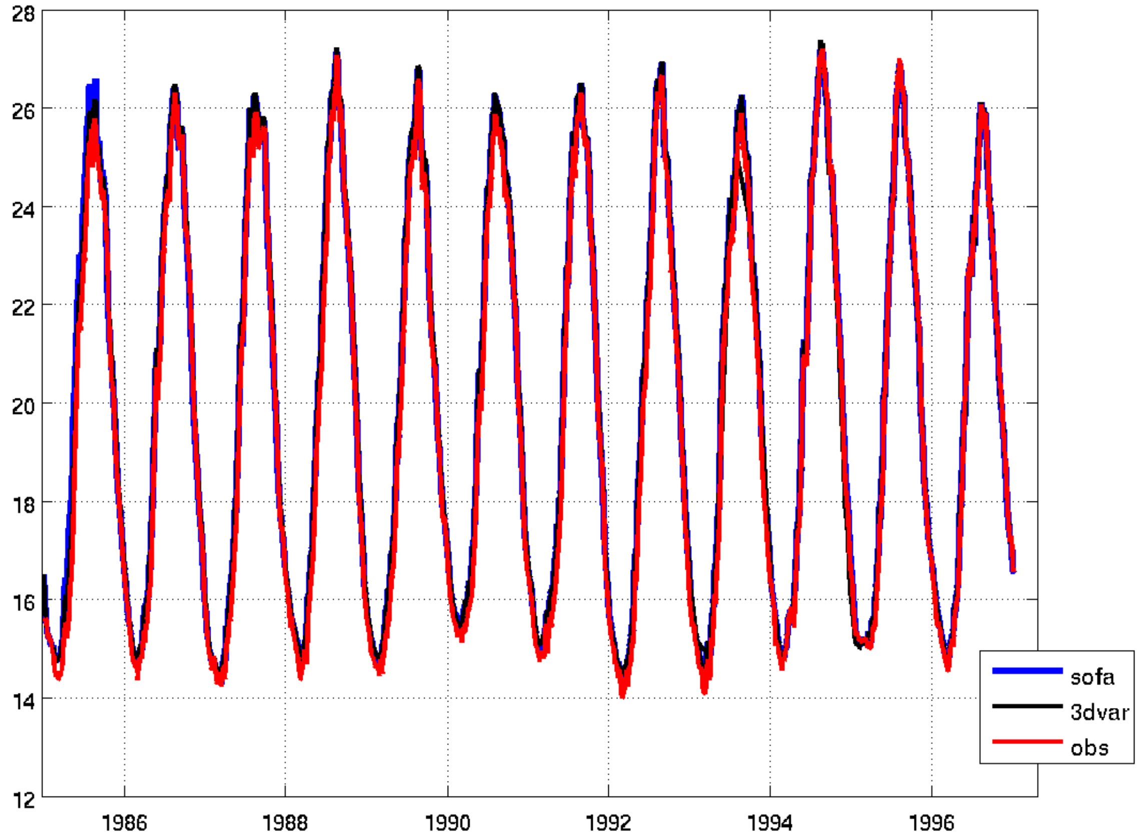

Figure 4-14: Temperature surface integral [degC]. Blue line is the SOFA solutions, Black line is the 3Dvar solution and the green line is the monthly mean climatology.

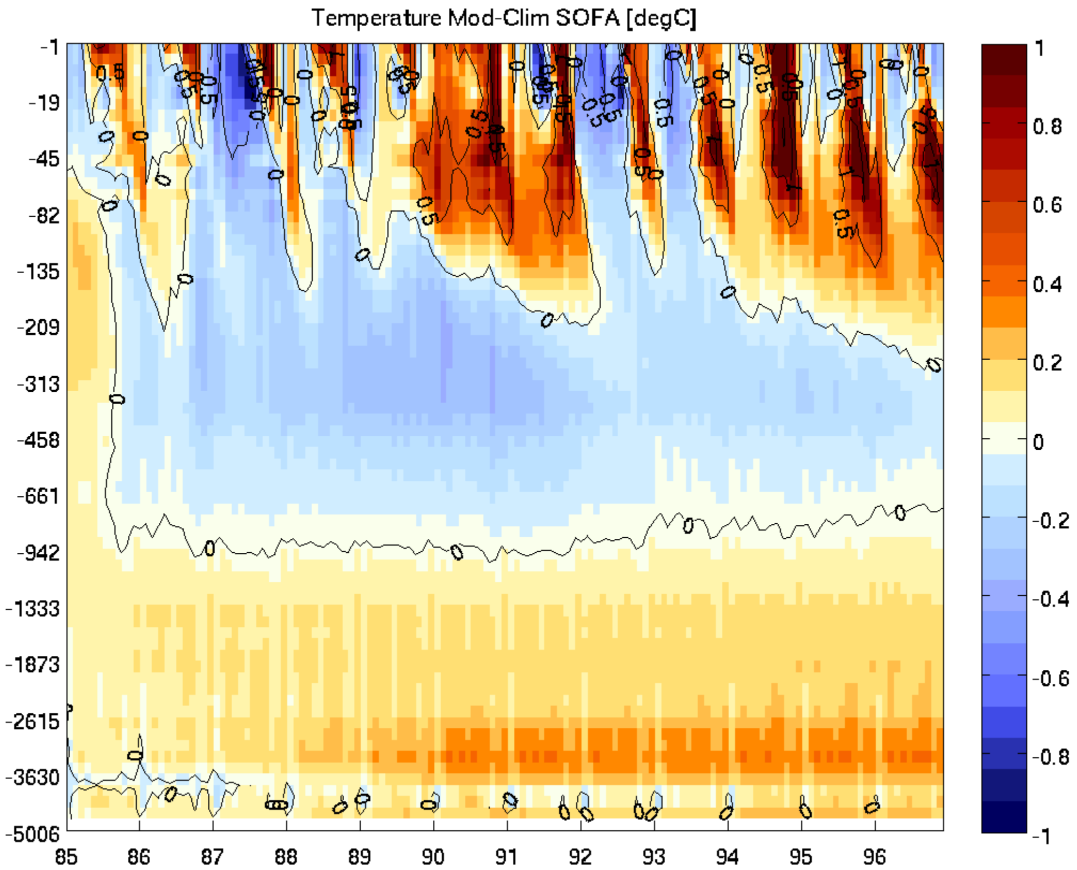

Figure 4-15: Temperature integral anomaly [degC] as function of depth and time calculated as model minus climatology for the SOFA experiment.

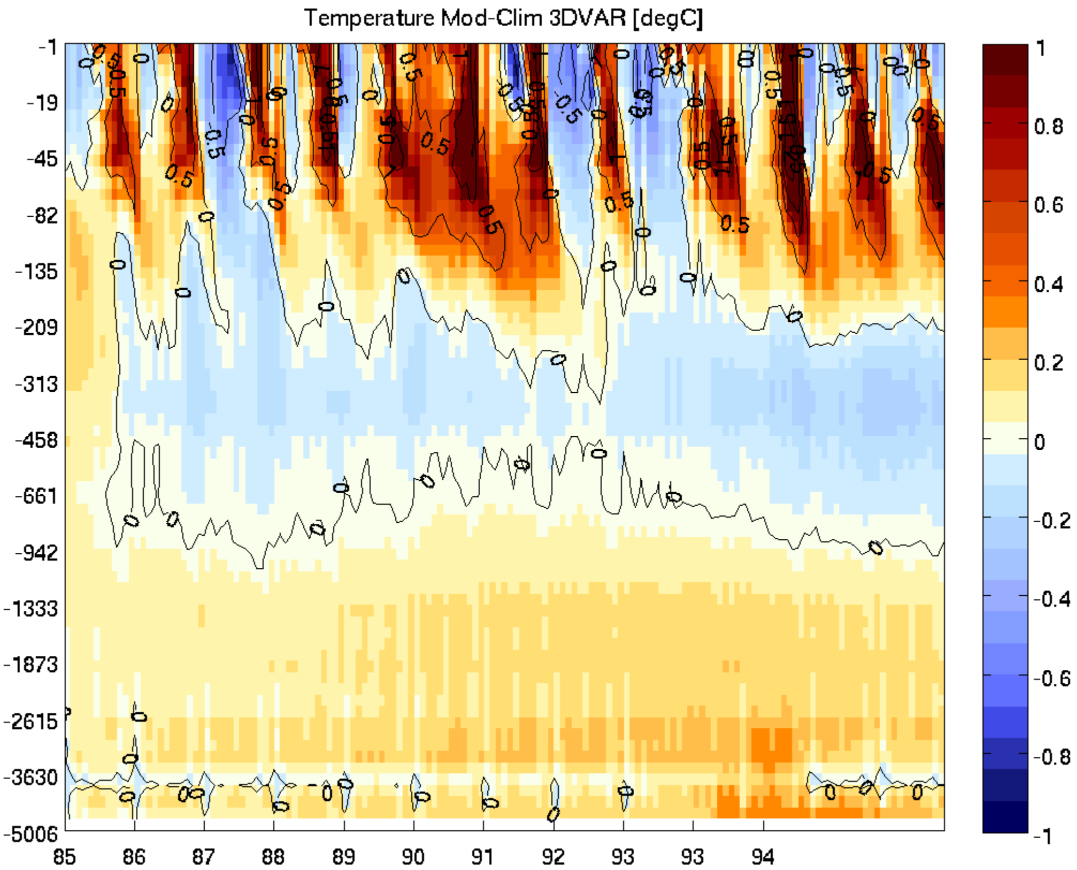

Figure 4-16: Temperature integral anomaly [degC] as function of depth and time calculated as model minus climatology for the 3Dvar experiment.

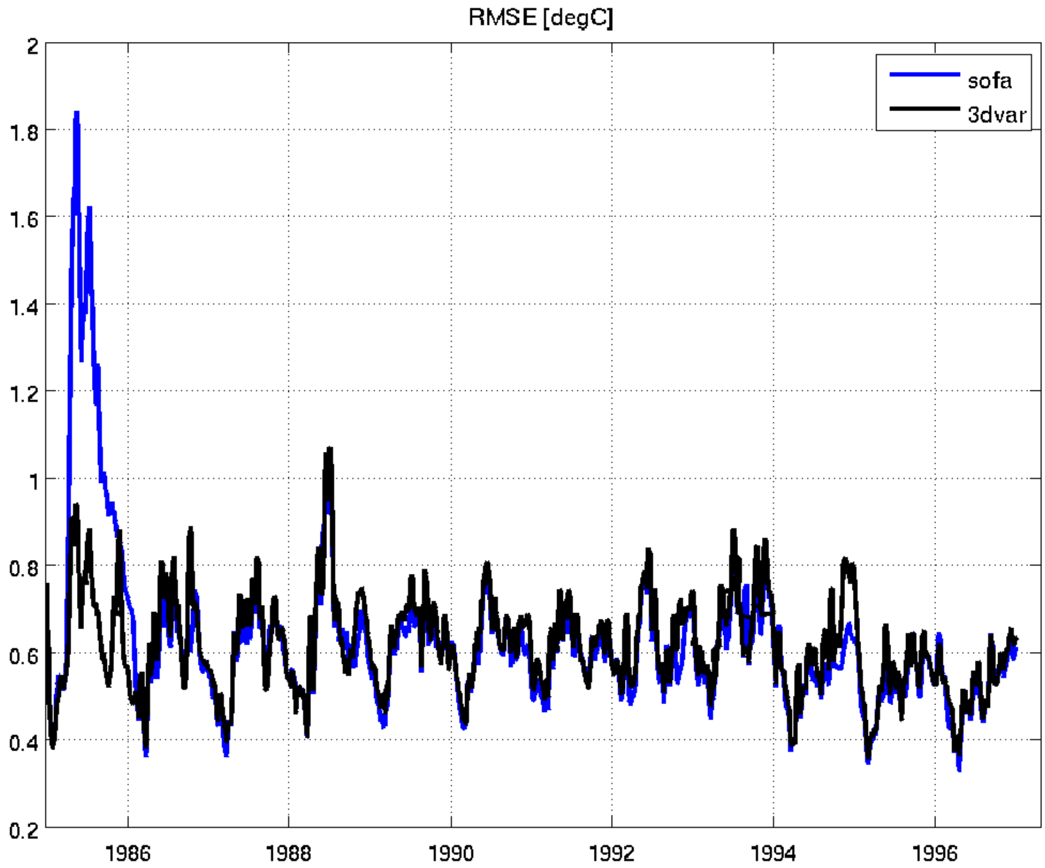

Figure 4-17: Root mean square error of the SST [degC]. Blue line is the SOFA solution, black line is the 3Dvar solution.

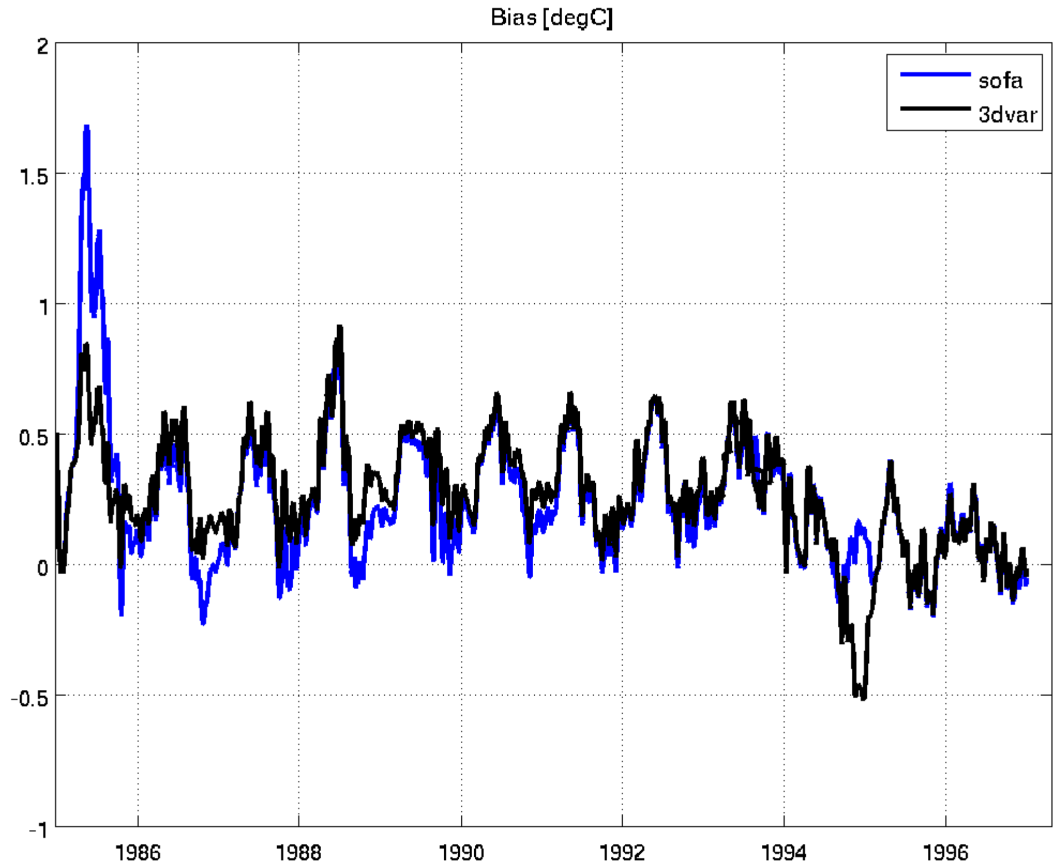

Figure 4-18: Bias of the SST [degC] calculated as model minus observations. Blue line is the SOFA solution, black line is the 3Dvar solution.

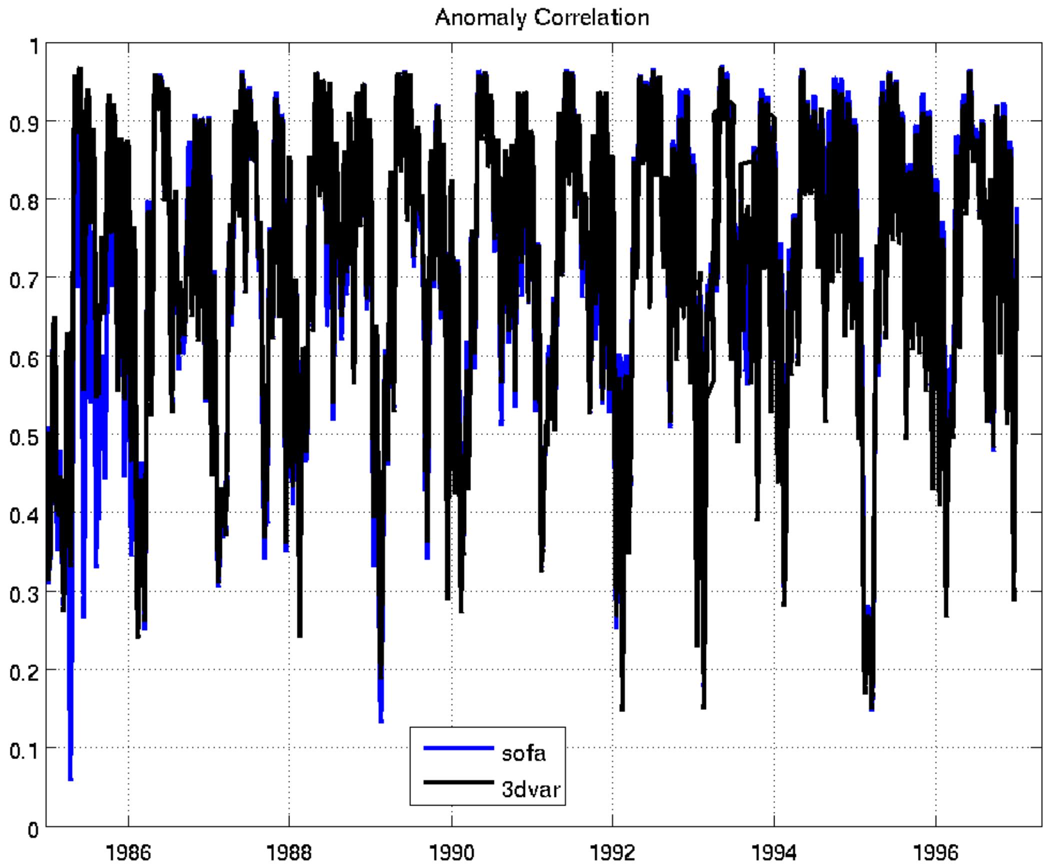

Figure 4-19: Anomaly correlation of the SST [degC] computed subtracting the monthly mean from the observations and the estimates. Blue line is the SOFA solution, black line is the 3Dvar solution

The volume integral of the Sea Surface Height (SSH) on the entire domain of the model is forced to be zero at each time step since the dynamical model enforces the volume conservation equation. However this may be not true for the assimilation estimates since there are no constraints considered in the minimization problem. We have then enforced that the corrections have basin mean equal to zero.

In Figure 4-20 the integral of the SSH is shown. The behavior of the SSH is quite similar for both reanalysis: the SSH sets immediately to negative values meaning that the basin mean of the Atlantic box is positive. This is consistent with the different density of the two basin water masses, one heavier than the other. A stable seasonal cycle of about 6 cm is evident which to be compared with altimetry should have the steric effect added (Tonani et al., 2007). 3Dvar and SOFA solutions are closer to each other after 1992 as it is expected because both the assimilation schemes use the same SLA measurements starting from October 1992.

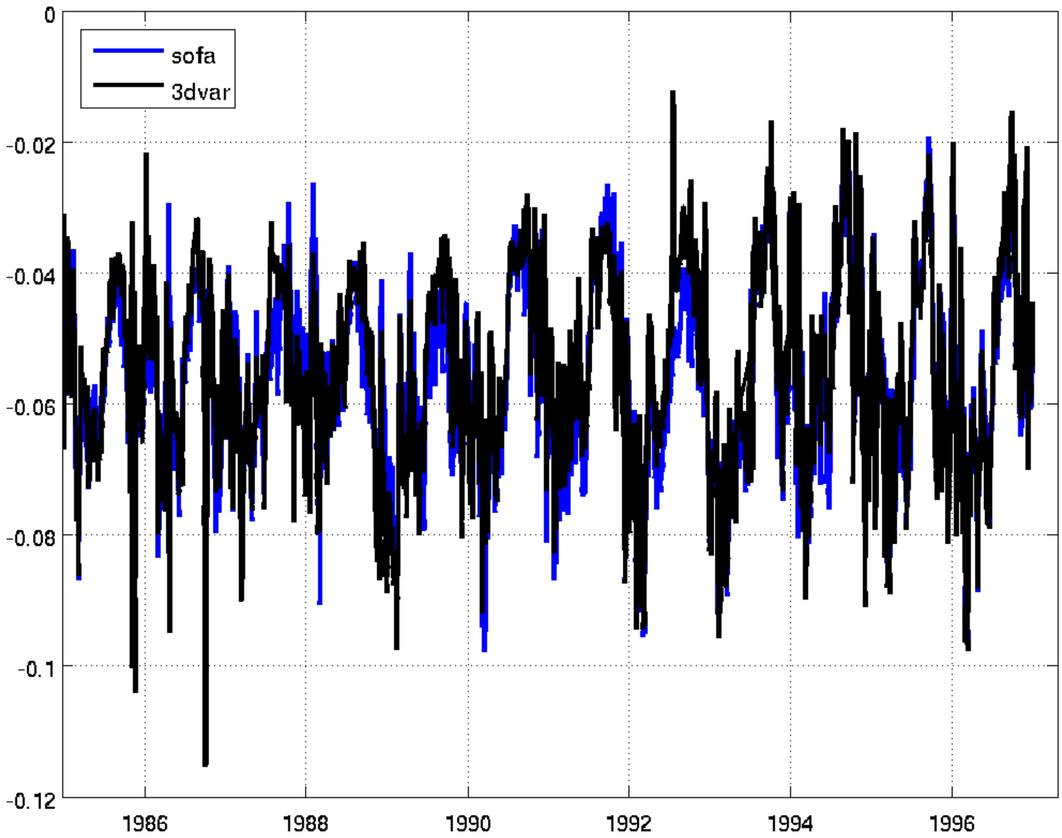

Figure 4-20: Integral of SSH [m]. Blue line is the SOFA solution, black line is the 3Dvar solution

Figure 4-21 shows the basin mean heat flux as a function of time: the green line is the climatology calculated from the NCEP reanalysis and the blue and black curves are the SOFA and the 3Dvar solutions. The inter-annual mean of the two time series is 8 W/m^2 for 3Dvar and 12 W/m^2 for SOFA while it is 2W/m^2 for climatology computed from NCEP re-analysis (Marzocchi, 2003). This problem is caused by an error in the OGCM which was discovered late in the thesis. However, this error was present in both the 3Dvar and SOFA reanalysis thus it should not influence the comparison between the two assimilation results. We believe that this error is the source for the next two problems shown in Figure 4-22 and 4-23. In Figure 4-22 the basin mean water flux is presented and it is clear. that the two estimates and the climatology are out of phase. Moreover the inter-annual mean value of the water flux is too small: 431 mm/yy for 3Dvar, 429 mm/yy for SOFA indicating low evaporation. Eventually also the net transport at Gibraltar straits is affected by this error since the inter-annual mean net transport is to low for both reanalysis (0.03 Sv) indicating that not enough water is entering trough the Gibraltar Strait.

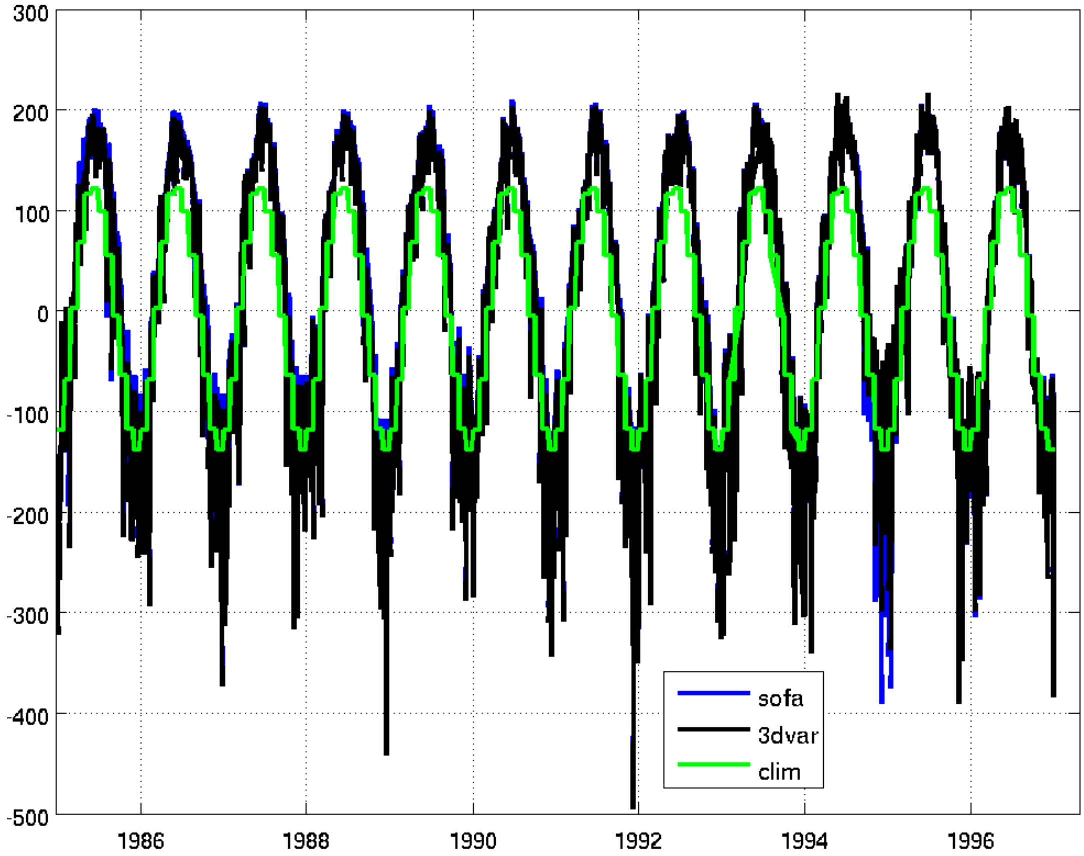

Figure 4-21: Basin Mean Heat Flux [Wm^{-2}]

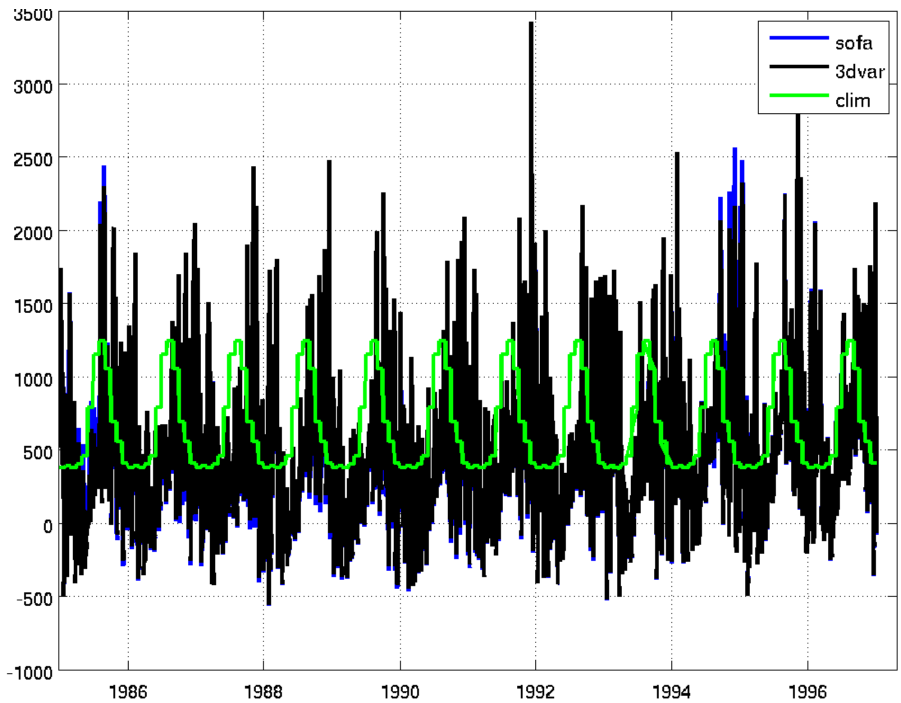

Figure 4-22: Basin Mean Water flux [mm/yy]

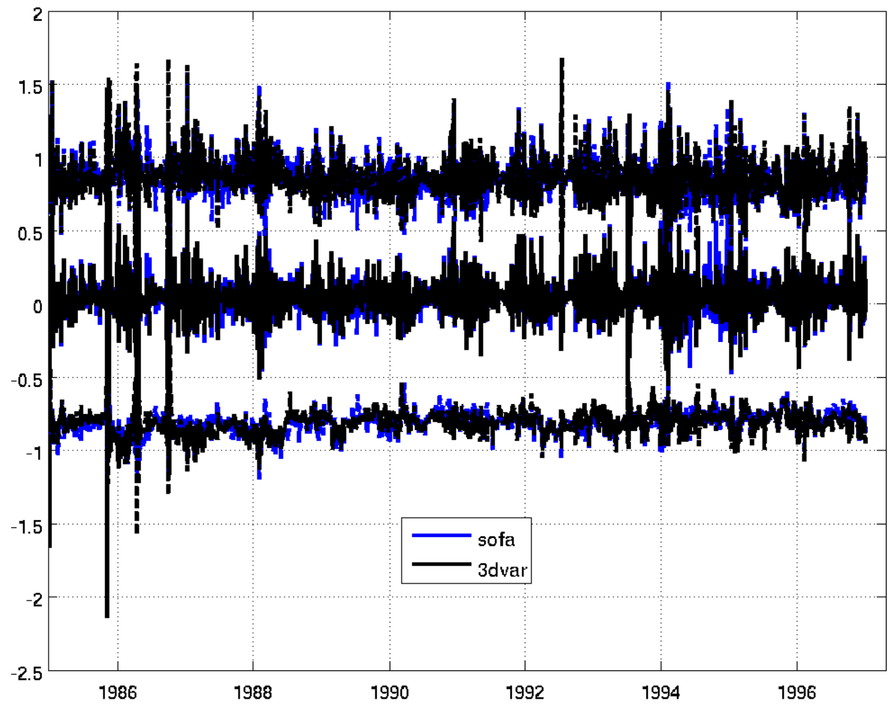

Figure 4-23: Gibraltar Transport [Sv]. The positive values indicate water entering into the Mediterranean basin, negative value transport out from the Mediterranean basin and two curves centered close to zero are the net transport.

The last assessment of the re-analysis estimates is done using the misfits. Misfits are defined as follows:

$$m = y_o - \mathbf{H}(x_b)$$

where y_o is an observation and x_b is the model solution H is the linearized observation operator, If we compute the misfits it is like to use independent data since they are calculated each day before the observations are inserted. It is not clearly a clear cut independent observation assessment but it is very important also to assess the progressive correction of the model solutions.

In Figure 4-24 the number of profiles used by SOFA and 3Dvar as a function of time are shown. The red bars are the number of salinity profiles available and the black bars are the number of temperature profiles. The upper panel indicates the number of profiles compared and assimilated with the SOFA while the lower panel is the number of profiles for the 3Dvar. Even if the number is comparable, the actual number is different for two reasons:

- SOFA can't assimilate profiles which are in areas whose depth is at shallower then 1000 meters while the 3Dvar can
- SOFA creates super-observations in case there are more profiles within the prescribed radius of influence while the 3Dvar handles each profile as independent.

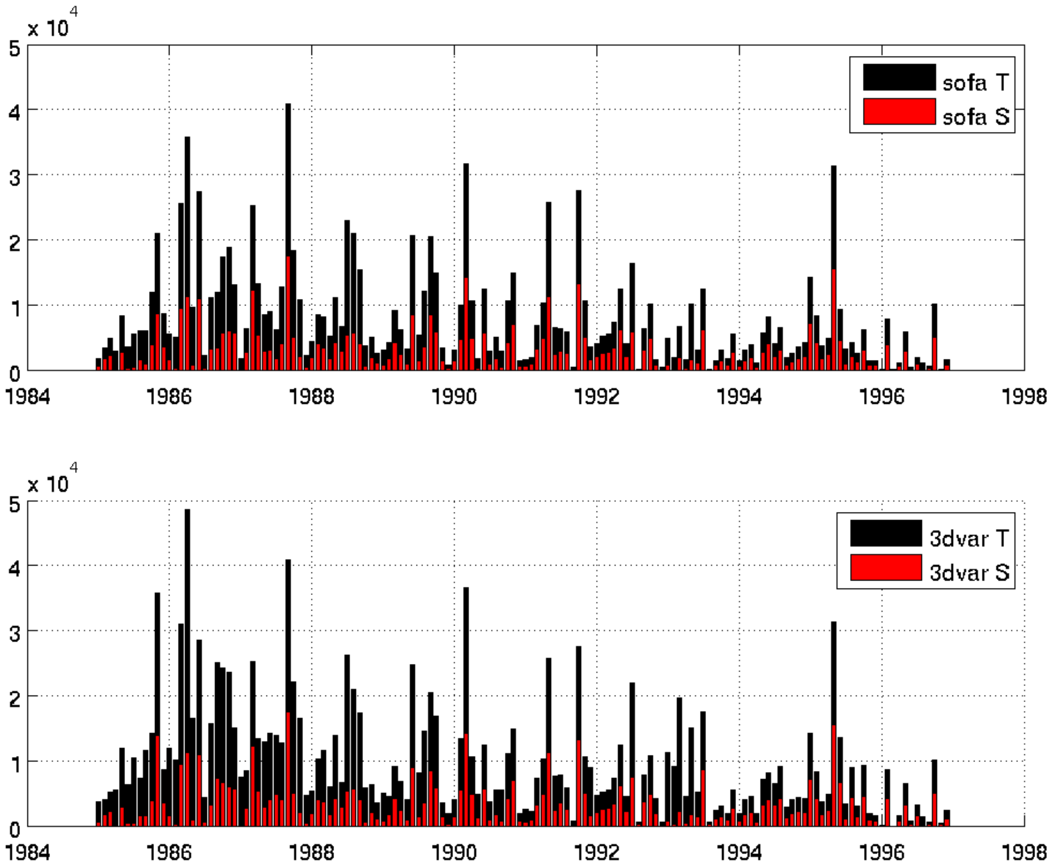

Figure 4-24: Number of assimilated profiles for SOFA (upper panel) and for the 3Dvar (lower panel). In red there is the number of salinity profiles in black of temperature ones.

The RMSE and the bias of the temperature and salinity misfits are now presented as a function of time and depth. For both the skill scores 3Dvar shows a better performance than the SOFA filter.

In particular the RMSE (Figure 4-25) of the 3Dvar is, on average, half of the SOFA one. In both cases the seasonal cycle of the error is visible with the highest values in summer and the lowest ones in winter. This may be due to difficulties for the model to create a very shallow and stratified thermocline in summer. It is interesting to notice that from 1994 to the end of the numerical experiments, the RMSE decreases significantly for both the reanalysis estimates but especially for the SOFA. It has to be kept in mind that the SLA data are assimilated from October 1992 thus it seems that after one year of assimilation of SLA data also the temperature field shows some improvements. Moreover since the SOFA decreases more then the 3Dvar it is possible that the impact of assimilating SLA data is bigger in SOFA then in 3Dvar. Quite crucial role may be played by the spatial distribution of that data. In fact the SLA data cover the whole basin in few days while the in situ measurements are usually over sampling a small region.

The bias, shown in Figure 4-26, is usually very small for both estimates but it is on average negative, indicating that the model is warmer than the observations. This might be confirming the hypothesis that the model has problems to create a very shallow thermocline during summer probably because of the inaccurate mixing scheme. The impact of the SLA assimilation is not visible in the bias and this is due to the fact that we consider the altimeter data with zero mean values.

It is interesting to note that, in October 1992, when the SLA data start to be assimilated the SOFA and 3Dvar schemes have an 'adjustment' shock in temperature of the opposite sign. In the future we should try to avoid such an adjustment by using a smoother mode approach to the insertion of SLA data.

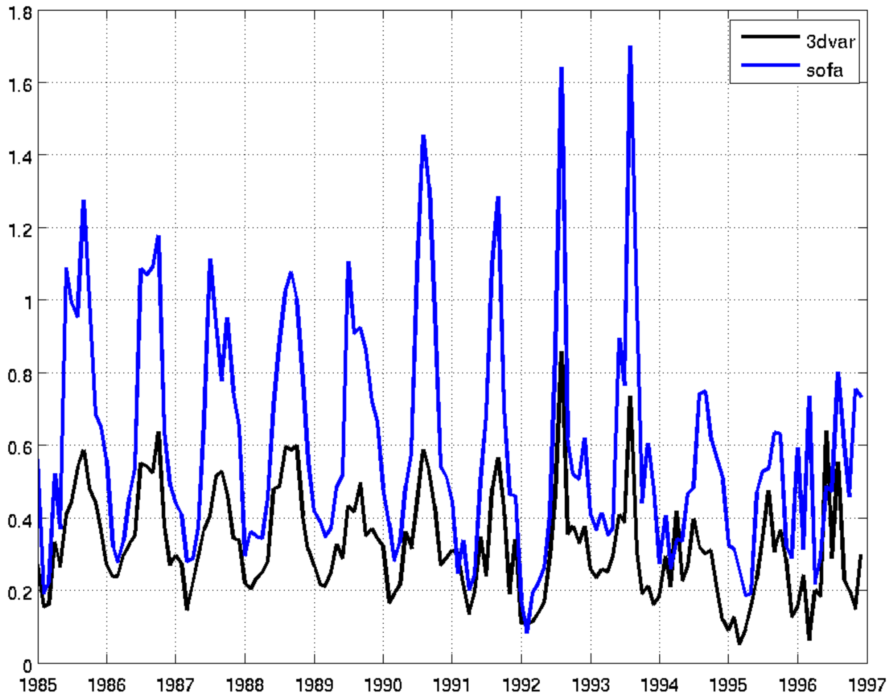

Figure 4-25: Basin mean root mean square of temperature misfits [deg C] as function of time.

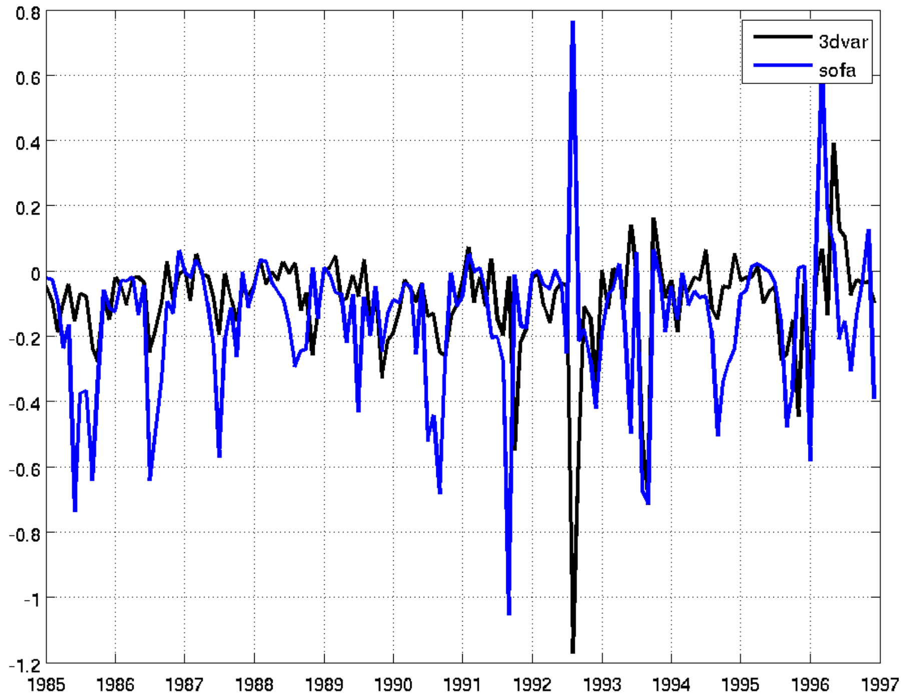

Figure 4-26: Basin bias of temperature misfits [deg C] as function of time.

Looking at the salinity skill scores as a function of time the same pattern of the temperature scores are recognizable. The RMSE and bias are presented in Figure 4-27 and Figure 4-28 respectively. The advantage of assimilating SLA data are less visible for the salinity than for the temperature: this is comprehensible considering the fact that the SLA data carry information on the upper water column density which is more influenced by the temperature then by the salinity. Concerning the bias we can say that, except in few cases, it is very close to zero. This is a quite strange result in the light of the results obtained by the comparison with the climatological salinity because the models were at every depth and always saltier then the climatology. This might be explained considering that the climatology has been created with a data set starting in the ninetieth century so it is possible that over the years the Mediterranean basin has become saltier then what it was.

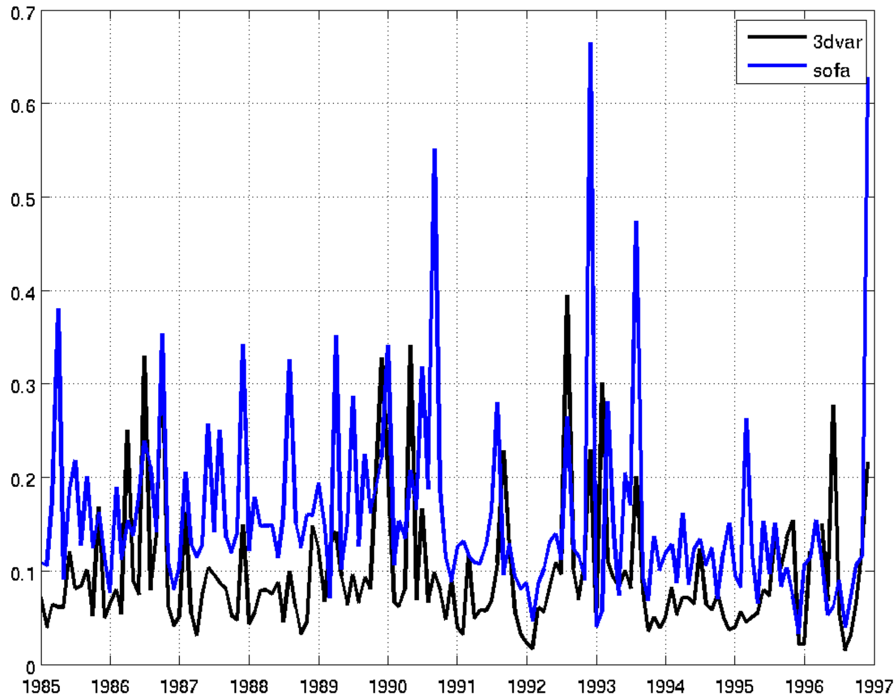

Figure 4-27: Basin mean root mean square of salinity misfits [psu] as function of time.

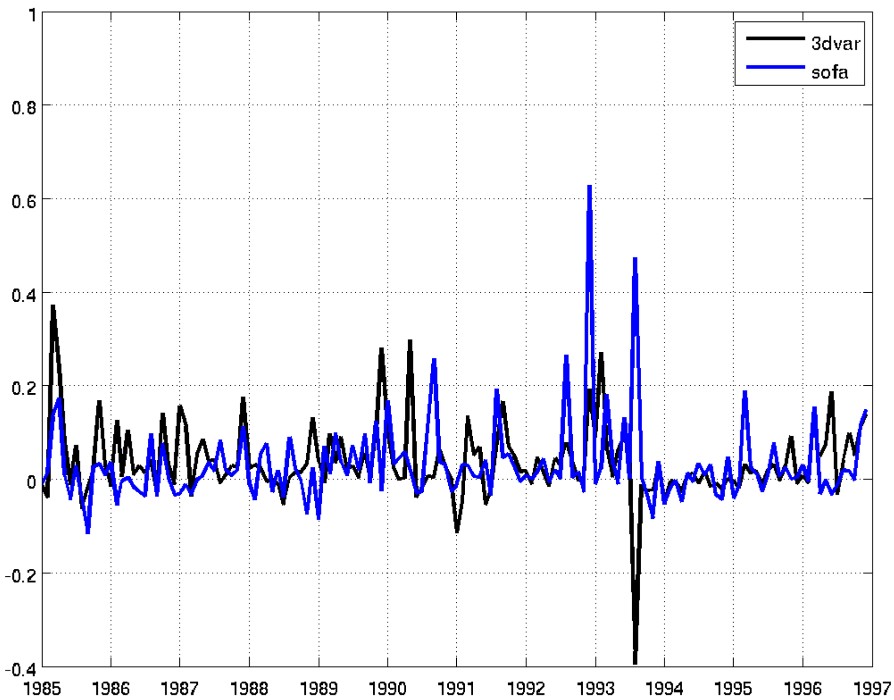

Figure 4-28: Basin mean bias of salinity misfits [psu] as a function of time.

In Figure 4-29 we show now the RMSE of temperature misfits as a function of depth. Once again the error is always bigger for SOFA then for the 3Dvar estimates. As it was expected the maximum error is at the summer thermocline depth (30-50 meters depth). The difference between the blue curve (SOFA) and the black curve (3Dvar) remains more or less constant over the water column as it was expected since both the assimilation schemes use the same EOFs to project the correction into the ocean. Comparing the bias (Figure 4-30) and the RMSE it is clearly visible that also in this case the bias counts for about half of the total error. The structure of the bias is interesting since it presents a zero crossing at 200 meters for both the reanalysis estimates and it is in agreement with the results obtained by the comparison with the climatology. The model seems to store to much heat at the surface and too little at the middle depth suggesting again a problem in the parameterization of the vertical mixing.

The salinity RMSE and bias have quite small values. In particular the RMSE is largest at the surface and this may be linked to a an inaccurate parameterization of the components of the water flux. Both the RMSE and the bias increase from 500 to the bottom, as it can be seen from Figure 4-31 and Figure 4-32, due to accumulation of salt in the bottom part of the water column.

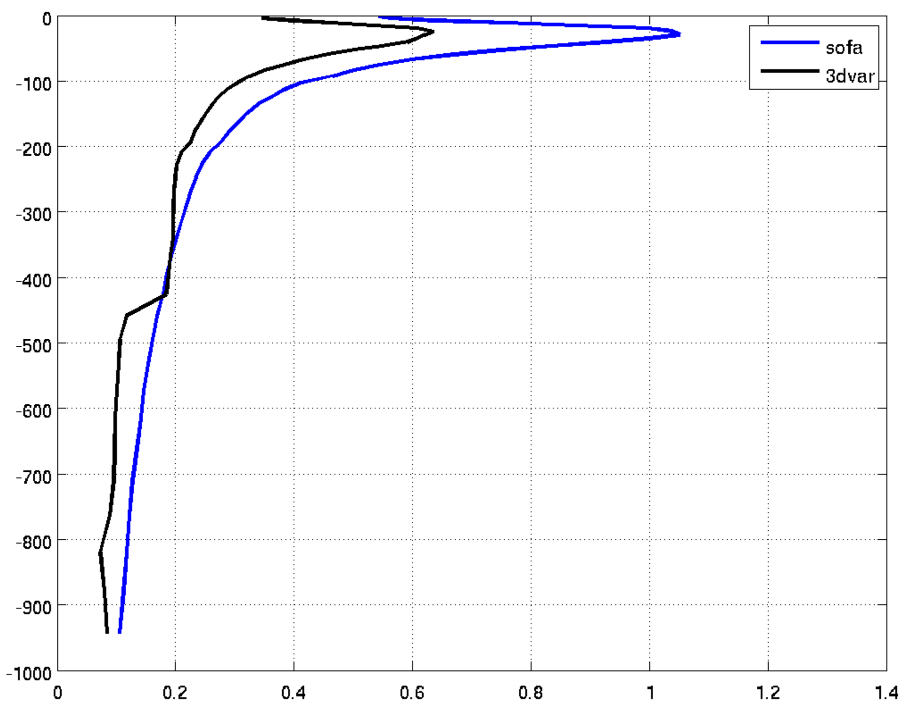

Figure 4-29: Root Mean Square of Temperature misfits [deg C] as a function of depth.

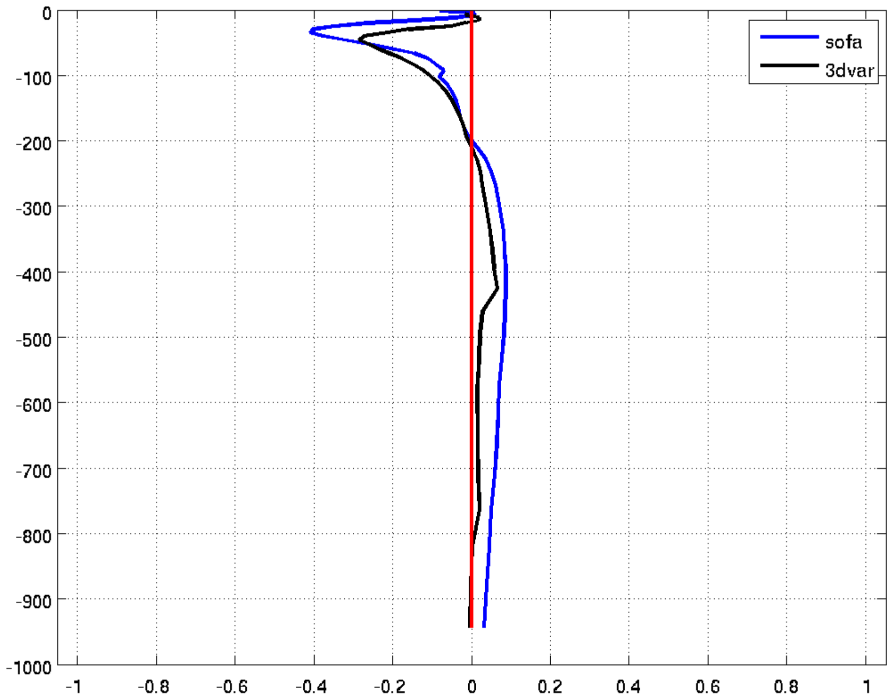

Figure 4-30: Bias of Temperature misfits [deg C] as a function of depth.

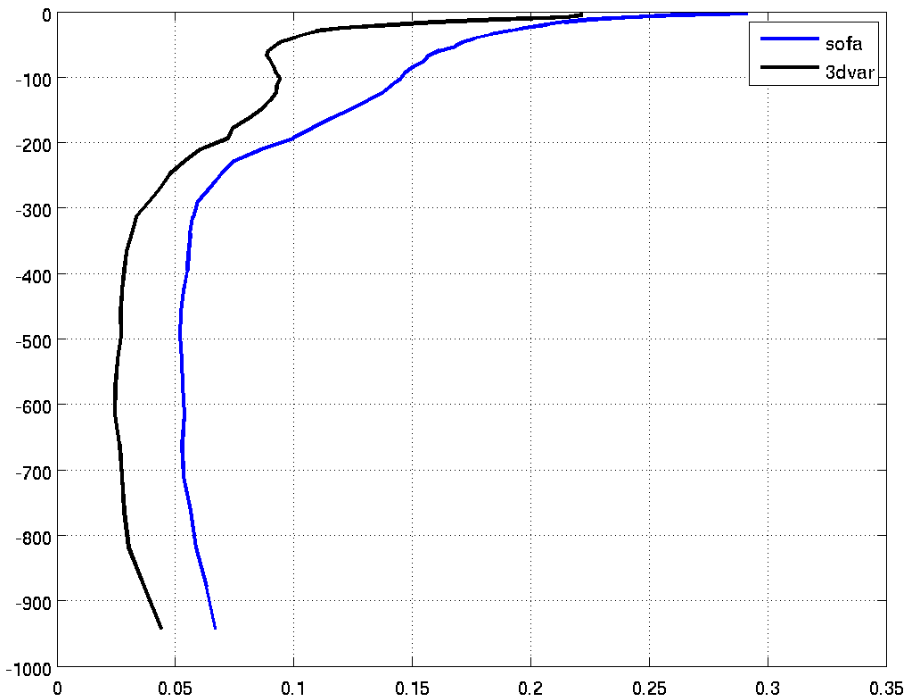

Figure 4-31: Root Mean Square of Salinity misfits [psu] as a function of depth.

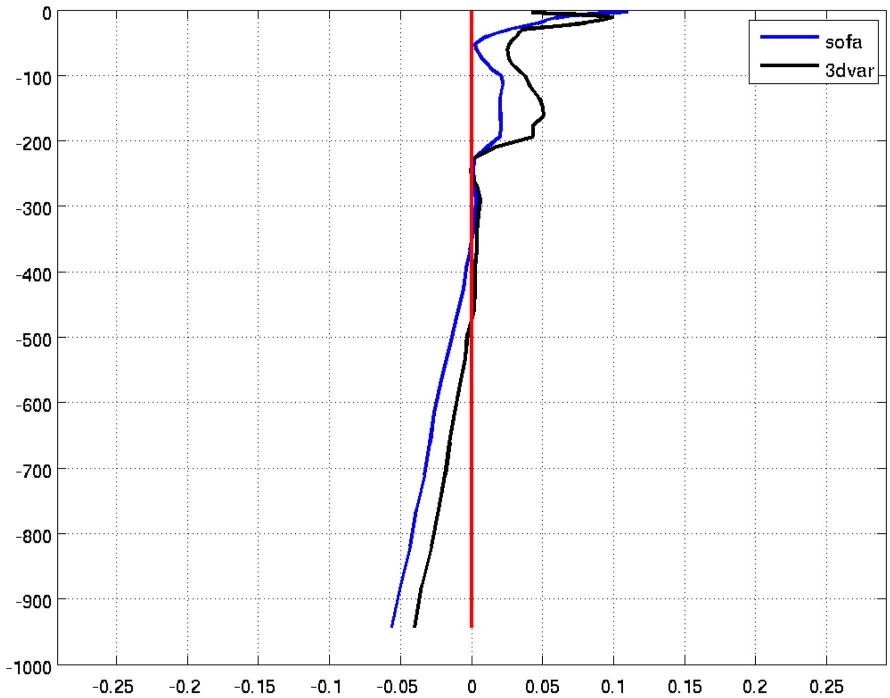

Figure 4-32: Bias of Salinity misfits [psu] as function of depth.

The Sea Level Anomaly misfit RMS for both the reanalysis are visualized in Figure 4-33 :. The behavior of the RMS is quite similar: as soon as the assimilation of SLA measurements starts the error decreases as it was expected. At the beginning the error of both reanalysis is almost the same: this is understandable considering that both the assimilations schemes use the same EOFs in order to specify the cross-covariances among the variables. The error decreases rapidly in the first year of assimilation and then it sets on a mean value of about 3 cm. This behavior of the error indicates that the system has some inertia and it needs some time to adjust to the new SLA data. This means also that the assimilation process is capable, not only to capture the information in the exact moment it is inserted, but it is also capable to keep it and propagate it correctly in the future. The performance of the assimilation schemes in acquiring information from SLA data is comparable between 3Dvar and SOFA reanalysis since the RMSE sets on approximately the same mean value. However it is very interesting to notice the opposite trend of the second half of year 1994. During this year the ERS satellite stop measuring and it returned available in 1995. In the first half of 1994 it seems that both the solutions are unaffected by the absence of the ERS measurements, however in the second part of that year the SOFA error tends to increase while the 3Dvar tends to decrease a bit. Only in December the 3Dvar RMSE seems to increase again to value comparable to the SOFA one. This may indicates that the 3Dvar is able to maintain the information for longer period and it is less affected by high spatial resolution of the ERS data.

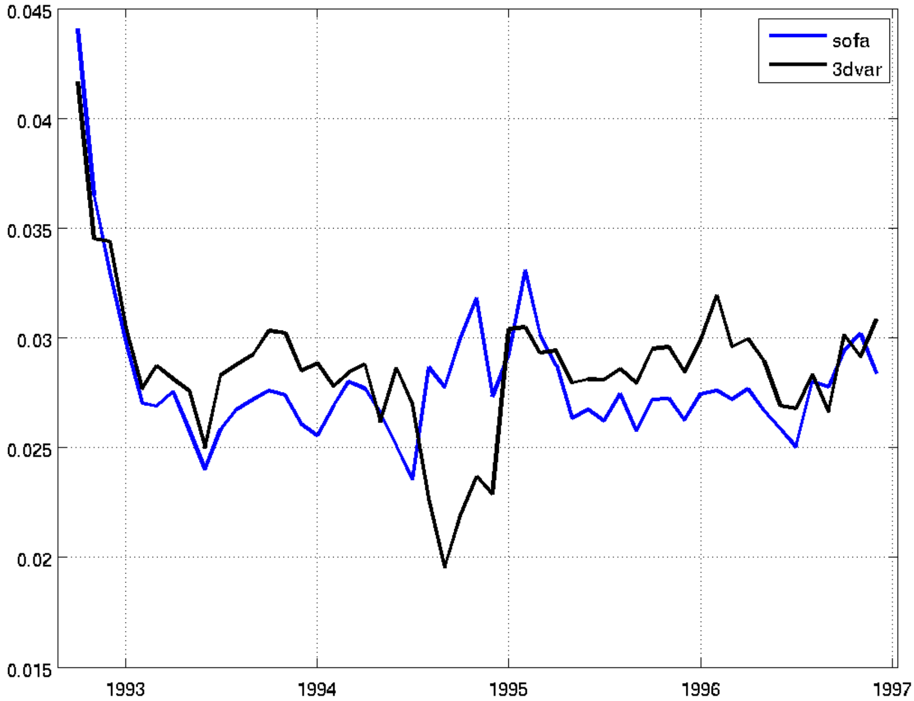

Figure 4-33 : Root mean square error of Sea Level Anomaly misfits [m].

5. Chapter: Conclusions

This study describes the development of modelling and data assimilation tools for the production of re-analsyses for the entire Mediterranean Sea. Data assimilation is a relatively recent development in oceanography since consistent observational data sets have been only recently collected for such an initiative to be meaningful, i.e. enough data are available to be assimilated into a dynamical model. Normally a re-analysis effort starts at the moment operational short term forecasting has set up both the general circulation model, the data assimilation scheme and the basic data collection infrastructure. Basically after some years the dynamical model starts to be used and observations assimilated, producing analyses of a certain quality, then re-analysis is needed to provide a space-time interpolated data set of high quality and value.

The Mediterranean Forecasting System started its activities in 1998 and after about ten years, several improvements in both the dynamical model and the data assimilation tools have been progressively done without however re-computing the analyses in a fully consistent way. In order to carry out a re-analysis two major steps were undertaken in this thesis. In the first, the general circulation model was upgraded to have the correct air-sea water fluxes. In the second, two assimilation schemes, one new and the other consolidated, were intercompared to show their impact on the quality of the re-analysis. Furthermore, in this thesis we have developed a totally new assimilation scheme, never applied to the Mediterranean area , that could give insight into the future tools of data assimilation for re-analysis.

The general circulation model used in this thesis is shown to be capable of reproducing quite accurately the ocean dynamics of the Mediterranean Sea. The results have shown that the model solution is in agreement with data and observations, even though some parameterizations of the model should be improved (i.e. heat flux and mixing processes). The new implementation of a realistic water flux, proposed in this study, has improved the model solution so that re-analysis is possible..

The two different assimilation schemes used in this thesis are: Sofa (De Mey and Benkiran,2000) and 3dvar (Dobriĉiĉ and Pinardi 2008). Two different reanalysis products have been obtained changing only the assimilation model. The study of the re-analysis produced shows that both products are sufficiently accurate for appropriate climate studies, except for the water budget and the heat budget. The problem related to these two air-sea fluxes has been found at the end of this work, preventing the possibility to re-compute the two re-analyses. Nevertheless, this error should not influence the results obtained from the comparison between the two assimilation schemes.

Both assimilation schemes show good capabilities in correcting the solutions provided by the dynamical model. Moreover it has been shown the ability of both systems in retaining this information and projecting it in the future. 3DVAR has demonstrated better skill than Sofa: in particular the 3DVAR solutions are better than Sofa one when the data are scarce and not homogeneously sampled. In the future the error on the heat flux will be corrected and new re-analysis will be computed in order to disseminate them to the scientific community with the aim of contributing to climate change studies.

Concerning the new data assimilation scheme, the Partitioned Kalman Filter and Smoother (PKFS), some of the hypothesis of the scheme have been verified. From an accurate analysis of the PKFS results, it has been shown that the assimilation scheme is capable to drive a “perturbed” solution toward the “true” one, even if the assumption on the relationships among the errors are not completely exact (steady state case). When the assumptions on the relationships among the errors are correct (time dependent experiment), the consistency of the results with the statistical assumptions demonstrates that the PKFS is not only capable of reducing the error of the simulation, but it can also associate measures of uncertainty to the assimilation estimates. Moreover it has been demonstrated that the Smoother solution is as good as the Filter one but it has the advantage to be physically consistent. The physical consistency has been achieved imposing the correction on the forcing, in our case wind stress.

Further assessment is necessary to give an answer to the question about the feasibility of applying PKFS in a realistic case using high resolution models. The results obtained from the experiments done in this preliminary work on the PKFS didn’t provide any evidence on the capacity of the PKFS to correct mesoscale errors. However it is already possible to affirm that the computational cost needed to model the state and control transition matrix will be huge for a high resolution model, such as the one used to compute the reanalysis.

APPENDIX A

The procedure to find the time asymptotic limit of the background error covariance matrix consists in integrating in time the Riccati equation. This method is quite inefficient from a computational point of view. An alternative way to compute it is using the so called "Doubling Algorithm". This recursive method allows to integrate in time step of power of two so that the computational savings are exponential. The recursion may be written as (Anderson and Moore, 1979):

$$\alpha_{k+1} = \alpha_k \left(I + \beta_k \gamma_k\right)^{-1} \alpha_k$$
$$\beta_{k+1} = \beta_k + \alpha_k \left(I + \beta_k \gamma_k\right)^{-1} \beta_k \alpha^T{}_k$$
$$\gamma_{k+1} = \gamma_k + \alpha^T{}_k \gamma_k \left(I + \beta_k \gamma_k\right)^{-1} \alpha_k$$

Starting the iteration with $\begin{cases} \alpha_1 = A^T \\ \beta_1 = H^T R^{-1} H \\ \gamma_1 = GQG^T \end{cases}$ and obtaining $\gamma_k = B^f_{2^k}$ at the k^th time step when the error converges.

Anderson B. and Moore J., 1979, *Optimal Filtering*, Prentice-Hall.

Ayoub N., Le Traon P. Y., De Mey P., 1997, *A description of the Mediterranean surface variable circulation from combined ERS-1 and TOPEX/POSEIDON altimetric data*, J. of Marine Systems, 18, 1-3 , 3-40

Bretherton F. P., Davis R. E., Fandry C. B., 1976, *A technique for objective analysis and design of oceanographic experiments applied to MODE-73*. Deep Sea Reserch, 23, 5559-582.

Daley, R. 1991, *Atmospheric data analysis*. Cambridge atmospheric and space science series, Cambridge University Press, ISBN 0-521 38215-7,.

De Mey P., and M. Benkiran, 2000*: A multivariate reduced-order optimal interpolation method and its application to the Mediterranean Basin–scale circulation.* Ocean Forecasting, Conceptual Basis and Applications*,* N. Pinardi, Ed., Springer-Verlag.

De Mey P.and Robinson A., 1987 *Assimilation of altimeter eddy fields into a limited area quasi-geostrophic model*. J. Phys. Oceanogr. 17 12. 2280–2293

Demirov, E. and Pinardi, N., 2002, *Simulation of the Mediterranean Sea circulation from 1979 to 1993. Part I: The interannual variability*, J. of Marine Systems., 33–34, 23–50,

Dobriĉiĉ, S., Pinardi, N., Adani, M., Bonazzi, A., Fratianni, C., and Tonani, M.: *Mediterranean Forecasting System: An improved assimilation scheme for sea-level anomaly and its validation*, Q.J. R.. Meteorol. Soc., 131, 3627–3642, 2005.

Dobriĉiĉ. S., *An Oceanographic Three-dimensional Variational Data Assimilation Scheme*, Ocean Modelling, in press

Dobriĉiĉ S., N. Pinardi, M. Adani, M. Tonani, C. Fratianni, A. Bonazzi, and V. Fernandez, 2007, *Daily oceanographic analyses by Mediterranean Forecasting System at the basin scale*, Ocean Sci., 3, 149–157

Dobriĉiĉ, S. 2005, *New mean dynamic topography of the Mediterranean calculated from assimilation system diagnostics*, Geophys. Res. Lett., 32, L11606.

Fu L.-L., Fukumori I, Miller R.N. 1993, *Fitting dynamic models to the Geosat sea level observations in the Tropical Pacific Ocean, II, A linear wind-driven model*, J. Phys. Oceanogr., 23, 2162-2181.

Fukumori I, Benveniste J., Wunsh C., Haidvogel D.B., 1993, *Assimilation of Sea Surface Topography into an Ocean Circulation Model Using a Steady-State Smoother*., J. Phys. Oceanogr., 23,1831-1855.

Fukumori I. and Malanotte-Rizzoli P., 1995, *An approximate Kalman filter for ocean data assimilation: An example with idealized Gulf Stream model*. J. of Geophis. Res., 100, C4, 6777-6793,

Fukumori I.,1995, *Assimilation of TOPEX sea level measurements with a reduced-gravity, shallow water model of the tropical Pacific Ocean*. J. of Geophis. Res., 100, C12, 25027-25039.

Fukumori I., Raghunath R., Fu L.-L., Chao Y, 1999, *Assimilation of TOPEX/Poseidon altimeter data into a global ocean circulation model: How good are the results?* J. of Geophis. Res., 104, C11,25647-25665.

Fukumori I., Raghunath R., Fu L.-L., 1998, *Nature of global large-scale sea level variabilità in relation to atmospheric forcing: A modeling study*. J. of Geophis. Res., 103, C3,5493-5512.

Fukumori I., 2005, *Prescribing and estimating model error : what is assimilation really solving?* View of Oceanography, edited by E.P. Chassignet and J. Verron,. Springer

Fukumori I., (2001), *A Partitioned Kalman Filter and Smoothe*r. Mon. Weather Rew., 130 1370-1382.

Malanotte Rizzoli P. and the POEM Group., 1996. *Experiment in the Eastern Mediterranean probes the origin of deep water masses*. *EOS* **77** 32, pp. 305–307

Millot C., 1985 *Some features of the Algerian current*. J. Geophys Res.,90, 7169-7176.

Molcard, A., Piterbarg, L., Griffa, A., Özgökmen, T.,M., Mariano A.J.,2002: *Assimilation of drifter position for the reconstruction of the Eulerian circulation field*, J. of Geophis. Res., 108, 3056-3077,

Arnone R. A., Wiesenburg D. A., Saunders K.D.,1990, *The origin and characteristics of the Algerian Current*, J. Geophys. Res.,95,1587-1598.

Gauthier P., Charete C., Filion L., Koclas P., Laroche S., 1999, *Implementation of a 3D variational data assimilation system at the Canadian Meteorological Center. Part I: Global analysis.* Atmosphere-Ocean, 37, 103-156.

Heburn G. W. and La Violette P. E., 1990, *Variations in the structure of the anticyclonic gyres found in the Alboran Sea.*, J. Geophys. Res.98, 1599-1613.

Ovchinnikov I.M., Zats V.I., Krivosheya V.G., Nemirosky M.S. Udov A.I., 1987, *Winter convection in the Adriatic and formation of deep eastern Mediterranean waters*. Ann. Geophys., 5B,89-92

Le Traon, P. Y. and Ogor, F.(1998): *ERS-1/2 orbit improvment using Topex/poseidon: the 2 cm challenge*, J. Geophys. Res, 103, 8045–805, 1998.

Lorenc, A. C., 1997: *Development of an operational variational assimilation scheme*. J. Met. Soc. Japan, 75, 339-346.

Paschini, E., Artegiani, A., Pinardi, N., 1993, *The mesoscale eddy field of the middle Adriatic Sea*, Deep Sea Reserch I ,40, 1365-1377

Pinardi N., Navarra A., 1993, *Baroclinic wind adjustment processes in the Mediterranean sea*, Deep-sea research II, 40,. 1299-1326

Pinardi N., Masetti E., 2000, *Variability of the large scale general circulation of the Mediterranean Sea from observations and modelling: a review*. Paleo, 158, 153-174.

Pinardi, N., Rosati, A., and Pacanowski, R. C. 1995, *The sea surface pressure formulation of rigid lid models. Implications for altimetric data assimilation studies*, J. Mar. Syst., 6, 109–119,.

Rixen, M.; Beckers, J.-M.; Maillard, C., 2002*, A hydrographic and biochemical climatology of the Mediterranean and the Black Seas: some statistical pitfalls*, in: Brown, M. et al. (Ed.) (2002). The Colour of Ocean Data: International Symposium on oceanographic data and information management, with special attention to biological data. Brussels, Belgium, 25-27 November 2002: book of abstracts. VLIZ Special Publication.

Robinson A.R., Lesile W.G., Theochraris A., Lascaratos A., 2001, *Mediterranean Sea Circulation*, Indira.

Robinson, A.R., A. Hecht, N. Pinardi, J. Bishop, W.G. Leslie, Y. Rosentraub, A.J. Mariano and S. Brenner, 1987, *Small Synoptic/Mesoscale Eddies: The Energetic Variability of the Eastern Levantine Basin*. Nature, 327(6118), 131-134.

Robinson A. R., Sellschopp J., 2000, *Rapid Assessment of the Coastal Ocean Enviroment,* Ocean Forecasting, Conceptual Basis and Applications, N. Pinardi, Ed., Springer-Verlag.

Trenberth and Olson, 1988, *An Evaluation and Intercomparison of Global Analyses from the National Meteorological Center and the European Centre for Medium Range Weather Forecasts*, Bulletin of the American Meteorological Society, 69, 9, 1047-1057.

Trenberth and Guillemot, 1995, *Evaluation of the Global Atmospheric Moisture Budget as Seen from Analyses*, J. of Climate, 8, 9, 225-2272.

Tonani M., Pinardi N. Dobriiĉiĉ, Pujol I., Fratianni C., 2008, *A high-resolution free-surface model of the Mediterranean Sea*, Ocean Sci. 4, 1–14,

Zavattarelli M., Mellor G.L., *A numerical Study of the Mediterranean Sea Circulation*., J. Phys. Oceanogr., 25,1384-1414

Madec G., Delecluse P., Imbard M., Levy C., 1998, OPA 8.1 *Ocean general Circulation Model reference manual*. Note du Pole de modelisazion, Institut Pierre-Simon Laplace (IPSL), France, 11

Pujol M. I.,and Larnicol G.,(2005) *Mediterranean sea eddy kinetic energy variability from 11 years of altimetric data,* J. Marine Sys,58.3-4.121-141.

Raicich F., 1996, *On the fresh water balance of the Adriatic Sea*, J. Marine Sys, 9, 305-319.

Roullet G., Madec G., 2000, *Salt conservation, free surface, and varying levels: a new formulation for ocean general circulation model*, J. Geophys Res.,105, C10, 23, 927-23,942.

Rousseanov V., Stanev V., Artale V., Pinardi N., 1995, *A seasonal model of the Mediterranean Sea general circulation*, J. Geophys Res., 100, C7, 13515-13538.

Marzocchi F., 2003, *Regimi climatici del Mediterraneo,* Tesi di Laurea, Facoltà di Scienze Ambientali, Università di Bologna

Mariotti A., Struglia V., Zeng N., Lau K.M., 2002, *The Hydrological Cycle in the Mediterranean Region and Implications for the Water Budget of the Mediterranean* Sea, Journal of Climate,15, 1674-1690.

Pujol M.-I., Larnicol G., *Mediterranean sea eddy kinetic energy variabilità from 11 years of altimetric data*. J. Marine Sys, 58, 121-142.

Talagrand, O.: *On the damping of high-frequency motions in fourdimensional assimilation of meteorological data*, J. Atmos. Sci., 29, 1571–1574, 1972

Von Storch H. and Navarra A., 1999, *Analisys of Climate Variability*, Springer.

Griffies S.M., 2005,*Some ocean model fundamentals*,: in Ocean Weather Forecasting: an Integrated View of Oceanography, edited by E.P. Chassignet and J. Verron, pages 19–73. Springer

Kistler, R., E. Kalnay, W. Collins, S. Saha, G. White, J. Woollen, M. Chelliah, W. Ebisuzaki, M. Kanamitsu, V. Kousky, H. van den Dool, R. Jenne, and M. Fiorino, 2001: *The NCEP-NCAR 50-Year Reanalysis: Monthly Means CD-ROM and Documentation*. Bull. Amer. Meteor. Soc., 82, 247-268.

S. Marullo, B. Buongiorno Nardelli, M. Guarracino, and R. Santoleri.2007 *Observing The Mediterranean Sea from space: 21 years of Pathfinder-AVHRR Sea Surface Temperatures (1985 to 2005). Re-analysis and validation.*Ocean Sci,3,299-310.

Pedlosky J.,1987, *Geophysical Fluif Dynamics* Springer